12-2012

Design and Optimization of Four-dimensional Cone-beam Computed Tomography in Image-guided Radiation Therapy

Moiz Ahmad

Design and Optimization of Four-dimensional Cone-beam Computed Tomography in Image-guided Radiation Therapy

by

Moiz Ahmad, B.S.

Approved:

Tinsu Pan, Ph.D., Supervisory Professor

George Starkschall, Ph.D.

Peter Balter, Ph.D.

Valen E. Johnson, Ph.D.

Lei Dong, Ph.D.

Approved:

Dean, The University of Texas Graduate School of Biomedical Sciences at Houston

Design and Optimization of Four-dimensional Cone-beam Computed Tomography in Image-guided Radiation Therapy

A

Dissertation

Presented to the Faculty of

The University of Texas
Health Science Center at Houston

and

The University of Texas
MD Anderson Cancer Center
Graduate School of Biomedical Sciences

in Partial Fulfillment
of the Requirements
for the Degree of

Doctor of Philosophy

by

Moiz Ahmad, B.S.

Houston, Texas
December 2012

Design and Optimization of Four-dimensional Cone-beam Computed Tomography in Image-guided Radiation Therapy

Publication No. _____

Moiz Ahmad, B.S.

Supervisory Professor: Tinsu Pan, Ph.D.

The influence of respiratory motion on patient anatomy poses a challenge to accurate radiation therapy, especially in lung cancer treatment. Modern radiation therapy planning uses models of tumor respiratory motion to account for target motion in targeting. The tumor motion model can be verified on a per-treatment session basis with four-dimensional cone-beam computed tomography (4D-CBCT), which acquires an image set of the dynamic target throughout the respiratory cycle during the therapy session. 4D-CBCT is undersampled if the scan time is too short. However, short scan time is desirable in clinical practice to reduce patient setup time. This dissertation presents the design and optimization of 4D-CBCT to reduce the impact of undersampling artifacts with short scan times.

This work measures the impact of undersampling artifacts on the accuracy of target motion measurement under different sampling conditions and for various object sizes and motions. The results provide a minimum scan time such that the target tracking error is less than a specified tolerance. This work also presents new image reconstruction algorithms

for reducing undersampling artifacts in undersampled datasets by taking advantage of the assumption that the relevant motion of interest is contained within a volume-of-interest (VOI). It is shown that the VOI-based reconstruction provides more accurate image intensity than standard reconstruction. The VOI-based reconstruction produced 43% fewer least-squares error inside the VOI and 84% fewer error throughout the image in a study designed to simulate target motion. The VOI-based reconstruction approach can reduce acquisition time and improve image quality in 4D-CBCT.

Acknowledgments

I thank my advisor Dr. Tinsu Pan foremost for providing me fulfilling and enjoyable research work. In every experiment and discussion together, he always had a gem of wisdom. Dr. Pan provided me balance with his perspective and challenged me to expand my possibilities.

One is lucky to find such a mentor as Dr. Pan, but I was doubly fortunate to have had a few other mentors at MD Anderson. Among these, I cannot repay Drs. Richard Wendt and Jingfei Ma for their inspiration and encouragement. I also could not have finished this work without the invaluable counsel of my supervising committee members.

I thank my classmates Adam Riegel, Hua Ai, and Richard Castillo for their support and advice, and particularly for helping me write code for all of life's little tasks.

I am also grateful for the generous support from the Schissler Family Foundation provided through their MD Anderson Cancer Center Fellowship. I was also supported by grants from the Cancer Prevention Research Institute of Texas and from Varian Medical Systems.

I am eternally thankful to my family, especially to: my mother for her self-sacrificing character, my father for his perseverance, my sister Maria for her voice and protection, my Nani for her absolute devotion, and my darling Christine for lending me her heart, mind, eyes, and ears.

This one is for my father. Get well soon!

Contents

Abstract iii

Acknowledgments v

Contents vii

List of Figures ix

List of Tables xi

List of Abbreviations xii

1 Introduction 1

1.1 Hypothesis . . . 2
1.2 Specific Aims . . . 2
1.3 Significance . . . 2
1.4 Dissertation organization . . . 4

2 Background and previous work 5

2.1 Radiation therapy . . . 5
2.1.1 Treatment planning . . . 6
2.1.2 Motion management and 4D-CT . . . 6
2.2 Image-guidance in radiation therapy . . . 7
2.2.1 Cone-beam computed tomography . . . 8
2.2.2 Four-dimensional CBCT . . . 9
2.3 Challenges in 4D-CBCT . . . 11

2.4 Previous work . . . 13
2.4.1 4D-CBCT sampling strategies . . . 13
2.4.2 Image reconstruction strategies . . . 14

3 Acquisition Optimization 16
3.1 Methods . . . 17
3.1.1 Offset vs. Centered Detector Configuration . . . 18
3.1.2 Image Reconstruction . . . 18
3.1.3 Phantom Study . . . 20
3.1.4 Patient study . . . 21
3.1.5 Measurement of image trajectory . . . 21
3.1.5.1 Region-of-interest constraint in image registration . . 23
3.2 Results . . . 24
3.2.1 Phantom study . . . 24
3.2.1.1 Object size and motion period . . . 24
3.2.1.2 Offset vs. centered detector configuration . . . 29
3.2.1.3 Number of respiratory phases . . . 36
3.2.1.4 Smoothing filter in image reconstruction . . . 38
3.2.2 Patient Study . . . 40
3.3 Discussion . . . 44

4 4D-VOI Reconstruction 46
4.1 Methods . . . 46
4.1.1 Algorithm specification . . . 46
4.1.2 Mathematical phantom study . . . 49
4.1.3 Dynamic chest phantom study . . . 52
4.1.4 Patient studies . . . 52
4.1.5 Image quality comparison of 4D-VOI and reference reconstruction algorithms . . . 53
4.2 Results . . . 54
4.2.1 Mathematical phantom . . . 54
4.2.2 Dynamic chest phantom . . . 61
4.2.3 Motion assessment in phantom study . . . 65
4.2.4 Patient studies . . . 67
4.3 Discussion . . . 72

5 Iterative 4D-VOI Reconstruction **74**
5.1 Methods . . . 74
5.1.1 Algorithm specification . . . 74
5.1.2 Reconstruction algorithm evaluation . . . 77
5.1.3 Mathematical phantom study . . . 78
5.1.4 Patient studies . . . 78
5.2 Results . . . 81
5.2.1 Mathematical phantom study . . . 81
5.2.2 Patient studies . . . 86
5.2.3 Reconstruction times . . . 93
5.3 Discussion . . . 94

6 Summary **97**
6.1 Concluding statement . . . 98

Appendix A Fast image reconstruction implementation using GPU hardware **99**
A.1 Methods . . . 101
A.2 Results . . . 104
A.3 Discussion . . . 106

References **109**

Vita **118**

List of Figures

2.1 Comparison of average CBCT and 4D-CBCT 10
2.2 4D-CBCT process flow 10
2.3 Sparse and irregular 4D-CBCT sampling 11
2.4 4D-CBCT undersampling artifacts example 12

3.1 Artifacts vs. scan time - 3 s motion period 24
3.2 Artifacts vs. scan time - 6 s motion period 25
3.3 Measured trajectories for various scan times and motion periods . . . 26
3.4 Trajectory measurement errors (1) 27
3.5 Trajectory measurement errors (2) 28
3.6 Centered vs. offset detector reconstructions (1) 30
3.7 Centered vs. offset detector reconstructions (2) 31
3.8 Centered vs. offset detector reconstructions (3) 32
3.9 Centered vs. offset detector reconstructions (4) 33
3.10 Centered vs. offset detector trajectory measurement errors 34
3.11 Trajectory measurement errors - offset detector (1) 35
3.12 Trajectory measurement errors - offset detector (2) 36
3.13 Reconstructions using different number of phases 37
3.14 Trajectory measurement errors using different number of phases . . . 38
3.15 Reconstructions using different filters 39
3.16 Trajectory measurement errors using different reconstruction filters . 40
3.17 Patient dataset reconstructions for various scan times 41
3.18 Measured target trajectories - patient dataset 42
3.19 Trajectory measurement errors - lung tumor 43

3.20 Trajectory measurement errors - lung calcification 43

4.1 Cone-beam CT geometry 47
4.2 Mathematical motion phantom 50
4.3 Mathematical phantom ROI and line profile specification 51
4.4 Dynamic ROI reconstructions - simulation study 56
4.5 Mathematical phantom reconstructions - 0% phase line profiles 57
4.6 Mathematical phantom line profiles - 25% phase line profiles 58
4.7 Mathematical phantom line profiles - 50% phase line profiles 59
4.8 Mathematical phantom line profiles - comparison to motion-averaged reconstruction 60
4.9 Mathematical phantom reconstructions - RMS errors 61
4.10 4D-VOI Chest phantom reconstruction (1) 62
4.11 4D-VOI Chest phantom reconstruction (2) 63
4.12 4D-VOI Chest phantom reconstruction - edges 63
4.13 Chest phantom line profile specification 66
4.14 Chest phantom 4D-VOI reconstruction - line profiles 66
4.15 Chest phantom MB reconstruction - line profiles 66
4.16 4D-VOI reconstruction - Patient 1, axial format 67
4.17 4D-VOI reconstruction - Patient 1, coronal format 68
4.18 4D-VOI reconstruction - Patient 1, edges 68
4.19 4D-VOI reconstruction - Patient 2, axial format 69
4.20 4D-VOI reconstruction - Patient 2, coronal format 69
4.21 4D-VOI reconstruction - Patient 2, edges 70

5.1 I4D-VOI: mathematical phantom reconstruction 82
5.2 Mathematical phantom ROI and line profile specification 84
5.3 Mathematical phantom reconstruction - line profiles 85
5.4 I4D-VOI reconstruction - Patient 1, coronal 87
5.5 I4D-VOI reconstruction - Patient 1, axial 88
5.6 I4D-VOI reconstruction - Patient 1, lung calcification 89
5.7 I4D-VOI reconstruction - Patient 2, coronal 91
5.8 I4D-VOI reconstruction - Patient 2, axial 92

A.1 Computational profile of steps in reconstruction 105
A.2 Scaling of performance with GPU size 106

List of Tables

4.1 Mathematical motion phantom parameters 51
4.2 Mathematical phantom simulation parameters 51
4.3 Names adopted for the reconstructions in the mathematical phantom study 55

5.1 I4D-VOI patient studies parameters 80
5.2 Mathematical phantom reconstruction - RMS errors 84
5.3 Mathematical phantom reconstruction - streak artifact measurements 85
5.4 I4D-VOI reconstruction times 93

6.1 Qualitative description of reconstructions 98

A.1 List of tested GPUs and their specifications 103
A.2 GPU reconstruction times 105

List of Abbreviations

4D-CBCT	Four-Dimensional Cone-Beam Computed Tomography
4D-CT	Four-Dimensional Computed Tomography
4D-VOI	Four-Dimensional Volume-of-Interest reconstruction
ART	Algebraic Reconstruction Technique
ASD-POCS	Adaptive Steepest Descent - Projection Onto Convex Sets reconstruction
CBCT	Cone-beam Computed Tomography
CNR	Contrast-to-Noise Ratio
CPU	Central Processing Unit
CT	Computed Tomography
CTV	Clinical Tumor Volume
FBP	Filtered Back-Projection reconstruction
FOV	Field Of View
FWHM	Full-Width Half Maximum
GPU	Graphics Processing Unit
GTV	Gross Tumor Volume
I4D-VOI	Iterative Four-dimensional Volume-of-Interest reconstruction

IEC	International Electrotechnical Commission
IGRT	Image-Guided Radiation Therapy
IGTV	Internal Gross Tumor Volume
ITV	Internal Target Volume
Linac	Linear Accelerator
MB	McKinnon-Bates
MIP	Maximum Intensity Projection
NEMA	National Electrical Manufacturers Association
OBI	On-Board Imager
PICCS	Prior Image-Constrained Compressed Sensing reconstruction
PTV	Planning Target Volume
RMS	Root Mean Square
RMSE	Root-Mean-Square Error
ROI	Region Of Interest
RPM	Real-Time Position Management system
SART	Simultaneous Algebraic Reconstruction Technique
SNR	Signal-to-Noise Ratio
TV	Total Variation
VOI	Volume Of Interest
Voxel	Volume Element
XRT	External Beam Radiation Therapy

Chapter 1

Introduction

Lung cancer is the most prevalent cancer worldwide in terms of both incidence and mortality [1]. A standard of care in lung cancer treatment is radiation therapy, in which high energy x-ray beams are directed from outside the patient to lung tumors. The radiation beams are designed such that a lethal radiation dose is delivered to the target, while a minimal dose is delivered to healthy tissue.

One difficulty in radiation therapy of lung cancer is managing respiratory motion. Lung tumors move with the expansion and contraction of the lungs as a patient breathes, increasing the likelihood that the radiation beams miss their target and deliver the radiation dose to the wrong region. According to Liu *et al.*, more than 10% of all patients with lung cancer have tumors that move more than 1 cm due to respiratory motion [2]. This is considered to be a significant amount of respiratory motion, for which a motion management strategy is needed.

Four-dimensional cone-beam computed tomography (4D-CBCT) has been proposed as an imaging method for validating the target motion prior to radiation therapy. Experimental 4D-CBCT has scan times that are too long for practical clinical use. The scan time should be between 1 and 2 minutes for clinical application; however, at this short scan time, 4D-CBCT imaging is degraded by undersampling

artifacts. These artifacts may introduce errors in localizing the moving target. This dissertation presents improvements in 4D-CBCT for resolving targets undergoing respiratory motion with 1 to 2 minutes scan time. The Hypothesis and Specific Aims of this dissertation are presented next.

1.1 Hypothesis

Image quality in four-dimensional cone-beam computed tomography with acquisition times less than 2 minutes can be improved by acquisition optimization and by new image reconstruction methods.

1.2 Specific Aims

Aim I

To quantify the trade-off between scan time and image quality in 4D-CBCT, especially at scan times under 2 minutes.

Aim II

To develop new image reconstruction algorithms to reduce undersampling artifacts in 4D-CBCT with short scan time.

1.3 Significance

This research improves 4D-CBCT with shorter, more practical scan times, enabling wider adoption of 4D-CBCT. Radiation therapy patients with highly mobile lung tumors may gain the most from 4D-CBCT. In these cases, conventional CBCT pro-

duces images that are blurred by motion, making it difficult to localize the target. By resolving the target motion, 4D-CBCT may provide several clinical benefits.

First, the target localization uncertainty is reduced using 4D-CBCT for tumors undergoing respiratory motion [3].

Second, any prior knowledge or patient-specific models of target motion can be validated with 4D-CBCT for safety assurance. The current standard of practice does not use time-resolved imaging for IGRT. If the target motion measured in 4D-CBCT at the time of treatment differs significantly from the motion model used in treatment planning, an update of the treatment plan can be prompted. This is important because respiratory changes may occur after treatment planning or during the treatment regimen [4].

Third, 4D-CBCT may enable improved treatment strategies. For instance, gated therapy has been proposed to treat the target at a specific phase of the breathing cycle. Gated therapy could provide favorable dose distributions [5, 6]. Using 4D-CBCT, a more accurate positioning could be performed for gated therapy.

The 4D-CBCT improvements in this dissertation are also advances toward real-time 4D image-guidance in radiation therapy. Although this dissertation focuses on imaging performed immediately prior to treatment, the proposed methods could also be applied to sparsely sampled data acquired *during* treatment.

To summarize, the main benefit of 4D-CBCT is to allow visualization of the tumor in the presence of respiratory motion, which may lead to greater treatment accuracy. Treatment accuracy is important for tumor control and minimum injury to healthy lung tissue [7]. Because lung cancer patients already have poor lung function, they can hardly tolerate further damage to healthy lung tissue. The potential impact is that fewer patients would have side effects or respiratory complications resulting from radiation therapy.

1.4 Dissertation organization

The remaining chapters of this dissertation are organized as follows: Chapter 2 introduces background concepts in image-guided radiation therapy and previous work in 4D-CBCT. Chapter 3 addresses Aim I and presents the optimization of 4D-CBCT data acquisition. Chapters 4 and 5 address Aim II and present new image reconstruction methods for short 4D-CBCT scan times. Chapter 4 presents a new "4D-VOI" reconstruction that improves image quality by restricting the temporal resolution requirement to only a volume-of-interest (VOI). Chapter 5 presents the new "iterative 4D-VOI" reconstruction which further improves upon the reconstruction of Chapter 4. Chapter 6 summarizes the results and comments on the completion of the Specific Aims of this dissertation. Lastly, an appendix is provided which describes the fast computational implementation of the reconstructions in this dissertation on graphics processing units.

Chapter 2

Background and previous work

This chapter provides the background information for this dissertation. Section 2.1 introduces basic radiation therapy concepts including motion management. Section 2.2 describes image-guidance in radiation therapy and introduces 4D-CBCT. Section 2.3 outlines the challenges in 4D-CBCT. Last, Section 2.4 presents previous work in the development and improvement of 4D-CBCT.

2.1 Radiation therapy

Therapy using ionizing radiation is widely used in the treatment of cancer. Radiation damages the DNA within target cells so that they cannot effectively divide, resulting in their death during the mitosis stage of the cell cycle [8]. The most widely-used form of radiation therapy is external beam radiotherapy (XRT), in which high-energy x-ray beams are produced outside of the patient by a linear accelerator (linac) and aimed at the tumor within the patient [9]. It is often preferred over surgery and chemotherapy as a non-invasive and precise method of attacking cancer cells. High-energy x-rays (1 MeV or greater) penetrate through skin and outer tissues to deposit destructive energy (radiation dose) in tumors. When many such beams are aimed at the tumor

from different angles, the tumor cells receive the highest percent of radiation dose and the peripheral healthy tissue is spared [10]. With further refinements in modern XRT technology, the radiation dose is conformed to the shape of the target [11].

2.1.1 Treatment planning

The energy, orientation angles, and shapes of radiation beams are planned so that a prescribed amount of radiation damage is inflicted upon the target, while the damage to healthy tissue is minimized. This planning process depends on CT imaging to map the internal patient anatomy and the location of the target tumor. A CT imaging exam produces three-dimensional images of the patient that are used to plan the radiation treatment. This process is known as a "CT simulation" because the CT images are used in a computer simulation of the treatment geometry. Radiation doses to the tumor and relevant organs are calculated. The planning CT is not to be confused with image-guidance in radiation therapy which is explained in Section 2.2.

2.1.2 Motion management and 4D-CT

Respiratory motion becomes an important factor in many treatments of lung cancer. More than 10% of all lung cancer patients receiving radiation therapy exhibit a tumor motion greater than 1 cm [2]. Before imaging became available to measure the patient-specific target motion, an extra population-based margin (planning target volume expansion [12]) was added to the gross tumor volume to ensure 100% coverage of the tumor in the presence of motion. This conservative approach ensures that the target receives the prescribed radiation dose, but also increases the damage to healthy lung tissue. It is more desirable to use a *patient-specific* model of tumor motion to design more accurate treatment volumes. For this purpose, 4D-CT imaging simulation was invented in which images are acquired over multiple respiratory cycles and a time

series of volumetric images are produced [13, 14]. The "4D" in this name refers to three spatial plus the extra temporal dimension.

There are several motion management strategies possible with a motion model from 4D-CT:

1. Patient-specific safety margins - With a motion model, an internal target volume (ITV) can be defined that confines the target tumor during respiration, thereby minimizing the amount of healthy tissue in the target volume [15].

2. Respiratory-gated therapy - The radiation treatment beam is turned on only during a specific respiratory phase [5, 16]. This allows the treatment volume to be as small as possible to avoid normal tissue damage.

3. Respiratory motion tracking - Radiation beam actively tracks the target along its respiratory motion path [17]. This also minimizes the treatment volume, but is more time-efficient than respiratory-gated therapy. However, this method is not widely used because of the unpredictable interplay effect between the beam steering and the tumor motion, which may compromise target coverage.

Although a target motion model is clearly preferable over no motion model, the patient's respiration may change over the course of a radiotherapy regimen; therefore imaging methods for verifying the motion model at the treatment session are needed.

2.2 Image-guidance in radiation therapy

Because the radiation dose distribution in the patient is calculated in a computer simulation of radiation physics, it is imperative that the actual treatment position is matched to the position in the simulation. The patient position relative to the radiation beams must be replicated accurately. External landmarks such as radio-opaque markers or tattoos on the patient's skin can be used to match the treatment

setup to the simulation setup. However, skin and other external landmarks are only surrogates of the internal target position. More precise positioning is possible with imaging of internal anatomy. Radiation therapy using imaging for patient positioning is referred to as image-guided radiation therapy (IGRT). IGRT reduces the amount of setup margin added to treatment volumes, sparing more healthy tissue [18].

2.2.1 Cone-beam computed tomography

IGRT has been performed using x-ray projection images. Although the internal anatomy is visible in x-ray projection imaging, only a two-dimensional image is available. Also, as in all projection radiography, contrast in this image is reduced by superimposed anatomy. In the last 12 years, three-dimensional imaging technology has become available in the treatment room via cone-beam computed tomography (CBCT) [19, 20]. In CBCT, an imaging system comprised of a flat-panel detector [21, 22] and an x-ray source is integrated into the treatment linac. This system acquires x-ray projection images of a size close to or larger than an average human thorax. The x-ray source and detector rotate in a circular trajectory around the patient and acquire typically 600 projections from different view angles in one rotation. These projection data are then processed by a computer, in which an image reconstruction program creates three-dimensional tomography images. The CBCT images are used for precise patient positioning in three dimensions. Overall, online CBCT imaging has improved the positioning accuracy in IGRT as compared to image guidance with 2D projection imaging [23].

The reconstructed images in conventional CBCT lack temporal resolution because they are reconstructed from data taken over a time scale of approximately 1 minute. (This is unlike dedicated CT scanners which reconstruct time-resolved images from data taken over approximately 0.5 s.) The CBCT scan time is much longer than

an average breath cycle (3-6 s); therefore, CBCT images of the thorax are degraded by motion artifacts. Conventional CBCT images show motion blurring and the tumor boundary is not clearly resolved. The tumor motion cannot be measured in a conventional CBCT scan because it is averaged out in the data acquisition. This is undesirable for targeting tumors with a large degree of motion (1 cm or greater).

2.2.2 Four-dimensional CBCT

Four-dimensional cone-beam computed-tomography (4D-CBCT) has been developed for images of the tumor phase-by-phase through the respiratory cycle without motion blurring, so that the tumor boundary is enhanced. An example comparing motion-averaged (conventional) CBCT and 4D-CBCT is provided in Figure 2.1. The tumor motion can be measured to verify the motion model used in treatment planning.

The method by which 4D-CBCT produces respiratory phase-resolved images is explained as follows: During projection data acquisition, the patient's breathing is monitored and a respiration signal is acquired. This signal is used to sort the projection data into groups corresponding to respiration phases. The projection data in each of these subsets are used to reconstruct separate tomographic images at each respiration phase. The 4D-CBCT process flow is illustrated in Figure 2.2. The final output is essentially a 4D tomographic movie in which a tumor's respiratory motion is depicted in all three spatial dimensions and across the respiratory cycle. This is similar to the raw data phase-binning approach to 4D-CT therapy simulation imaging presented by Keall *et al.* [24].

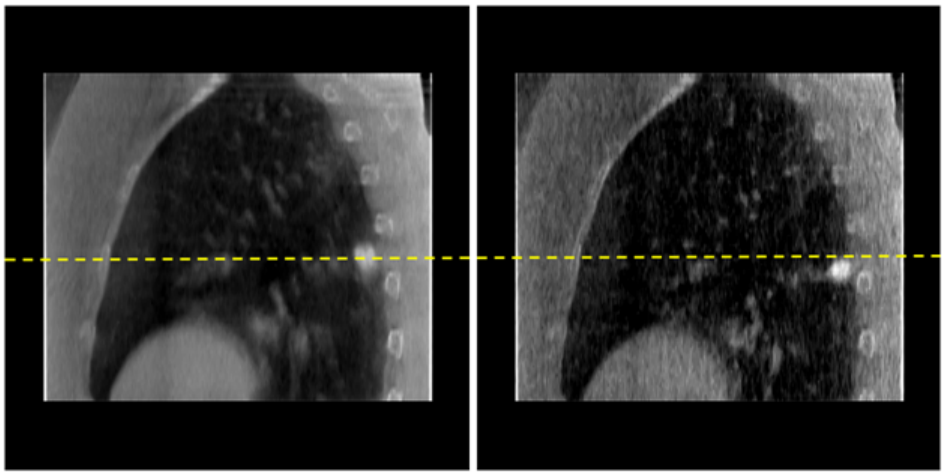

Figure 2.1: Comparison of average CBCT and 4D-CBCT. Left: average CBCT; Right: 4D-CBCT image at end-inhale. Both images were reconstructed from the same raw data.

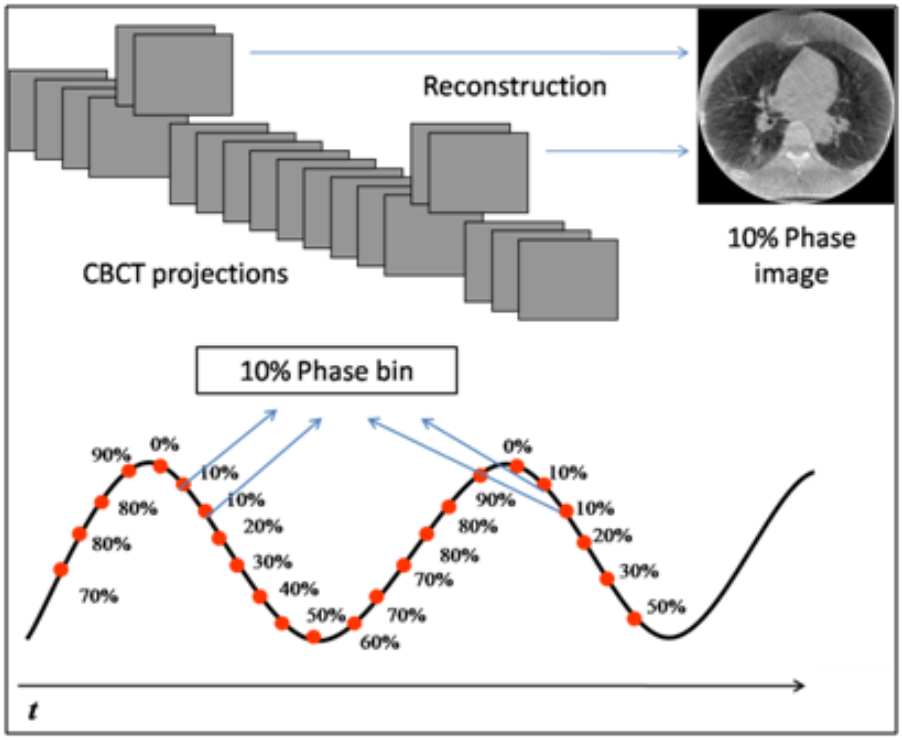

Figure 2.2: 4D-CBCT process flow - Cone-beam projections are sorted according to respiratory phase (10% phase show here). Phase-correlated images are for each phase.

2.3 Challenges in 4D-CBCT

Because 4D-CBCT involves sorting projections into respiratory phase subsets, there is a reduction in the number of projections available to reconstruct any particular phase. Furthermore, this projection data is irregularly sampled (see Figure 2.3 below). Note that the sorted projections group into "bunches", each bunch representing a different breath cycle. There are large spaces between bunches, which corresponds to missing projection data. The angular sampling is fundamentally limited by the number of breath cycles during the scan. With a 1-minute acquisition, 10–20 bunches are acquired for breathing cycles of 3–6 s.

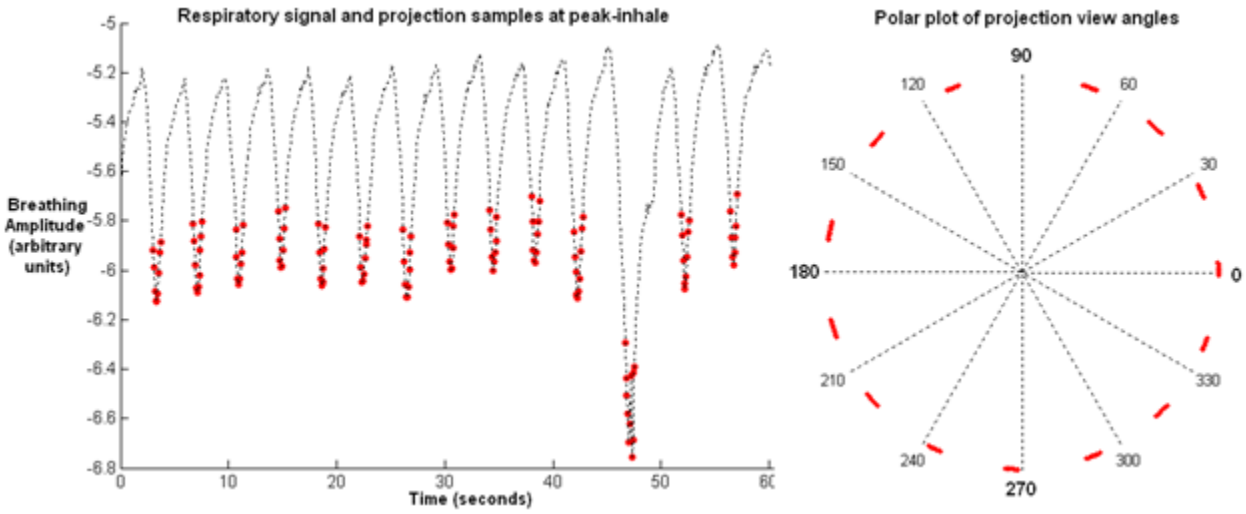

Figure 2.3: Sparse and irregular 4D-CBCT sampling - A 1-minute CBCT acquisition was performed on a patient. Left: patient respiratory signal annotated with projections taken at peak-inhale phase. Right: Angular distribution of projections at peak inhale phase. Note the sparse and irregular angular sampling of this projection data set. The projection data are sorted into "bunches."

The effect of this sparse and irregular sampling is view aliasing artifacts, which appear as streaks in axial format images [27]. In this dissertation, "view aliasing artifact", "undersampling artifact", and "streak artifact" are used interchangeably

with each other. An example of this artifact is shown in Figure 2.4. Aliasing is the misrepresentation of a high-frequency as a lower frequency. High frequency details such as boundaries are lost in view aliasing and edges appear jagged. Note the loss of these details in the spine and the large lung lesion in the image below.

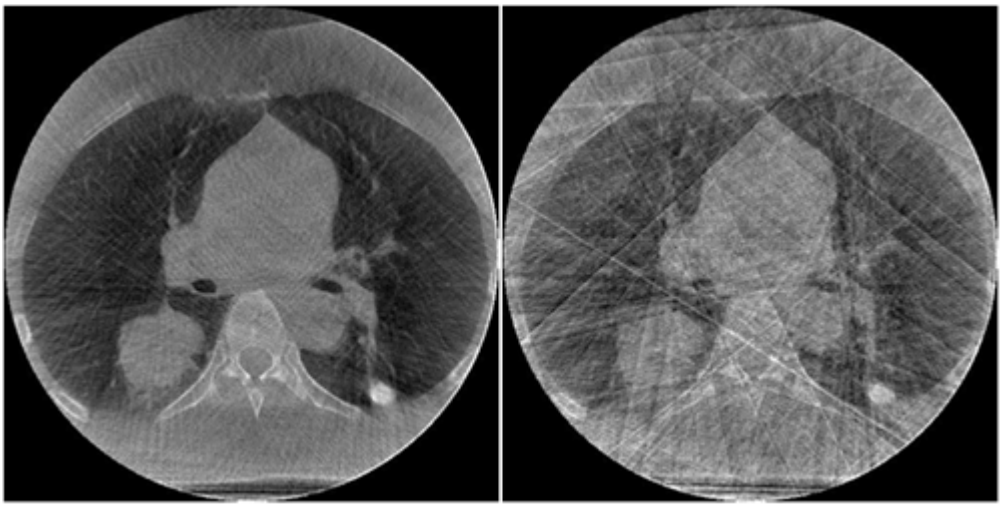

Figure 2.4: 4D-CBCT undersampling artifacts example - Left: Image reconstructed with adequate view angle sampling. Right: image reconstructed after removal of projections. Inadequate view sampling results in streak artifacts.

Image degrading mechanisms such as noise, low contrast, and artifacts can all affect image perception, but this dissertation is concerned with methods for reducing undersampling artifacts. Because of practical clinical scanning time limitation, clinical 4D-CBCT is undersampled and the main source of image degradation is undersampling artifacts. Undersampling artifacts become worse with shorter scan times as fewer projection data become available. The following questions arise with regard to sampling in 4D-CBCT:

- What minimum scan time is required to ensure that undersampling artifacts do not affect target motion measurement?

- Is there a minimum threshold scan time, below which the measurement accuracy

decreases abruptly?

- Is there a linear relationship between scan time and tumor boundary accuracy?

A rigorous study of optimizing 4D-CBCT scan time is needed.

Apart from acquisition optimization, the impact of streak artifacts may be reduced in image reconstruction. Image reconstruction strategies for specifically reducing undersampling artifacts in 4D-CBCT are needed.

2.4 Previous work

2.4.1 4D-CBCT sampling strategies

In one continuous gantry rotation, any given projection angle is sampled for only one particular respiratory phase and not for any other phase. For a standard 1-min/1-rotation acquisition in conventional CBCT, this causes large gaps in angular sampling within each phase and produces streak artifacts when the standard filtered back-projection image reconstruction is used.

To overcome the sampling problem, several acquisition strategies have been demonstrated. All of them involve increasing the scan time and the number of acquired projections. The following studies have demonstrated 4D-CBCT with different acquisition and sorting parameters. Lu *et al.* used a scan time of 3.3-6.6 min [25]. The gantry rotation speed and the total scan time were adapted to the patient's breathing to capture a constant number of breath cycles regardless of the breathing rate. Even with as high as 10 respiration phases, this scanning protocol resulted in negligible image artifacts. Sonke *et al.* demonstrated a 4-min acquisition protocol [26]. Li *et al.* described a protocol in which multiple gantry rotations are used to acquire sufficient projection data for 4D-CBCT [27]. Using a standard 1-min rotation speed

for 4 continuous rotations, an adequate amount of projection data were acquired for negligible undersampling artifacts. Each of these studies used the standard filtered back-projection reconstruction algorithm.

These studies have demonstrated sufficient data sampling, but there is no established lower limit for sampling. There has been no systematic investigation of view aliasing artifacts with short scan times, and their impact on target motion measurement.

2.4.2 Image reconstruction strategies

Various reconstruction algorithms have been proposed to address sparse-view sampling in CBCT and 4D-CBCT. Image reconstruction using a very few samples has been demonstrated through total-variation (TV) minimization algorithms such as adaptive steepest descent projection onto convex sets (ASD-POCS) [28, 29]. Prior image constrained compressed sensing (PICCS) uses a prior image constraint to improve the reconstruction accuracy and convergence speed [30, 31]. Both the TV minimization and PICCS algorithms regularize iterative reconstruction by assuming that solutions satisfy some sparsity constraint. Evaluations of the image quality, robustness, convergence, and computational aspects of these iterative reconstruction algorithms using sparse data were provided by Bergner *et al.* [32] and Bian *et al.* [33] The TV-minimization and PICCS are very promising algorithms for image reconstruction using sparsely sampled projection views, but as yet neither algorithm has been demonstrated appropriate for all sparse-data image reconstruction scenarios. One reason is that assumptions of image sparsity may not necessarily hold. Computational cost is another prohibitive factor. In IGRT, the image should be available immediately after acquisition. Pan *et al.* outlined several reasons (applicability, implementation challenges, and computational cost) why many iterative algorithms have

never been successfully incorporated into clinical CT systems [34]. There is a need for a computationally inexpensive image reconstruction algorithm that can reduce artifacts in undersampled 4D-CBCT.

Chapter 3

Acquisition Optimization

This chapter presents an evaluation of 4D-CBCT performance by assessing the accuracy of target motion measurements for various target sizes and motions. The results may serve as patient-specific guidelines for scan parameters selection in 4D-CBCT. The Methods, Results, figures and tables in this chapter were reprinted from Ahmad *et al.* [35] with permission from the *Medical Physics* journal.

As discussed in Chapter 2 several previous works have studied the relationship between scan time and image quality in 4D-CBCT. These works have assessed image quality using traditional image quality metrics such as signal-to-noise ratio (SNR), contrast-to-noise ratio (CNR), or image intensity error (in the case of phantom experiments). Qi and Chen (2011) have provided such an approach, conducting a 4D-CBCT performance study in which they measured the target motion trajectory using 4D-CBCT with various scan parameters [36]. Although this study included several scan parameters and reconstruction algorithms, it assessed 4D-CBCT performance for only one object and only one object motion.

Intuitively, one expects measuring the trajectory of a smaller object to be more difficult than for a larger one when there are streaky under-sampling artifacts. It is also known that longer respiration periods are associated with greater streak artifacts

in 4D-CBCT [37]; one then expects greater errors in tracking small targets with long respiration periods. Because of these dependencies on target characteristics, it is proposed that 4D-CBCT scan parameters can be further optimized on a patient-specific basis. For example, Lu *et al.* (2007) [25] and Li and Xing (2007) [37] have previously suggested setting gantry rotation speed based on the patient breathing period.

In this work, the 4D-CBCT performance was compared for various object sizes and motion trajectories. The performance was assessed by the accuracy of target motion trajectories in phantom data using an automatic measurement method. For each object size and motion, image datasets were acquired using various combinations of scan parameters including scan time, number of 4D-CBCT phases, reconstruction parameters, and detector configurations. The purpose was to optimize scan parameters for a given target size and motion. Lastly, the phantom study results were supported with a patient study.

3.1 Methods

The influence of object size and motion on the accuracy of target trajectory measurement in 4D-CBCT was assessed. Although the object characteristics cannot be selected in a patient exam, they can be controlled in a phantom study. Therefore a phantom study was designed to test various object sizes and motion periods. For each object size and motion, various combinations of scan parameters were used. The most important scan parameter was the scan time, because it directly affected the amount of data available to the task of tracking target motion. Other parameters were the number of phases used to sort the projection data, the detector configuration (centered or offset detector), and the smoothing filter used in the image reconstruction. The last two parameters are described in subsections 3.1.1 and 3.1.2. All of the ex-

periments were performed using the Varian OBI system (Varian Medical Systems, Palo Alto, CA).

3.1.1 Offset vs. Centered Detector Configuration

Two different detector configurations were used: offset and centered detector. Offset detector configuration is often used in clinical CBCT of the thorax or abdomen to enlarge the field-of-view (FOV) for a given size flat-panel detector [38]. Although the FOV is increased without increasing the size of the detector, a trade-off is made in sacrificing half of the x-ray fan data. Another trade-off is that a 360° rotation with a centered detector provides redundant data. Because of the popularity of the offset detector configuration, it was included in this experiment.

The offset detector was shifted by 14.8 cm. The centered detector provided a 25-cm FOV, whereas the offset detector provided a 45-cm FOV. For the centered detector, the projection data were acquired over π-plus-fan angle range (200°), whereas for the offset detector, they were acquired over a full 360° rotation (a full 360° required for offset detector). The 200° was sufficient for the centered detector configuration. On the other hand, some redundant data would be collected from complementary projection angles in a 360° scan in the centered detector configuration.

3.1.2 Image Reconstruction

In this work, the standard Feldkamp filtered back-projection (FBP) was used for image reconstruction. Feldkamp reconstruction is simply the modification of 2D (planar) filtered back-projection to 3D cone-beam geometry in CBCT [39]. In 4D-CBCT, each phase was reconstructed independently using the Feldkamp reconstruction. It is important to emphasize here that many reconstruction algorithms often perform better than filtered back-projection for under-sampled data. Most notable are al-

gorithms based on total-variation (TV) minimization [28, 40, 41, 29, 42]. These algorithms have produced superior image quality results in both phantom and patient data. However, no single algorithm has been proved superior over others for all clinically imaged objects and situations. Consequently, filtered back-projection remains the only clinically-used image reconstruction algorithm in CBCT. Another reason for choosing FBP is that imaging phantoms are biased in favor of TV minimization algorithms because they are usually piecewise constant. TV minimization prefers piecewise constant solutions and is not appropriate for the phantom study in this work.

The performance of smoothing reconstruction filters on the measured trajectory was tested. The purpose of this part of the experiment was to determine whether reconstruction filters affect the motion measurement and whether the filter should be set based on object characteristics. For this part of the experiment, the following Butterworth low-pass filters [43] were used:

1. No smoothing: pure ramp filter,

2. Medium smoothing: ramp filter with a Butterworth window with a cutoff of 20% of the Nyquist frequency and order n = 5,

3. Heavy smoothing: ramp filter with a Butterworth window with a cutoff of 10% of the Nyquist frequency and order n = 5.

For this system, the detector spacing was 0.388 mm and the Nyquist frequency was 1.29 line pairs/mm. The medium smoothing filter above provides smoothing similar to typical clinical CBCT.

3.1.3 Phantom Study

The IEC NEMA body phantom was used in this experiment. There were six spheres of 10, 13, 17, 22, 28, and 37 mm diameters in this phantom to simulate different size lung tumors. The phantom was set on a sliding motion platform set to move in a periodic motion along the longitudinal direction of the scanner. Two different motion profiles were used: a 3-s motion period and a 6-s motion period. Most patient respiratory cycle durations are between 3 and 6 s [14]. A 2-cm motion amplitude was selected to simulate plausible lung tumor motion amplitude, particularly for lesions in the lower lobe [44]. Also, a 2-cm motion is one that benefits from a motion management strategy. A 3-m scan of the phantom was acquired for both the 3-s and 6-s motion profiles. The Varian Real-time Position Management (RPM) system was used to acquire a respiratory signal during the x-ray acquisition, which was used to sort the projection data into phases.

Starting with the 3-m scan data, shorter scans were simulated by removing projection data. The data were removed in such a way as to maintain a realistic number of motion cycles for the shorter scans. For instance, removing the data for every alternating cycle represents an acquisition with half of the scan time. By reducing projection data by factors of 1/2, 1/3, 1/4, 1/5, and 1/6, scan times of 1.5 m, 1 m, 45 s, 36 s, and 30 s were simulated. One advantage of simulating shorter scan times by removing projection data is that the different simulated scans come from the same actual scan and the images are inherently registered among the scans. The number of phases chosen was 2, 4, 8, and 16. These particular values were selected because they are multiples and their time points in the respiratory cycle are aligned relative to each other. All raw data were used, regardless of the number of phases. The trajectory of each sphere across the respiratory phases was measured using a rigid image registration method (section 3.1.5).

3.1.4 Patient study

A 4D-CBCT exam was performed of one lung cancer patient receiving radiotherapy. This patient had a large 40-mm diameter lung tumor in the posterior right lung that moved with a 2.8-s breathing cycle. This patient also had a 10-mm diameter calcified plaque in the posterior left lung. The patient was scanned with a 4.5-m scan time. Using this original 4.5-m scan, shorter scan times were simulated by reducing projection data in the same manner as for the phantom experiment and obtained six different scan times: 45 s, 54 s, 68 s, 1.5 m, 2.25 m, and 4.5 m. The Varian RPM system was used to acquire the respiratory signal for this patient. The RPM data were used to sort the projection data into 2, 4, and 8 phases and reconstruct 4D image sets. A higher number of phases (e.g. 16, as in the phantom study) was not used because the projection sampling rate for this patient study did not support more than 10 phases. Using the 4D-CBCT image data, the trajectories of both the lung tumor and the calcified plaque were measured for different scan times and number of phases.

The tumor trajectory was measured using a deformable image registration method (section 3.1.5). Although the "true" trajectory was not known for accuracy assessment, the trajectory measured from the 4.5-m scan served as the gold standard. The accuracy of the trajectories measured using various scan times was compared against this standard.

3.1.5 Measurement of image trajectory

The trajectory of the target was measured as it moved through the respiratory cycle. The location of a target in any given phase relative to a reference phase was measured using image registration. By determining the position of the target relative to the position in reference phase in all the phases in the 4D image set, the target trajectory

was measured. The following describes the image registration method used:

For the phantom data, a rigid translation-only image registration based on minimizing image intensity difference was used. This minimization problem was solved using the Levenberg-Marquardt algorithm [45, 46, 47], which performs small shifts in displacement until the intensity difference is minimized. The displacement c was initialized to zero. For the patient data, the trajectories were measured using deformable image registration instead of rigid registration. The registration method proposed by Lu *et al.* (2004) based on the calculus of variations was used [48]. This registration also was an intensity-based approach. This deformable image registration method was also used by Qi and Chen (2011) to extract motion trajectories in 4D-CBCT [36, 49]. For both rigid and deformable registration, one phase in the 4D image set was chosen as the reference phase, and the relative target displacement in each of the other phases to the reference phase were measured. To avoid false local minimum solutions, a multi-resolution strategy was used in which the registration is first performed on low resolution images and the registration result becomes the starting point to the successively higher resolution registrations. In this work, four resolution levels were used for the rigid registration and six levels for the deformable registration. The registration result for one phase was used as the initial estimate for the registration of the next phase. (e.g. the registration of Phase 2 to Phase 1 was used as the initial estimate for the registration of Phase 3 to Phase 1, and so forth. Phase 1 was the reference phase image.)

Once the trajectory was measured, the error for all points along the trajectory was computed by comparison with the true trajectory. The errors in the points along the trajectory were summarized using a root-mean-square (RMS) Error metric:

$$RMS\ Error = \sqrt{\frac{1}{n-1}\sum_{i}\left|\vec{r}_m{}^{i} - \vec{r}_t{}^{i}\right|^2} \quad , \tag{3.1}$$

where $\vec{r}_m{}^i$ and $\vec{r}_t{}^i$ are the measured and true positions, respectively, of the object in the i^{th} phase. The variable n is the number of phases in the 4D-CBCT data set. The summation was performed over $n-1$ phases, while one phase was chosen as the reference phase in the image registration-based measurement.

3.1.5.1 Region-of-interest constraint in image registration

Because lung motion is complex, the task of measuring motion trajectories was simplified by restricting the image registrations (both rigid registration for the phantom and deformable registration for the patient) to a small volume of interest (VOI) containing the moving target. Within the VOI, the motion is simpler and approximately rigid with minimal rotation and deformation. For the phantom study, the 4D-maximum intensity projection (MIP) image was used to segment the motion envelope of the sphere. This VOI was expanded by 5 mm and used in the image registrations. This is a common margin added to delineated tumor volumes in lung cancer to account for target setup uncertainty and inter-fractional motion. With this margin, the moving spheres remained inside the VOI. For the patient study, a suitable VOI was already available in the form of the planning treatment volume (PTV) in the patient's radiation treatment plan [12]. In this case, the PTV included margins for microscopic extensions of disease (CTV margin) and also for setup uncertainties (PTV margin). These margins were chosen specifically for this patient by a radiation oncologist. The CTV and PTV margins added together were roughly 7-mm expansions around the tumor, which is somewhat larger than but close to the 5-mm margin used for the VOI in the phantom study.

3.2 Results

3.2.1 Phantom study

3.2.1.1 Object size and motion period

Images of the NEMA phantom for both 3-s and 6-s period motions at the end-exhale (50% phase) are shown in Figures 3.1 and 3.2 respectively. Both figures show images for various scan times from 30 s to 3 m, reconstructed using 8 phases. Not surprisingly, the streak artifacts from under-sampling increase as scan time is reduced. The streak artifacts are also worse for the 6-s motion than for the 3-s motion.

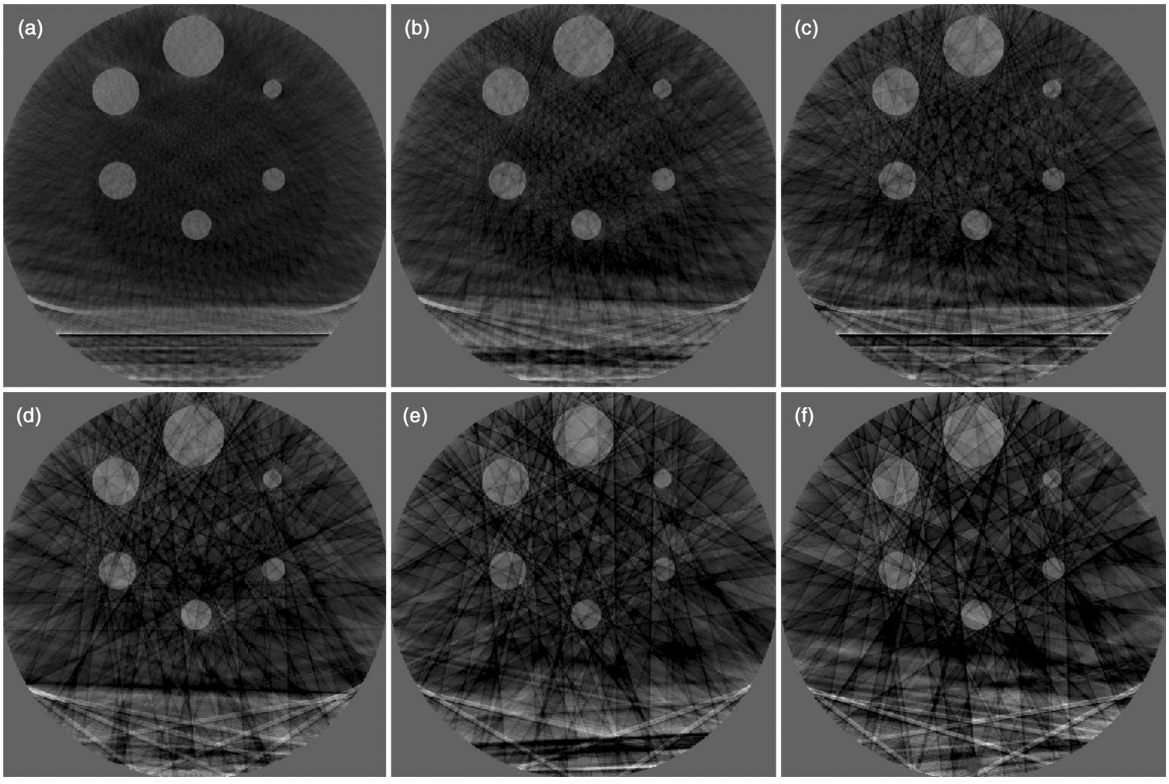

Figure 3.1: Reconstructions of the 3-s period NEMA motion phantom at 50% phase from data corresponding to different scan times: (a) 3 m, (b) 1.5 m, (c) 1 m, (d) 45 s, (e) 36 s, and (f) 30 s. Used with permission from *Medical Physics* journal (Ahmad and Pan, 2012) [35].

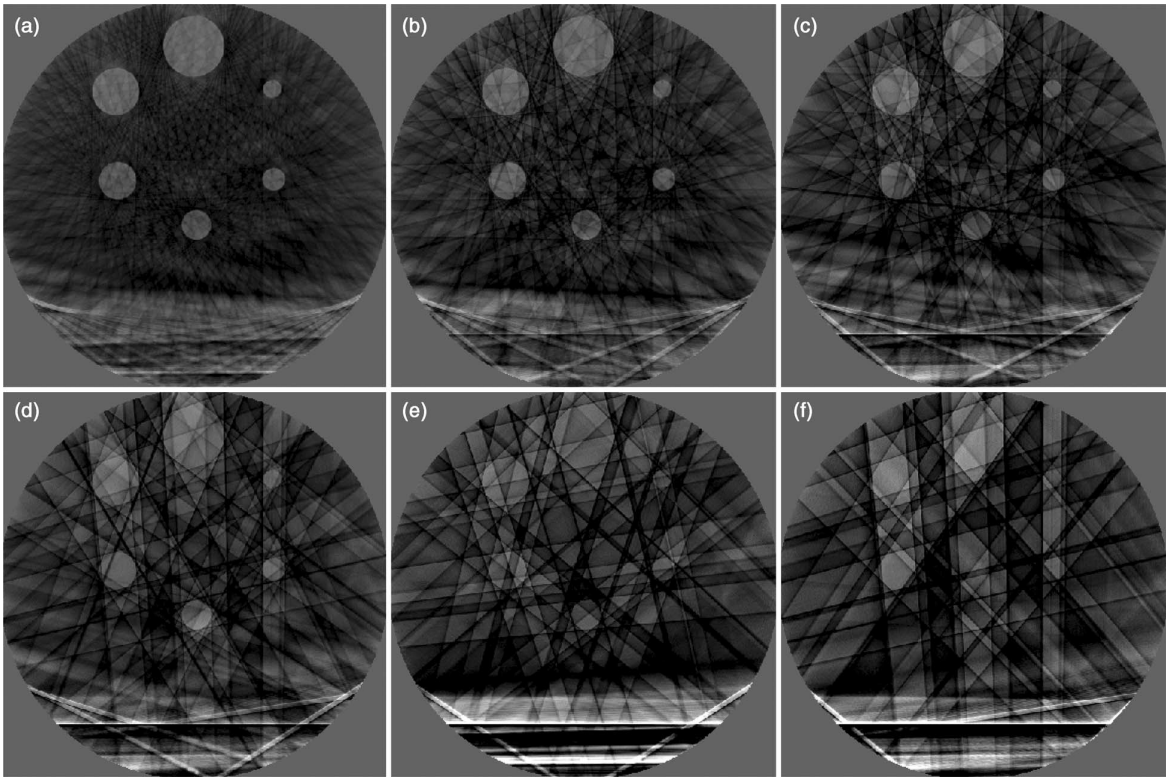

Figure 3.2: Reconstructions of the 6-s period NEMA motion phantom at 50% phase from data corresponding to different scan times: (a) 3 m, (b) 1.5 m, (c) 1 m, (d) 45 s, (e) 36 s, and (f) 30 s. Used with permission from *Medical Physics* journal (Ahmad *et al.*, 2012) [35].

For all 12 objects (6 sizes and 2 motion periods), the sphere motion trajectories were measured for the various scan times. The trajectory component in the longitudinal (z) direction for each object is shown in Figure 3.3. The number of respiratory phases was set to 16. The first major trend observed was that errors were consistently greater for the 6-s period than for the 3-s period for short scan times. For the 3-s period, the errors were all less than 2 mm (aside from one exception for the 13-mm sphere) for all scan times and sphere sizes, whereas large errors of 6 mm or greater were observed for spheres smaller than 22 mm with the 6-s period. This suggests that scan times can be set very short for 3-s breathing periods. For the 3-s period, the su-

perior angular sampling produced fewer streak artifacts and more accurate trajectory measurements than for the 6-s period. The second trend observed was that errors became smaller with increasing scan time. This was particularly true for 17-mm or smaller spheres with the 6-s period. A scan time of 1.5 m or greater always produced errors of less than 2 mm. The third trend observed was that larger objects were more accurately tracked. For the 28-mm or larger spheres, the scan time could be reduced to 45 s while keeping the error below 2.5 mm, regardless of period.

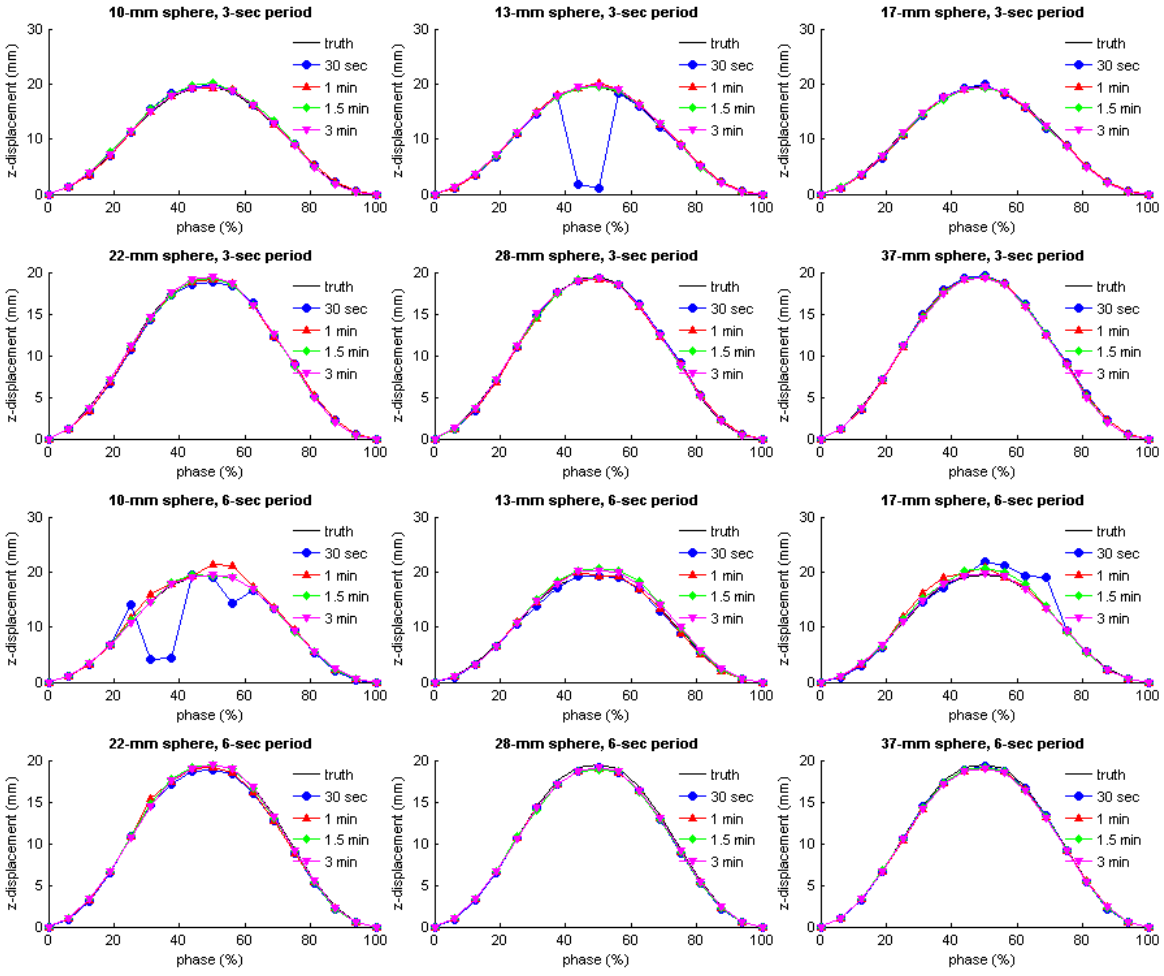

Figure 3.3: Measured trajectories of spheres of various sizes and motion periods using various scan times. Displacements along the longitudinal (z-axis) are plotted. Used with permission from *Medical Physics* journal (Ahmad and Pan, 2012) [35].

Figures 3.4 and 3.5 summarize the trajectory errors for different sphere sizes and scan times for a fixed motion period (either 3 s or 6 s). These figures display the observed trend of increasing error with smaller object size or scan time. Note that the observed trends were not absolute: in a few cases, errors decreased with smaller object size or scan time. These anomalies can be attributed to the random nature of streak artifacts; a streak artifact may intersect a sphere, causing a trajectory measurement error, or the artifact may not intersect the sphere. For increased confidence in the observed trends, a statistical analysis using many repeat acquisitions would need to be performed; insufficient data were acquired for such an analysis.

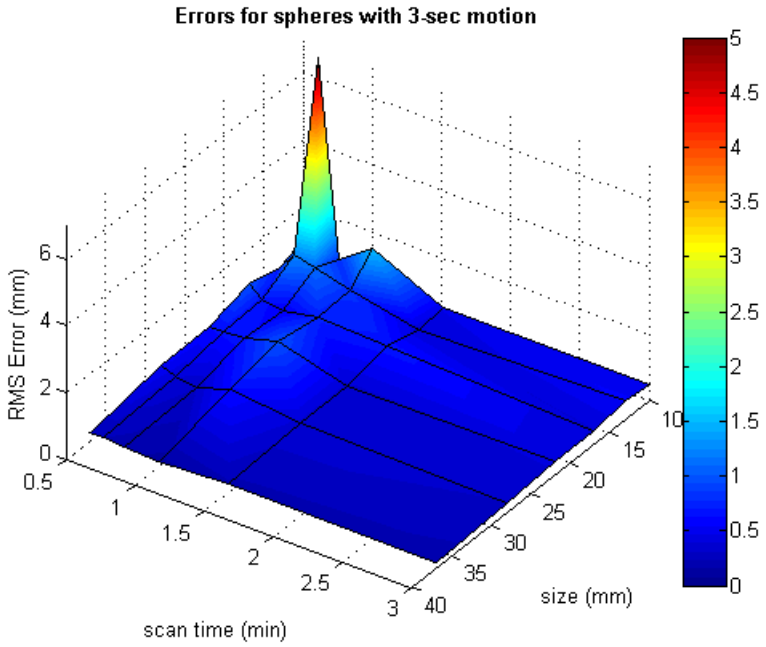

Figure 3.4: Root mean square (RMS) trajectory measurement errors of spheres of various sizes with 3-s motion. Used with permission from *Medical Physics* journal (Ahmad and Pan, 2012) [35].

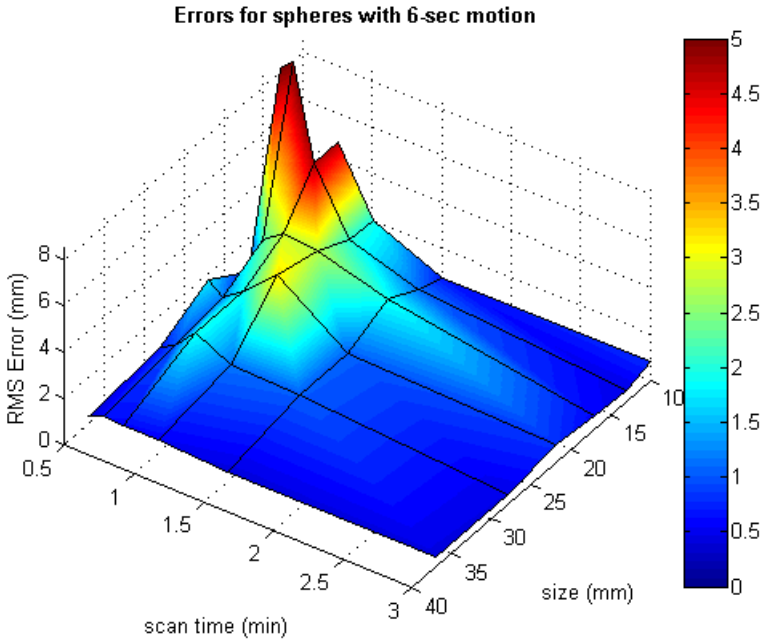

Figure 3.5: Root mean square (RMS) trajectory measurement errors of spheres of various sizes with 6-s motion. Used with permission from *Medical Physics* journal (Ahmad and Pan, 2012) [35].

One can use Figures 3.4 and 3.5 to optimize a 4D-CBCT acquisition in the following way: Select the appropriate figure based on the motion period. Then, for a given object size and scan time, find the expected trajectory measurement accuracy. Conversely, for a given object size and desired measurement accuracy, one can find the corresponding scan time on the horizontal axis. In this way, the user can minimize the 4D-CBCT scan time for desired measurement accuracy.

It is emphasized again that these results were obtained using the Feldkamp (FBP) image reconstruction algorithm. The errors are expected to be much less for iterative reconstruction using total-variation minimization. Because of the piecewise constant nature of the phantom, the quantitative image errors and, consequently, the registration errors are expected to be close to zero for all the targets and acquisition parameters in this study with total-variation minimization reconstruction.

3.2.1.2 Offset vs. centered detector configuration

Figures 3.6 to 3.9 show image reconstructions comparing the offset and centered detector configurations. The images with the larger field of view correspond to the offset detector configuration. All images are at the peak exhale phase. Figures 3.6 and 3.7 show the reconstructions for the phantom moving with 3-s period, scanned with 3-m and 1-m acquisitions respectively. Figures 3.8 and 3.9 show the reconstructions for the phantom moving with 6-s period, scanned with 3-m and 1-m acquisitions respectively. The offset detector images have slightly more streak artifacts than their centered detector counterparts, especially with 1-m acquisition. Figure 3.10 shows the errors in the measured sphere trajectories for these scans. The two detector configurations showed similar performance. (A useful point of reference is that a typical setup margin in IGRT is 3 mm. Errors less than 3 mm may be considered clinically insignificant.) The only time the performance of the offset and centered detectors showed clinically significant difference was for targets smaller than 20 mm scanned with acquisition time shorter than 1.5 m. Figure 3.11 (3-s motion) and Figure 3.12 (6-s motion) show plots that can be used to optimize the scan time for a desired trajectory measurement accuracy for a given object size using the offset detector configuration.

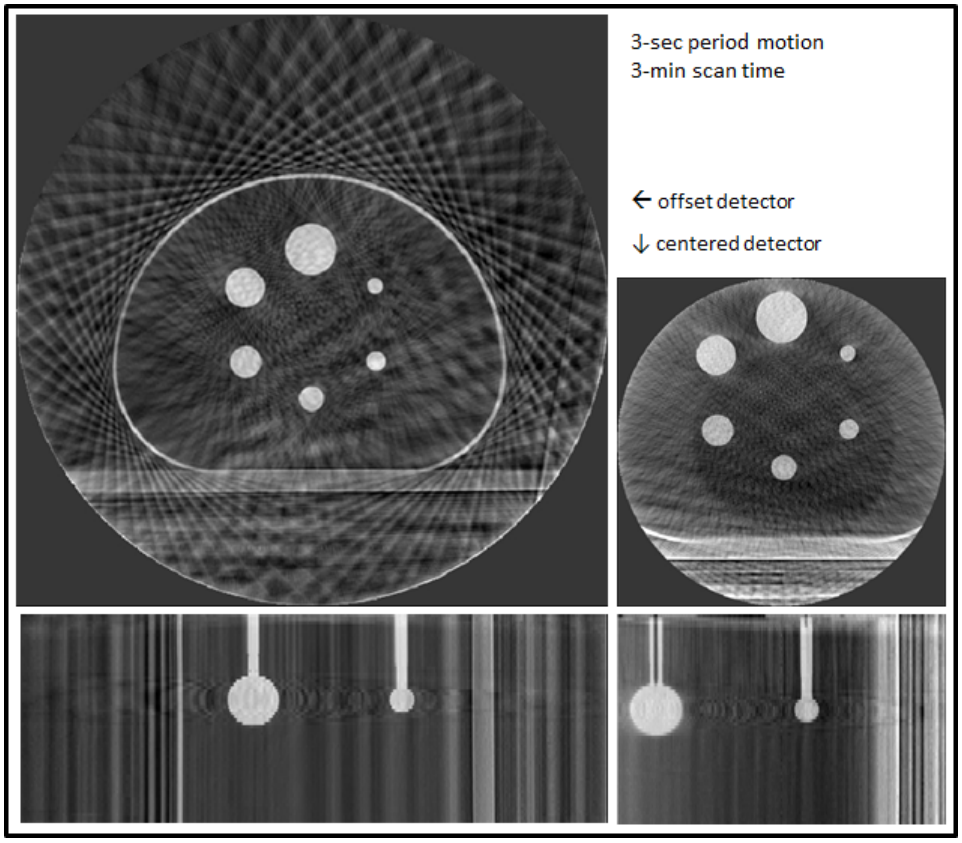

Figure 3.6: Centered and offset detector acquisitions for the 3-s motion period and 3-m scan time. Left column: offset detector, right column: centered detector, top row: axial views, bottom row: sagittal views. Used with permission from *Medical Physics* journal (Ahmad and Pan, 2012) [35].

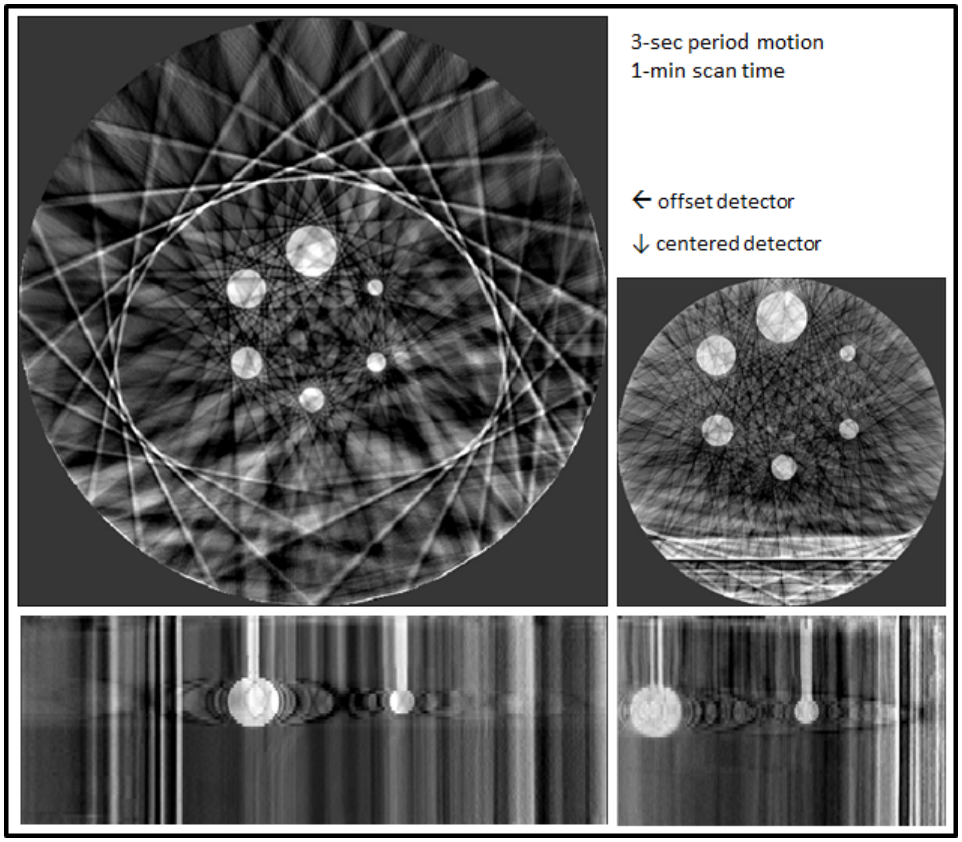

Figure 3.7: Centered and offset detector acquisitions for the 3-s motion period and 1-m scan time. Left column: offset detector, right column: centered detector, top row: axial views, bottom row: sagittal views. Used with permission from *Medical Physics* journal (Ahmad and Pan, 2012) [35].

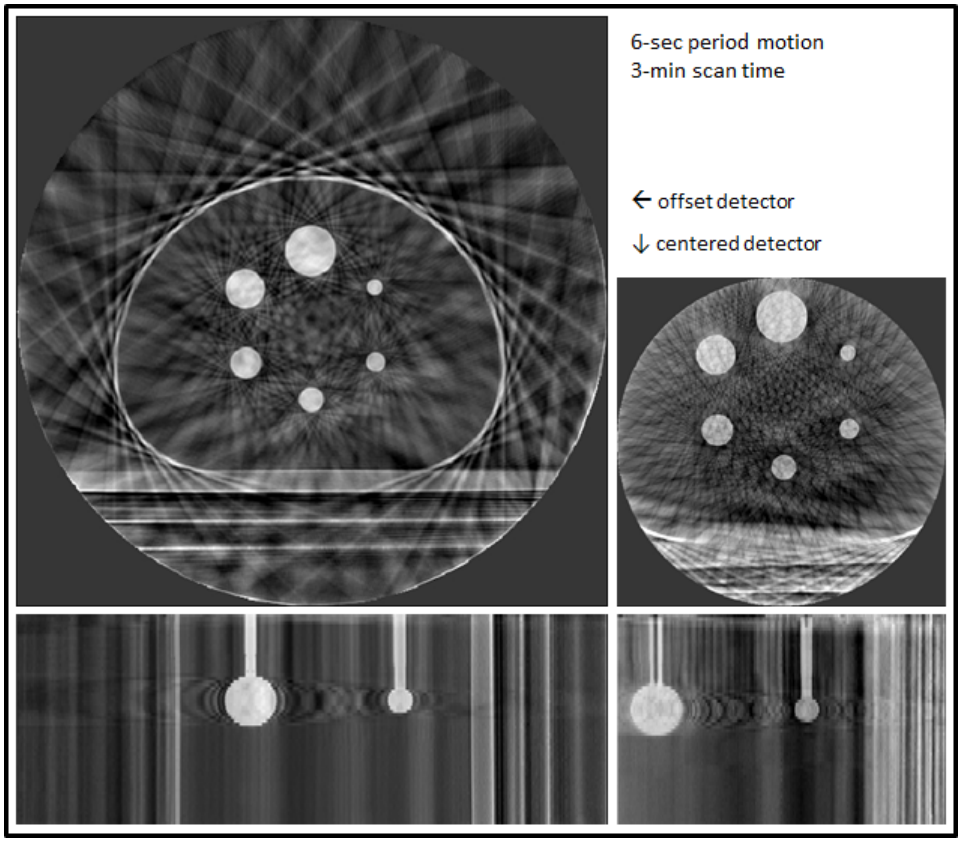

Figure 3.8: Centered and offset detector acquisitions for the 6-s motion period and 3-m scan time. Left column: offset detector, right column: centered detector, top row: axial views, bottom row: sagittal views. Used with permission from *Medical Physics* journal (Ahmad and Pan, 2012) [35].

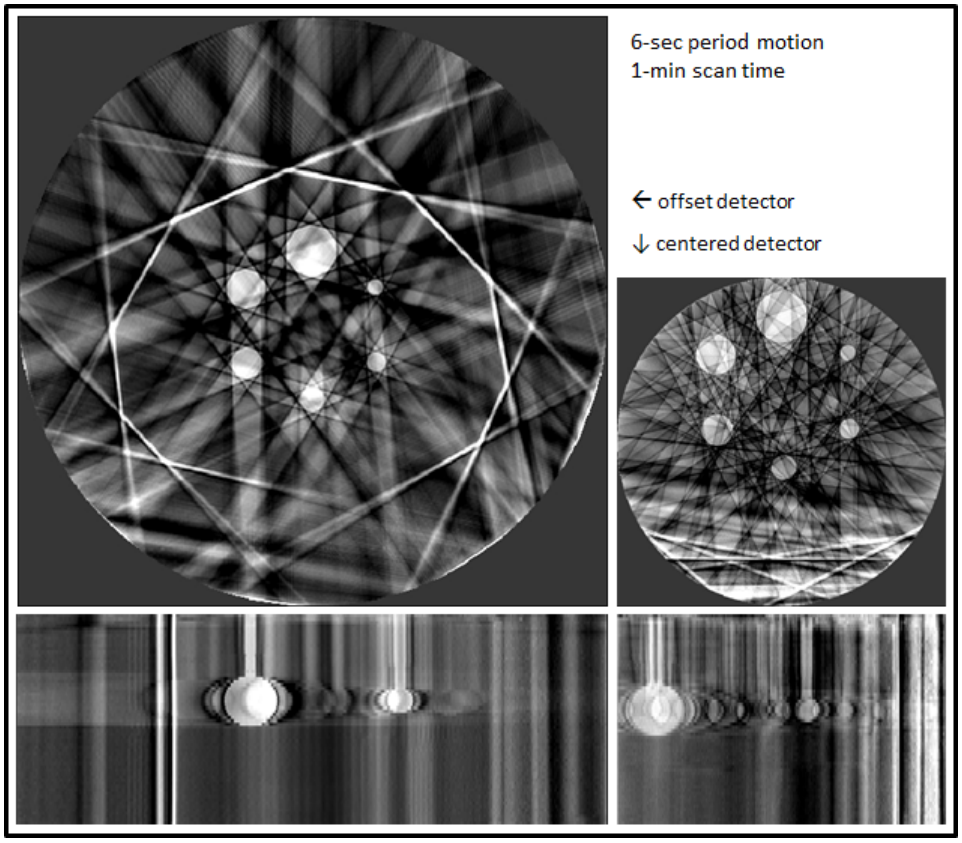

Figure 3.9: Centered and offset detector acquisitions for the 6-s motion period and 1-m scan time. Left column: offset detector, right column: centered detector, top row: axial views, bottom row: sagittal views. Used with permission from *Medical Physics* journal (Ahmad and Pan, 2012) [35].

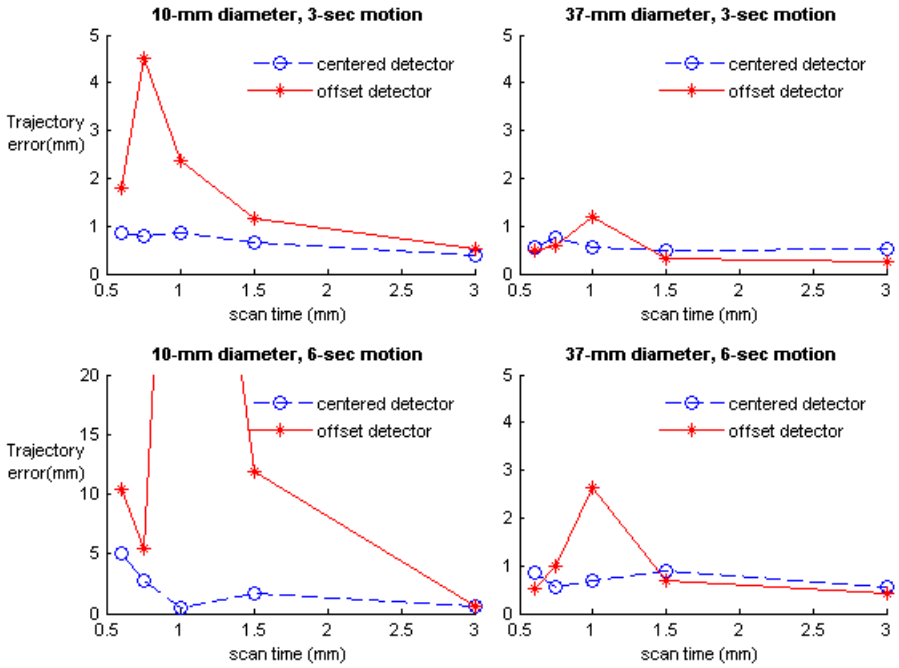

Figure 3.10: Comparison of root-mean-square trajectory errors for centered and offset detector configurations for 10-mm/37-mm sizes and 3-s/6-s periods. Errors are plotted against scan time. Used with permission from *Medical Physics* journal (Ahmad and Pan, 2012) [35].

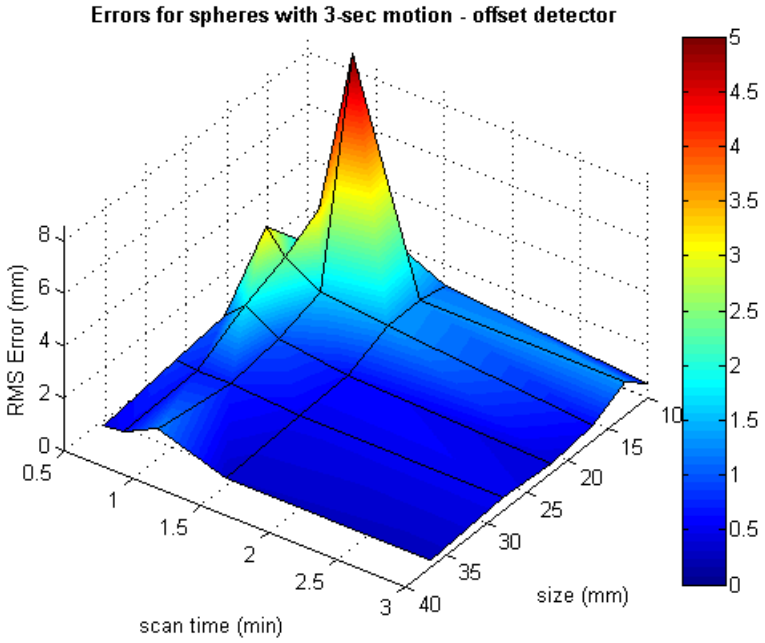

Figure 3.11: Root mean square (RMS) trajectory measurement errors of spheres of various sizes with 3-s motion using the offset detector acquisition. Used with permission from *Medical Physics* journal (Ahmad and Pan, 2012) [35].

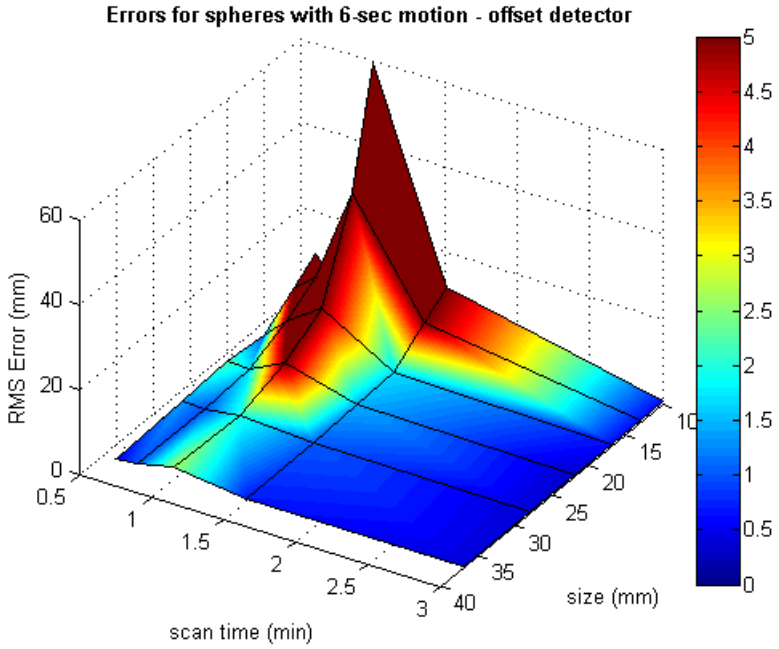

Figure 3.12: Root mean square (RMS) trajectory measurement errors of spheres of various sizes with 6-s motion using the offset detector acquisition. Used with permission from *Medical Physics* journal (Ahmad and Pan, 2012) [35].

3.2.1.3 Number of respiratory phases

Figure 3.13 shows images for the 1-m acquisition data of the phantom with 6-s motion period, corresponding to projection sorting using 2,4, and 8 phases. A clear loss of temporal resolution and motion blurring was evident in the 2-phase reconstruction (Figure 3.13, panel 3). Streak artifacts were present in all 3 sorting configurations. Even though the 2-phase reconstruction used more projection data due to the larger temporal width of the phase bin, the visual appearance of the streak artifacts did not improve much. Sacrificing temporal resolution did not appear to be a good strategy for mitigating streak artifacts.

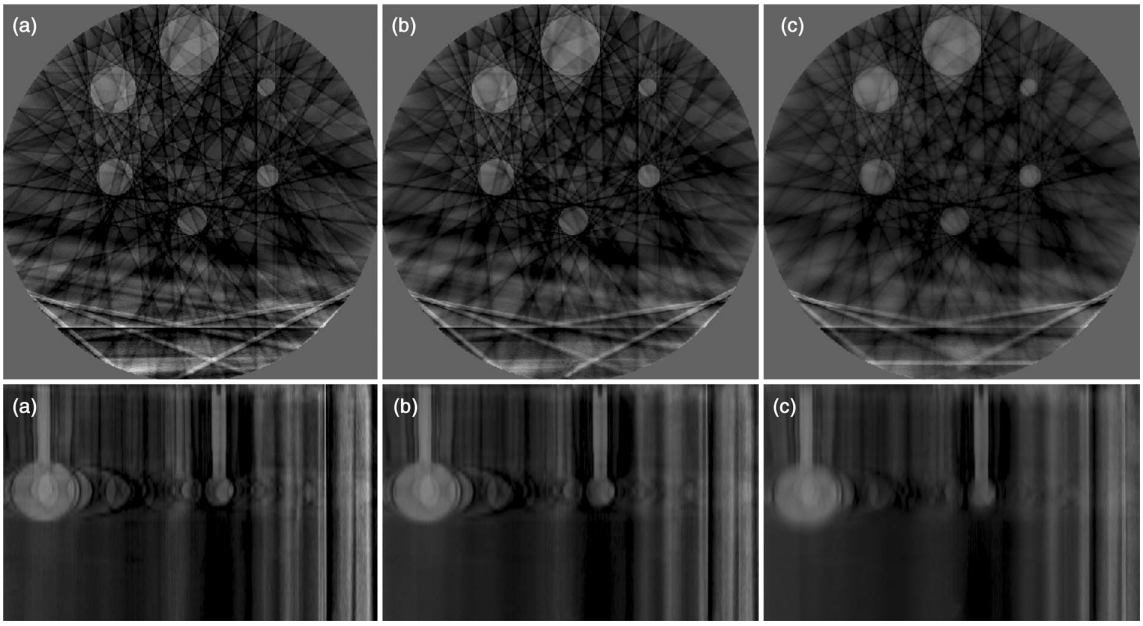

Figure 3.13: Reconstructions of the 6-s period NEMA motion phantom from 1-m acquisition data at 50% phase reconstructed using different numbers of respiratory phases: eight phases (a), 4 phases (b), and 2 phases (c). Top row: axial images. Bottom row: sagittal images. Used with permission from *Medical Physics* journal (Ahmad and Pan, 2012) [35].

Figure 3.14 shows the measured trajectories for spheres of various sizes and motions using a short scan time (30 s) and different number of phases. With 2 and 4 phases, the measured motion amplitude was systematically lower than the true value due to motion blurring. There was a systematic error of 6.5 mm when sorting the data into only 2 phase bins. The trajectories for 8 and 16 phases had only sub-millimeter differences. Eight phases provided sufficient temporal resolution for trajectory measurements. In general, although the streak artifacts were slightly reduced by reducing the number of phases, this did not improve the accuracy of the measured trajectory.

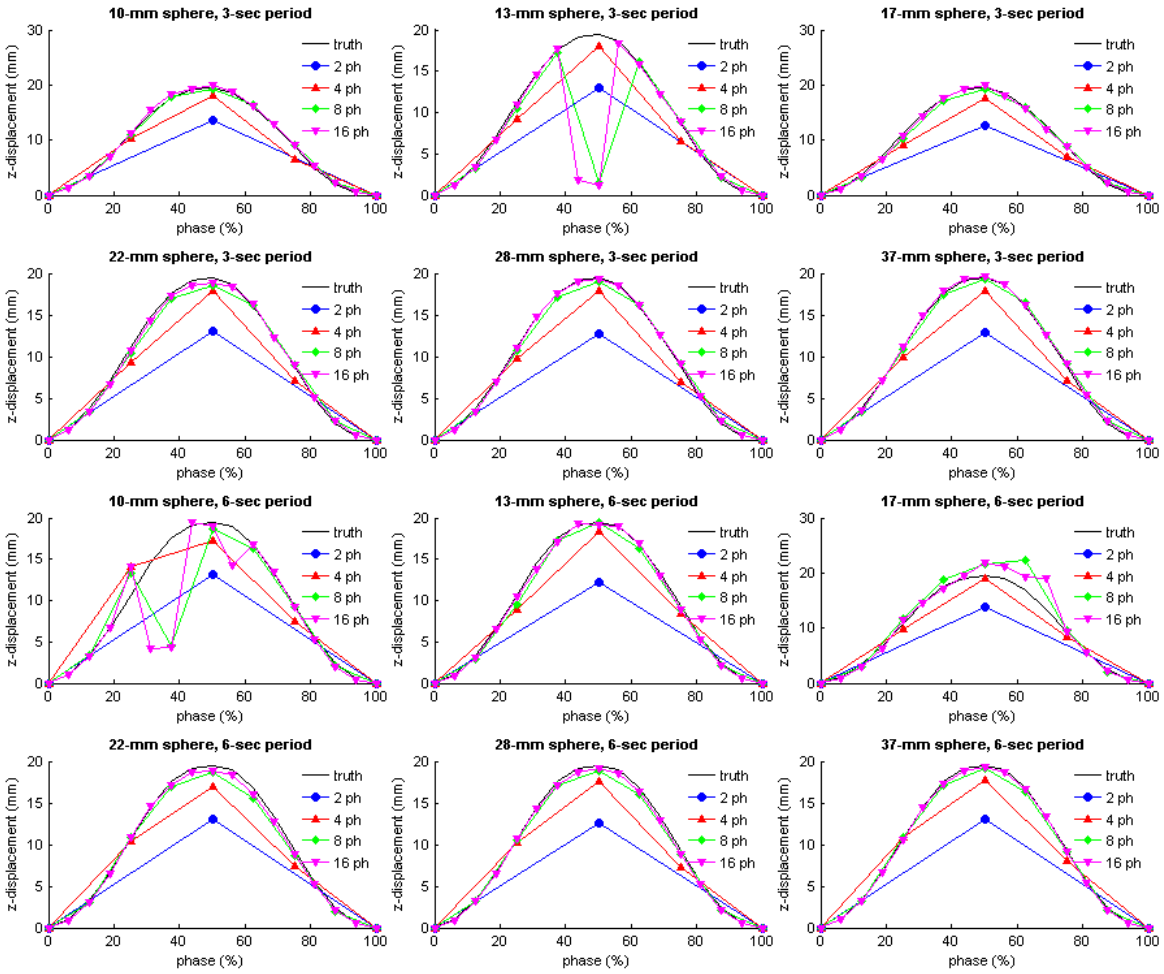

Figure 3.14: Measured trajectories of spheres of various sizes and motion periods using various numbers of phases to sort the projection data. Data for "short" scan time (30 s) are shown. Displacements along the longitudinal (z-axis) are plotted. Used with permission from *Medical Physics* journal (Ahmad and Pan, 2012) [35].

3.2.1.4 Smoothing filter in image reconstruction

Figure 3.15 shows the images reconstructed using different filters corresponding to zero, medium, and heavy smoothing. The top row shows filtered images for "highly sampled" 3-m scans. The bottom row shows filtered images for "undersampled" 36-s scans. The motion trajectories using different reconstruction filters for the under-

sampled acquisitions were measured. The RMS trajectory error results (in millimeters) are shown in Figure 3.16. The error for any given size was nearly the same regardless of the choice of filter in image reconstruction. The trajectories for the zero, medium, and heavy filters had mostly sub-millimeter differences among each other, even when the errors themselves were as large as 10 mm. In summary, the smoothing filter did not affect the measured trajectory, whether accurate or inaccurate.

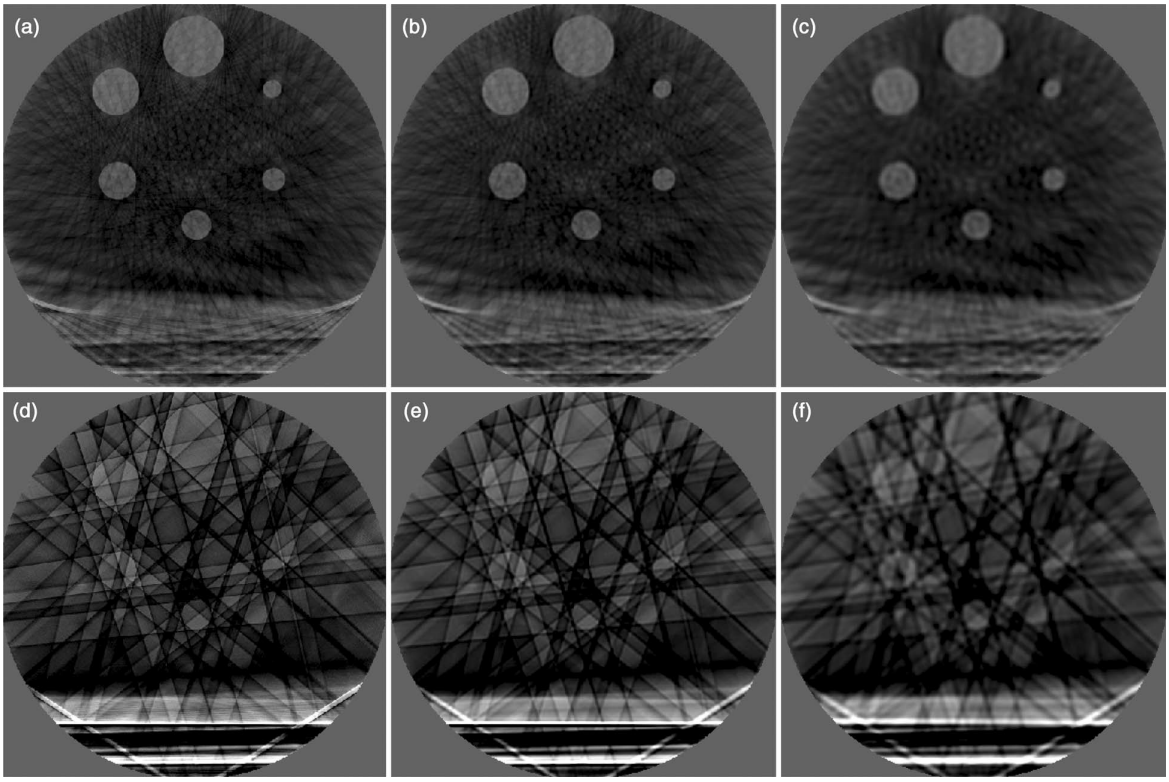

Figure 3.15: Reconstructions of the 6-s period NEMA motion phantom using different reconstruction filters at 50% phase. Top row: 3-m scan: (a) no smoothing, (b) medium smoothing, and (c) heavy smoothing. Bottom row: 36-s scan: (d) no smoothing, (e) medium smoothing, and (f) heavy smoothing. Used with permission from *Medical Physics* journal (Ahmad and Pan, 2012) [35].

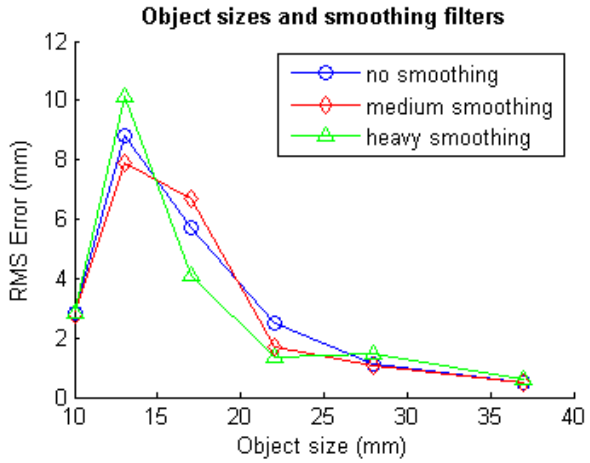

Figure 3.16: Root mean square (RMS) trajectory measurement errors of spheres of various sizes using various reconstruction filters. Data from 36-s scan time. Spheres have 6-s motion period. Used with permission from *Medical Physics* journal (Ahmad and Pan, 2012) [35].

3.2.2 Patient Study

Figure 3.17 shows the reconstructed image sets for the patient study for six different scan times, reconstructed using 8 phases. Using the deformable image registration method, we measured the trajectory of both the patient's lung tumor and the calcified plaque for several scan times and number of phases. Figure 3.18 shows the x, y, and z components of the trajectories for various scan times. The trajectories for the 4.5-m scan time were considered the truth. The errors in the measured tumor trajectories are shown in Figures 3.19 and 3.20. The tumor most closely resembled the 37-mm size / 3-s period sphere from the phantom study. However, the tumor had a 5-mm motion amplitude, whereas the phantom sphere had a 20-mm motion amplitude.

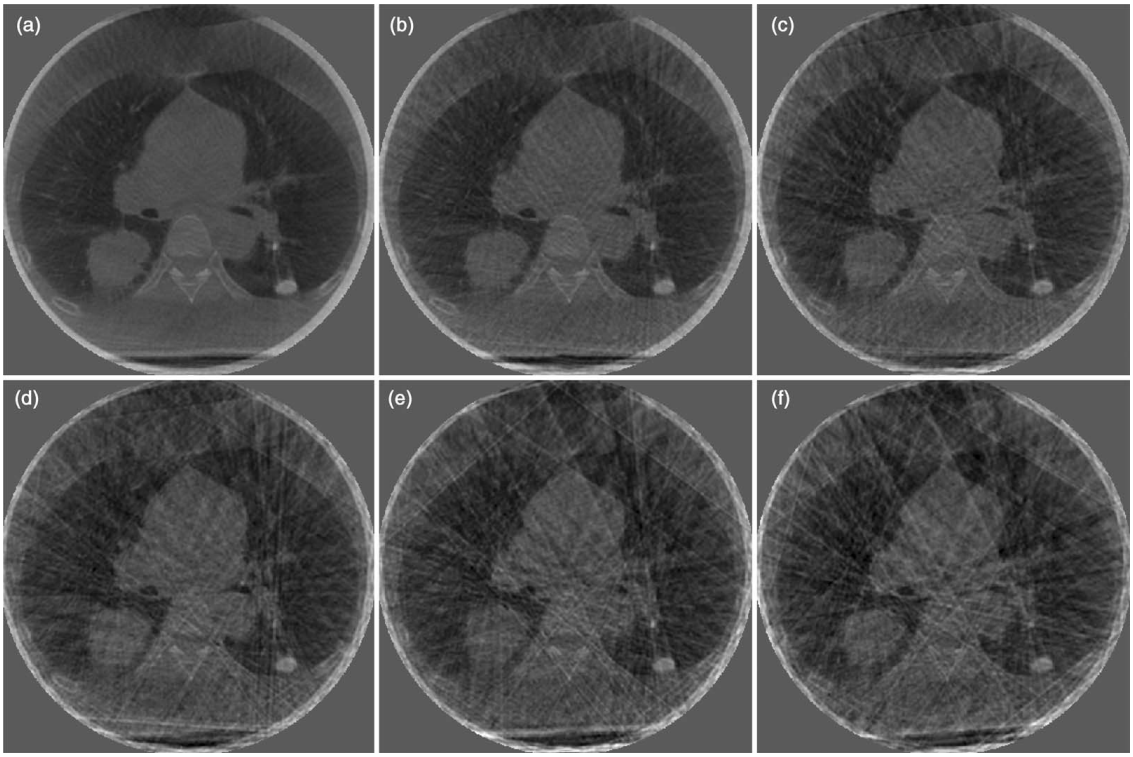

Figure 3.17: Reconstructions of the patient data corresponding to different scan times at 50% phase: (a) 3 m, (b) 1.5 m, (c) 1 m, (d) 45 s, (e) 36 s, and (f) 30 s. Used with permission from *Medical Physics* journal (Ahmad and Pan, 2012) [35].

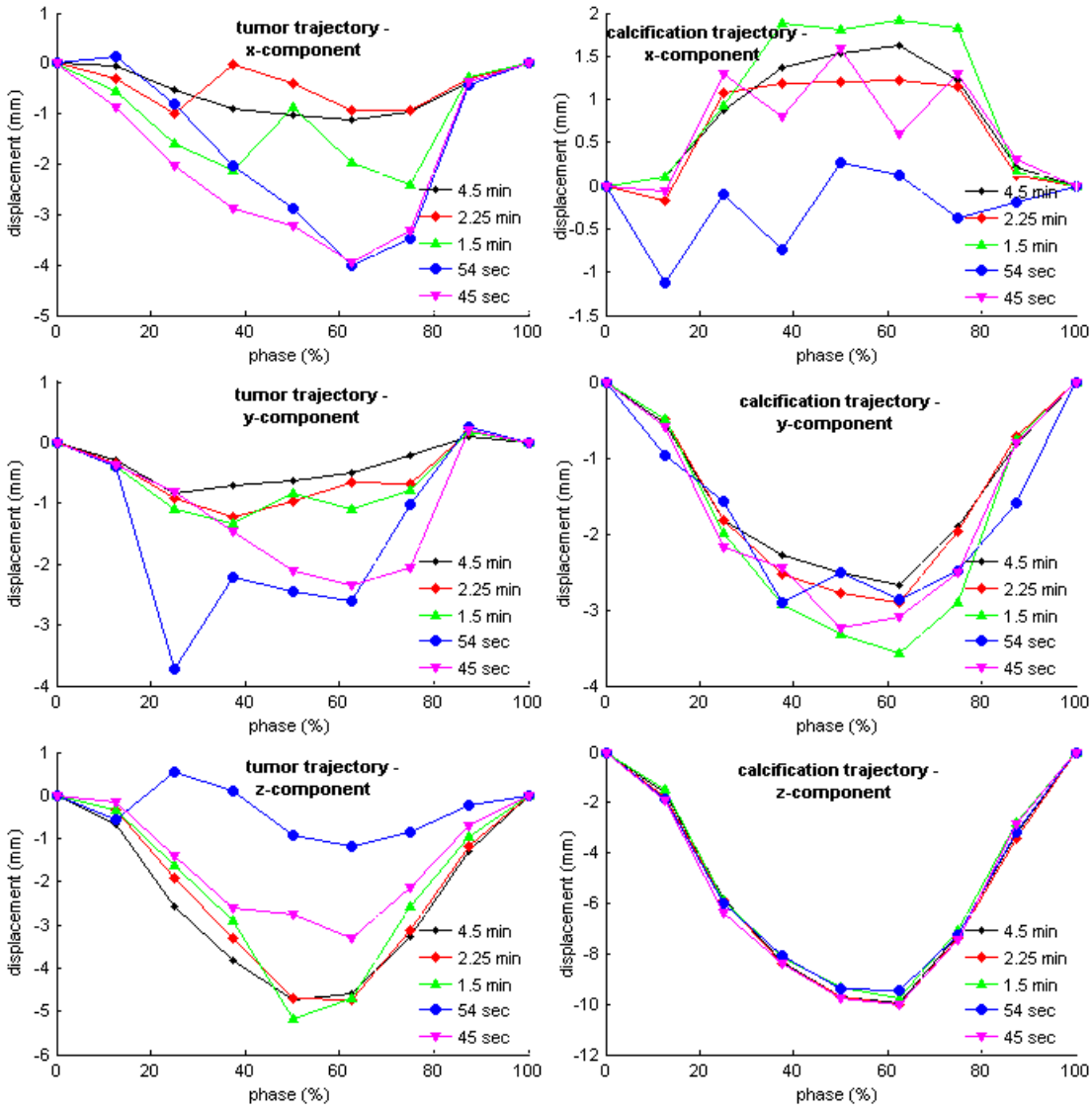

Figure 3.18: Measured trajectories of the lung tumor and calcification for various scan times. Data are based on reconstructions with eight phases. Used with permission from *Medical Physics* journal (Ahmad and Pan, 2012) [35].

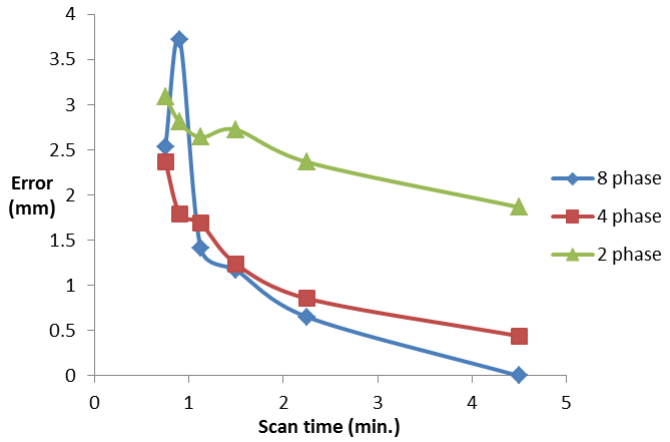

Figure 3.19: Root mean square (RMS) trajectory measurement errors of the lung tumor for different scan times and number of respiratory phases. Used with permission from *Medical Physics* journal (Ahmad *et al.*, 2012) [35].

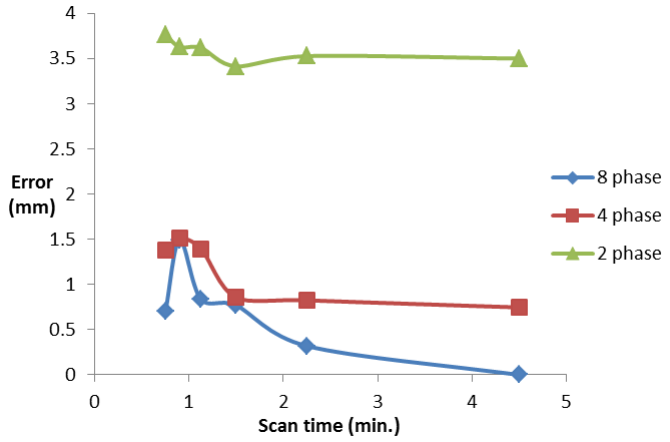

Figure 3.20: Root mean square (RMS) trajectory measurement errors of the calcified plaque for different scan times and number of respiratory phases. Used with permission from *Medical Physics* journal (Ahmad and Pan, 2012) [35].

The same trends in measurement errors were observed for the patient study as in the phantom study. The errors decreased with increasing scan time, and there was greater error using a smaller number of phases because of motion blurring. Whereas the errors for the 37-mm size / 3-s period phantom sphere changed slowly with scan time (approximately 0.5 mm for all scan times for 8- and 16-phase reconstructions),

there was more variation over scan times in the patient study. At short scan times, the errors were larger for the patient study. This suggests that the details of non-rigid motion are lost with decreasing scan time. There was one outlier at the 54-s scan time for the 8 phase bin sorting. For this particular scan, strong streak artifacts intersected the tumor, causing large errors in the measured trajectory. As discussed earlier, the streak pattern is largely unpredictable and strongly dependent on both the object and the angular sampling of projections. The calcification in this study most closely resembled the 10-mm size / 3-s period sphere from the phantom study.

The calcification had a 10-mm motion amplitude, whereas the phantom sphere had a 20-mm motion amplitude. The errors for both the calcification and phantom sphere were approximately 0.5 mm across all scan times (for 8-phase reconstructions). The mostly constant measurement accuracy across scan times for the calcification study may reflect the rigid nature of the calcified lesion. It may also be due to the high contrast of the calcification against the lung tissue background, making the task of tracking the motion equally easy across various scan times.

3.3 Discussion

This is the first investigation of how object size and motion affect 4D-CBCT performance, specifically the accuracy of trajectory measurements of objects influenced by respiratory motion. The results show that the most important parameter is the object motion period, with shorter periods being more favorable. The second important parameter is object size, with larger objects being more favorable. For the 3-s period of motion, objects larger than 13 mm were tracked with sub-millimeter accuracy with a 1-m scan time. For the 6-s period of motion, objects larger than 22 mm were tracked with sub-millimeter accuracy with a 1.5-m scan time. The object's period of motion and its size together should be used to select the appropriate scan

time.

Offset detector configuration did not degrade the 4D-CBCT performance compared to centered detector configuration except for slow-breathing objects smaller than 20 mm or scanned with acquisition time of 1 m or less. The number of phases or the reconstruction filters were not found to be important parameters for optimizing 4D-CBCT performance based on object size and motion alone.

Two factors that were not included in the scan time optimization study were object contrast and the degree of non-rigid motion. These factors may also have an important effect on 4D-CBCT motion measurement performance. More phantom studies testing these object parameters are needed to further optimize 4D-CBCT on a patient-specific basis. Lastly, although the results were confirmed in one patient study, more patient studies are needed to validate the results of the phantom study and to capture biological variation. Such a study would require knowledge of the true target trajectory obtained using an accurate reference imaging method such as 4D-CT or 4D-MRI, or using projection imaging with a fiducial marker. The reference imaging would be performed immediately prior to a 4D-CBCT. Such an experiment is not ethically possible in a clinical study, but may be possible in a small animal study.

Chapter 4

4D-VOI Reconstruction

This chapter presents a novel image reconstruction method for 4D-CBCT: the new 4D-VOI reconstruction. The purpose of this reconstruction method is to reconstruct images from undersampled data acquisitions of about 1-min scan time. This reconstruction achieves better image quality than standard FBP reconstruction, while keeping computational cost much lower than that of iterative reconstruction algorithms. The computational cost is small enough that a practical computational implementation is feasible for IGRT. The improved image quality, short scan time, and practical computational cost are important improvements in 4D-CBCT for IGRT. The Methods, Results, figures and tables in this chapter were reprinted from Ahmad *et al.* [50] with permission from the Medical Physics journal.

4.1 Methods

4.1.1 Algorithm specification

In the 4D-VOI reconstruction, first a motion averaged 3D reconstruction is performed using all (i.e., unsorted) projection data. The 3D reconstruction is performed using

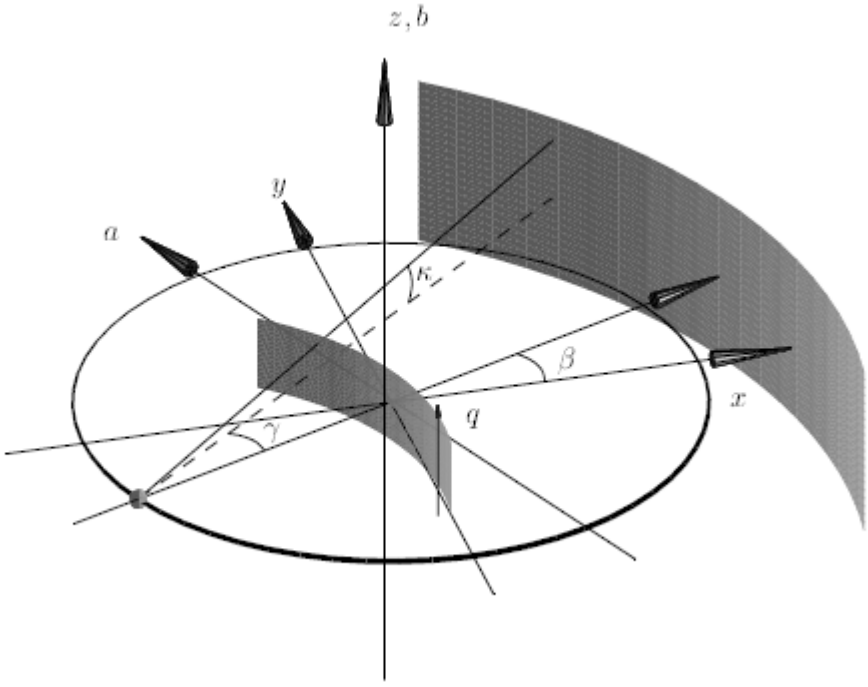

Figure 4.1: The cone-beam geometry. The axes of the planar detector (a, b) and the projection angle β are shown. Taken from Turbell [51].

the Feldkamp filtered back-projection (FBP) reconstruction, which is given by the following discrete formula:

$$f_{3D}(x, y, z) = \frac{2\pi}{M} \sum_{i=1}^{M} \frac{Q(\beta, a, b)}{U(x, y, z)} \ , \tag{4.1}$$

where M is the total number of cone-beam projections, $Q(\beta, a, b)$ is the filtered raw cone-beam projection data, and U is a weighting factor in back-projection. The Cartesian coordinates (x, y, z) represent the reconstruction volume, and the coordinates (β, a, b) represent the raw data (sinogram) space. The coordinate β is the projection angle, and (a, b) are the horizontal and vertical directions on a two-dimensional detector, respectively. The cone-beam geometry is depicted in Figure 4.1. Each of these factors is explained in greater detail by Feldkamp *et al.* [39] The back-projection is performed with the summation.

In the conventional 4D-CBCT (full 4D) reconstruction, the projections $[1, M]$ are sorted into phase bins $B_1, B_2, \ldots, B_N$, where N is the number of respiratory phases to be reconstructed. The full 4D reconstruction is given by

$$f_{full4D}(x, y, z) = \frac{2\pi}{n(B_k)} \sum_{i=1}^{i \in B_k} \frac{Q(\beta, a, b)}{U(x, y, z)} \ , \tag{4.2}$$

where $k \in 1, N$ is the respiration phase to be reconstructed, and $n(B_k)$ is the number of projections in the kth respiration phase. The major difference between the full 4D and the 3D reconstructions is that the summation runs over a more limited set of projections in the full 4D case. In the 4D-VOI reconstruction, a 3D volume-of-interest (VOI) containing the radiotherapy target and any respiratory motion is first selected. The VOI is defined on the motion-averaged image (which does not have undersampling artifacts.) This VOI may be a user-drawn contour or a generic shape such as a cube, cylinder, or sphere. The 4D-VOI reconstruction is defined as a composite of the 3D and full 4D reconstructions,

$$f_{4D-VOI}(x, y, z) = \begin{cases} f_{full4D} & \text{for}(x, y, z) \in VOI, \\ f_{3D} & \text{otherwise} \end{cases} \tag{4.3}$$

In other words, the region inside the VOI is set equal to the full 4D reconstruction, and the area outside of the VOI is set equal to the 3D reconstruction. The purpose of this composite reconstruction is to eliminate the streak artifacts outside the VOI, where temporal resolution is not needed. The temporal resolution is maintained within the VOI, which contains the target motion information.

In patient studies, an appropriate VOI for this reconstruction method is not necessarily known. For these patient studies, the planning target volume (PTV) from radiation therapy planning was used as the choice of VOI in the 4D-VOI reconstruc-

tion. The PTV is a volume based on a contour drawn by a physician on a treatment planning image (typically CT). The PTV delineates the radiation therapy target and also contains safety margins to account for many sources of uncertainty in target position and size caused by respiratory motion, setup errors, unseen microscopic, and diseased tissue [12]. The PTV is *a priori* information based on a physician's interpretation of CT images, and it includes margins for target position uncertainty. It is a reliable choice of VOI for this reconstruction as it is specifically designed to contain the target. The work flow for the 4D-VOI reconstruction was as follows: First, the unsorted raw CBCT was used to reconstruct the motion-averaged (3D-CBCT) image. Next, the PTV from the treatment plan was registered to the 3D-CBCT image. The PTV was manually registered to the 3D-CBCT image using a rigid body translation. Once the PTV was registered, the final step was the 4D reconstruction of the voxels inside the PTV according to Equation 4.3. The projection data were sorted using the respiration signal. The sorted projection data were used for 4D reconstruction in only the VOI region.

4.1.2 Mathematical phantom study

A mathematical (synthetic) phantom was used to test the VOI-based reconstruction. This reconstruction is designed for cone-beam CT but is also applicable to any projection imaging system where large gaps in angular sampling may occur. For simplicity, a simulation using a two-dimensional phantom with motion was performed, based on the commonly used Shepp-Logan phantom. The phantom is composed of ellipses, whose parameters are listed in Ref. [52]. The three small (high-contrast detectability) ellipses were replaced with a moving circular disk as shown in Fig 4.2. The disk has a continuous sinusoidal motion with a 4-s period, and the motion amplitude is equal to the diameter of the disk. The ellipse parameters defining the moving disk

are provided in Table 4.1.

The scan consisted of analytic line integral calculation of rays intersecting the ellipses in the mathematical phantom. The scan time was 1-min and 600 projection angles were acquired. For each of these 600 projection angles, a set of projections onto a flat one-dimensional detector was calculated. This 2D object simulation used the same geometry as the central plane of the Varian On-Board Imager (OBI) CBCT system (Varian Medical Systems, Palo Alto, CA.) The projection data were sorted into eight phases. After sorting, there were 75 projection angles for each phase. This combination of motion period, scan time, scan rotation speed, and projection sorting resulted in a distribution of projection angles that is representative of 1-min 4D-CBCT.

The mathematical phantom is useful because it contains high intensity structures that generate streak artifacts when there is angular undersampling. An ROI (as opposed to "VOI" for this two-dimensional phantom) was chosen to encapsulate the target motion (see Figure 4.3) and was used in the ROI-based reconstruction.

Figure 4.2: Left- Shepp-Logan phantom. Center- Modified motion phantom at 0% phase. Right- Phantom at 50% phase. The three detail spheres near the bottom have been replaced with a circular disk that moves in the vertical direction. Used with permission from *Medical Physics* journal (Ahmad *et al.*, 2011) [50].

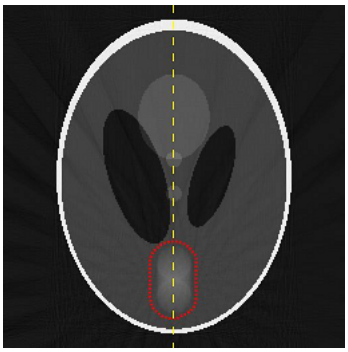

Figure 4.3: Motion averaged reconstruction using all projection data. The dashed vertical line is used to measure the intensity line profile. The dotted line indicates the ROI used in the dynamic ROI reconstruction. Used with permission from *Medical Physics* journal (Ahmad *et al.*, 2011) [50].

Table 4.1: Parameters defining the moving disk in the Shepp-Logan phantom.

Center coordinate $(x(t), y(t))$	$(0.1 * \sin(2\pi t/4\text{s}), 0)$
Major axis length (x-direction)	0.1
Minor axis length (y-direction)	0.1
Intensity	0.25

Table 4.2: Simulation scan parameters

Phantom size	$256 * 256$
Number of detectors	512
Fan angle	$15.09°$
Scan range	$0° - 195.09°$
Number of projection angles	660
Scan time	60 s
Number of phase bins	8

4.1.3 Dynamic chest phantom study

A dynamic chest phantom was set up to simulate a lung tumor undergoing respiratory motion. An anthropomorphic chest phantom was used so that the realistic streak artifacts would be generated in undersampled acquisitions. The chest cavity of the phantom was emptied, and a 2-cm diameter water-filled sphere was placed in the emptied volume of the left lung. This sphere was suspended in the lung by a movable plastic rod that was driven by a motor to simulate the periodic respiratory motion. The water-filled sphere was programmed to move in the superior-inferior direction with a 1.8-cm amplitude and a 4.2-s period. The phantom was scanned with the Varian On-Board Imager (OBI) CBCT scanner (Varian Medical Systems, Palo Alto, CA) in its clinical low-dose thorax mode. This mode completes one gantry rotation in 60 s and acquires 660 projections over a 360-deg rotation. The known motion profile was used to sort out the projections into eight respiratory phase bins.

4.1.4 Patient studies

Retrospective 4D-CBCT patient studies were performed using data from lung cancer patients who had received stereotactic body radiation therapy. The raw CBCT data and the respiratory tracking data were taken from two patient studies. The respiration tracking method used the Varian Real-time Position Management (RPM) System to track the height of the chest wall of a free-breathing patient lying in the supine position [44]. The two patients previously had long acquisition (4.5-6 min) 4D-CBCT scans. Since the purpose of this present study was to demonstrate 4D-CBCT with short acquisitions of about 1 min, the number of projections in the long acquisitions was reduced to simulate shorter acquisitions. The projections were removed in a way that represented an accurate number of breath cycles for a 1-min scan time. For instance, to reduce the scan time by 80%, the projection data for only one of

five breath cycles were retained, while data for the other four breath cycles were discarded. This process produced an angular distribution of projection angles that was a realistic representation of a 1-min scan. After reducing the datasets to 1-min, patient studies 1 and 2 had 403 and 406 projections respectively.

4.1.5 Image quality comparison of 4D-VOI and reference reconstruction algorithms

The 4D-VOI, standard 4D, and McKinnon-Bates (MB) [53, 31] algorithms were tested and compared using the same acquisition data. The MB reconstruction is a two-pass reconstruction that reconstructs a static image in the first pass and adds the dynamic details in the second pass. For both phantom and patient studies, the 4D-VOI reconstruction was compared with the standard phase-sorted Feldkamp reconstruction in terms of image quality. Because the entire volume in the standard phase-correlated Feldkamp reconstruction was 4D (whereas the 4D-VOI reconstruction had only a small 4D volume), the former is referred to as the "full 4D" reconstruction. In particular the streak artifacts that resulted from undersampling were assessed. The 4D-VOI reconstruction was also compared with the MB reconstruction algorithm in terms of streak artifacts and image contrast. Last, the standard 3D reconstruction was also included as a reference point for assessing the temporal resolution gained in the 4D methods.

To highlight and assess the streak artifacts in the different reconstructions, each image was also processed with a Sobel 3*3 pixel edge-detection kernel. The edge-detection filter brings out straight edges (streak artifacts) and also the inherent edges of the object.

The motion resolution in the phantom study was measured using the known true motion. The motion blur was quantitatively assessed by measuring the apparent

width of the sphere. The image intensity along a line profile through the moving sphere was measured at both the end-inhale and the end-exhale phases. The motion blurring was then quantitatively assessed by measuring the apparent width of the sphere. The sphere size was measured as the full-width half-maximum (FWHM) of the peak seen in the line profile. The motion displacement is measured as the displacement of the peak (as determined by FWHM) between the end-exhale and the end-inhale phases.

Last, the contrast-to-noise ratio (CNR) was measured for the different reconstructions. In the patient studies, the mean image intensity values in a homogeneous region in the heart and in a region in the background lung were measured. This was divided by the noise (standard deviation) of the region of interest in the heart. In the phantom study, a similar measurement was used, except that the water region was used instead of the heart region and the air region was used instead of the lung background.

4.2 Results

4.2.1 Mathematical phantom

The mathematical phantom is a two-dimensional moving object. To avoid confusion with the terms "2D", "3D," and "4D", the following names were adopted for the reconstructions in this mathematical phantom study: "Dynamic ROI reconstruction" refers to the reconstruction in which motion is resolved in a small region only. It is analogous to the 4D-VOI reconstruction in CBCT. "Full dynamic" refers to the reconstruction in which motion is resolved throughout the imaging volume. It is analogous to full 4D reconstruction in CBCT. "Motion averaged" refers to the reconstruction using the complete, unsorted projection data set. It is analogous to 3D reconstruction

Table 4.3: Names adopted for the reconstructions in the mathematical phantom study

Mathematical phantom study	Analogous CBCT reconstruction
Dynamic ROI	4D-VOI
Full dynamic	Full 4D
Motion averaged	3D-CBCT

in CBCT. The names are summarized in Table 4.3

The reconstructed images for dynamic ROI, full dynamic, and motion averaged reconstructions are shown in Figure 4.4. Undersampling produces severe streak artifacts in the full dynamic reconstruction. The ROI selected for the dynamic ROI reconstruction is shown by the dotted line in Figure 4.3. Although there is no improvement inside the ROI in the dynamic ROI reconstruction, the region outside the ROI is much improved due to the reduction of streak artifacts. The two low-contrast circles in the center of the phantom are far clearer in the dynamic ROI reconstruction. The motion-averaged image reconstruction using all the projections (shown in Figure 4.3) lacks temporal resolution and shows a motion blur for the moving disk.

The quantitative accuracy of the dynamic ROI reconstruction was assessed using the line profile depicted by the dashed yellow line in Figure 4.3. The measured line profiles are shown in Figures 4.5 to 4.8. Figure 4.5 compares the dynamic ROI (dashed line) and full dynamic (dotted line) reconstructions at the 0% phase. The ground truth is shown in the solid red line. Outside the ROI region, the line profile for the full dynamic reconstruction shows large errors (root mean square error of about 0.25), whereas the line profile for the dynamic ROI reconstruction is essentially equivalent to the ground truth. Inside the ROI region, the line profiles for the dynamic ROI and full dynamic reconstructions are equivalent (by definition). Figures 4.6 and 4.7 show similar plots for the 25% and 50% phases. Figure 4.8 compares the dynamic ROI reconstruction (0% and 50% phases) to the motion averaged reconstruction.

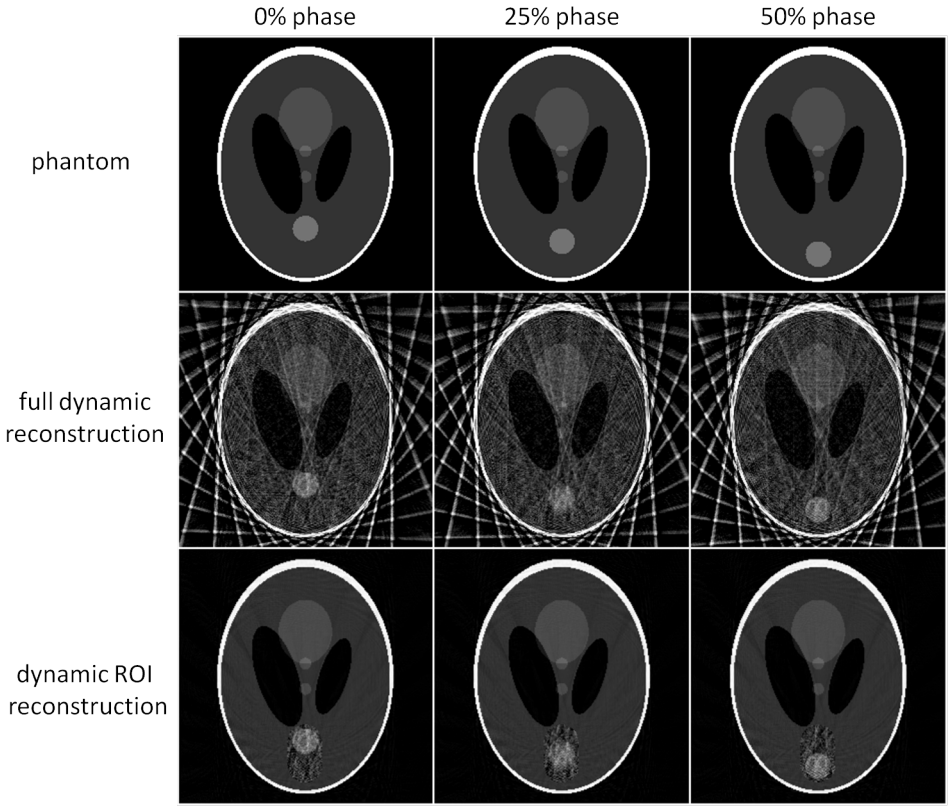

Figure 4.4: Dynamic ROI reconstruction compared against the full dynamic reconstruction and the truth image. Used with permission from *Medical Physics* journal (Ahmad *et al.*, 2011) [50].

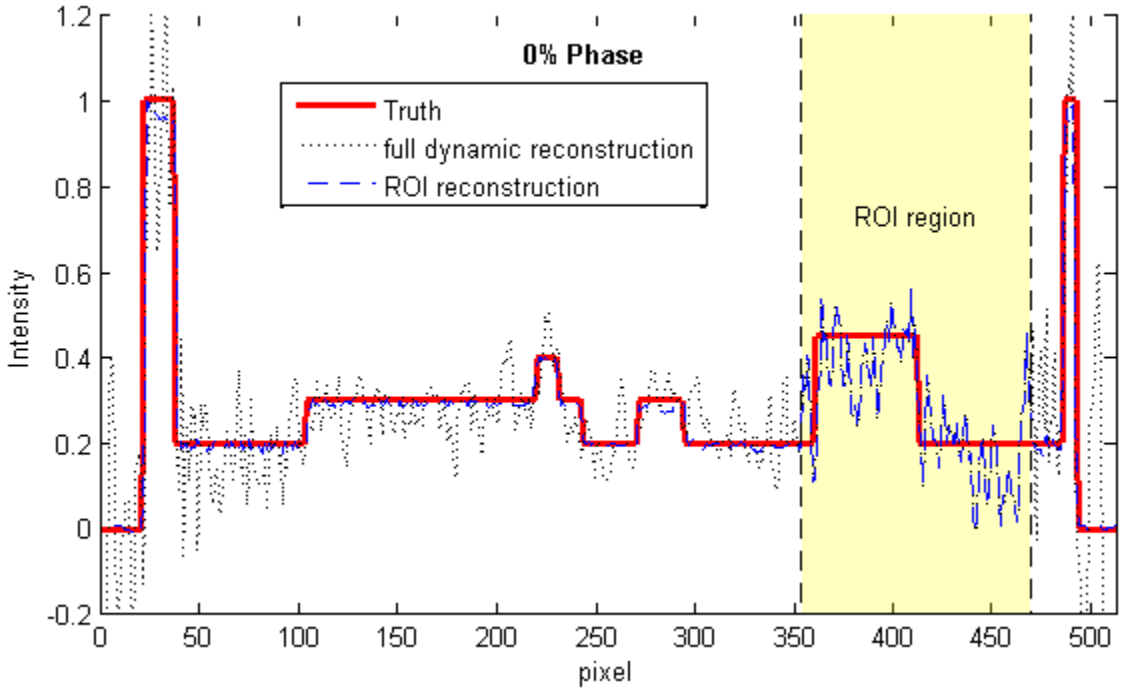

Figure 4.5: Line profiles of the reconstructions at the 0% motion phase. Used with permission from *Medical Physics* journal (Ahmad *et al.*, 2011) [50].

The dynamic ROI reconstruction shows motion-resolved line profiles, whereas the motion-averaged reconstruction shows a static triangular profile.

The RMS pixel errors were measured in the entire image and in the ROI region. The RMS errors of the various reconstructions are shown in Figure 4.9. The RMS pixel statistics were calculated over (1) the entire image, and (2) only the ROI region. The full dynamic reconstruction has a large RMS error (0.25) over the whole image due to streak artifacts. Because of motion blur, the motion averaged reconstruction has slightly greater error inside the ROI (0.107) than the dynamic ROI and fully dynamic reconstructions (0.099 and 0.99 errors, respectively). The high contrast of the disk helps the dynamic ROI reconstruction to resolve the shape and the location of the disk, despite the presence of streak artifacts inside the ROI region. This result suggests that this reconstruction method may be advantageous for lung lesions, which

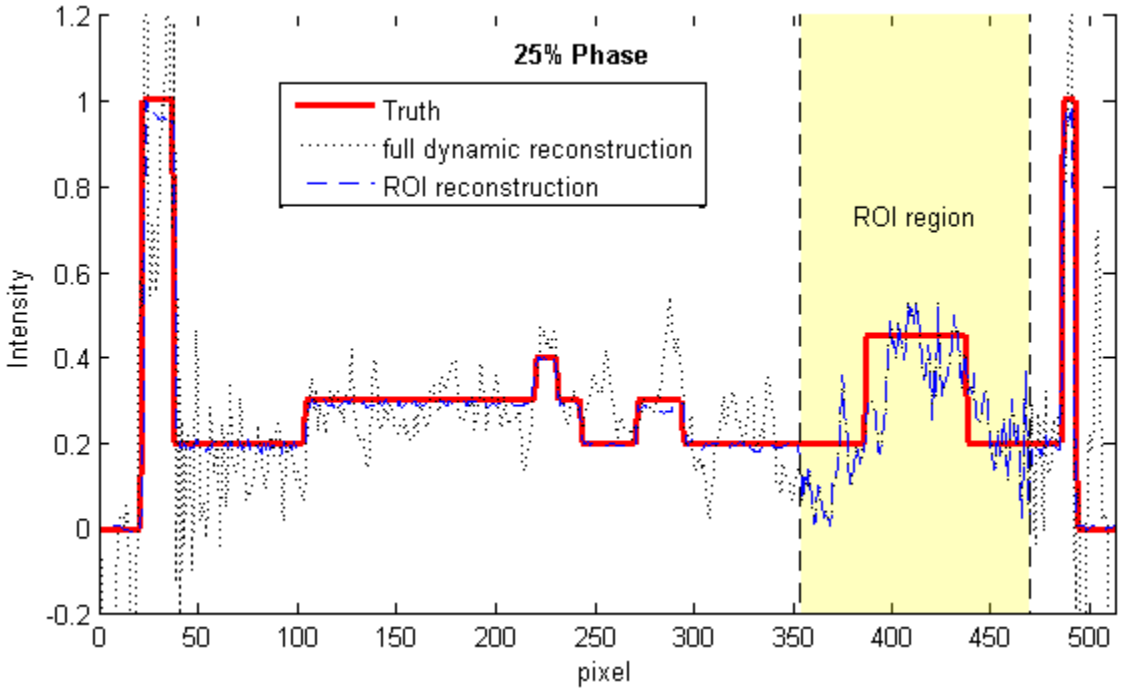

Figure 4.6: Line profiles of the reconstructions at the 25% motion phase. Used with permission from *Medical Physics* journal (Ahmad *et al.*, 2011) [50].

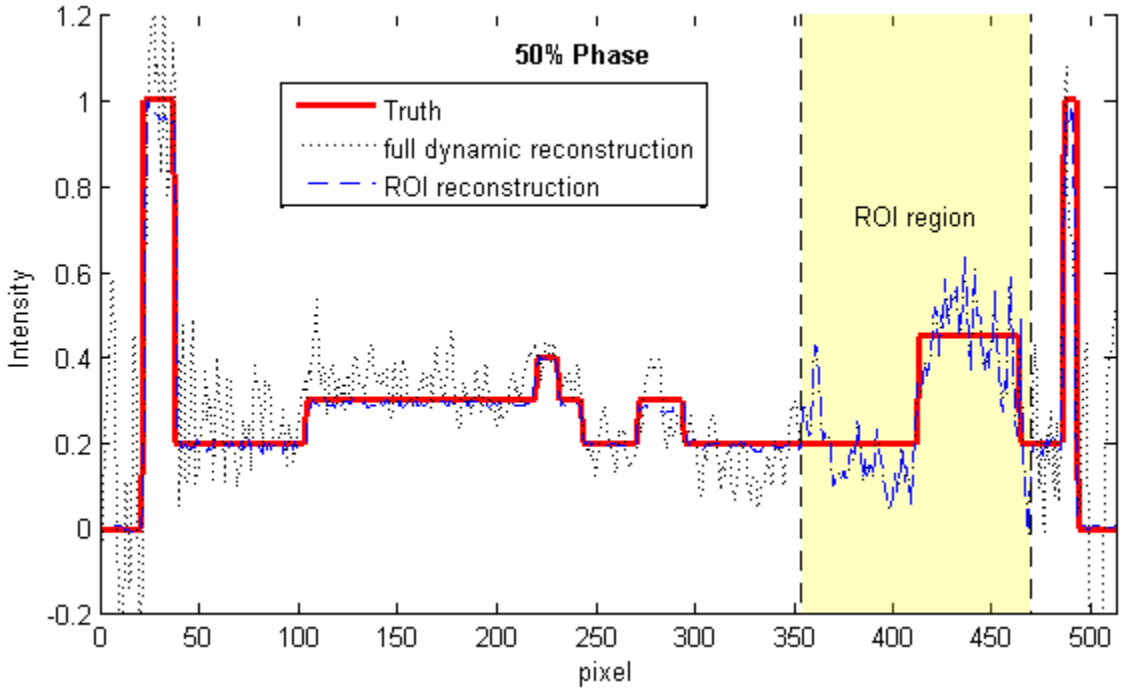

Figure 4.7: Line profiles of the reconstructions at the 50% motion phase. Used with permission from *Medical Physics* journal (Ahmad *et al.*, 2011) [50].

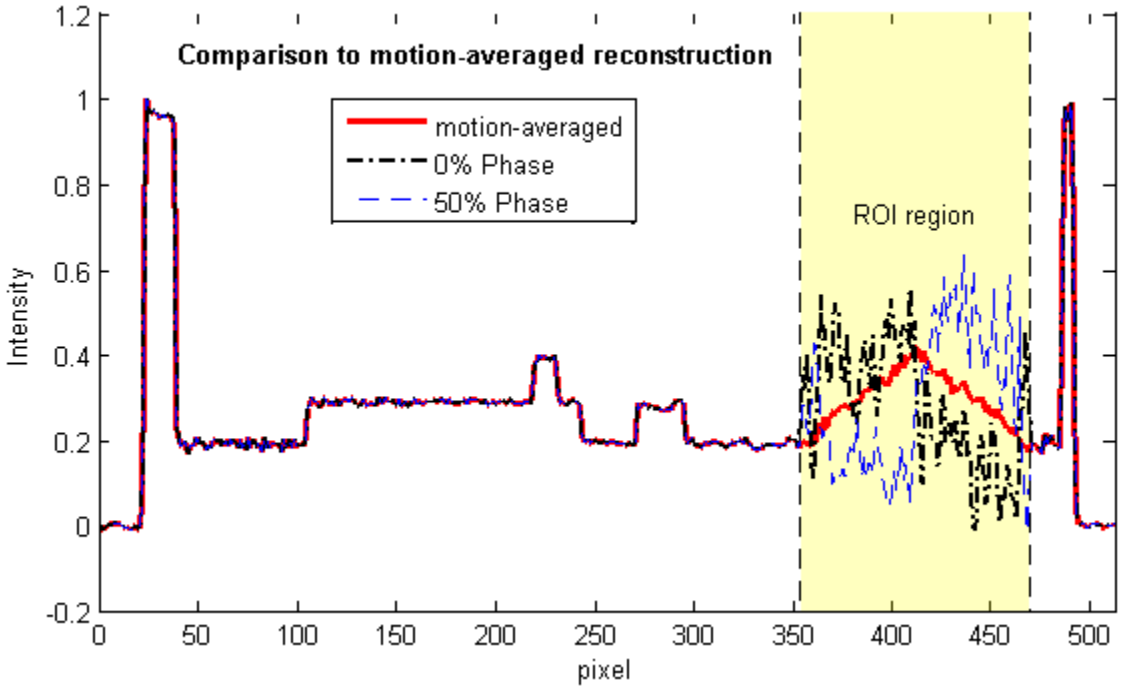

Figure 4.8: Comparison of the dynamic ROI reconstruction to the motion averaged reconstruction. Used with permission from *Medical Physics* journal (Ahmad *et al.*, 2011) [50].

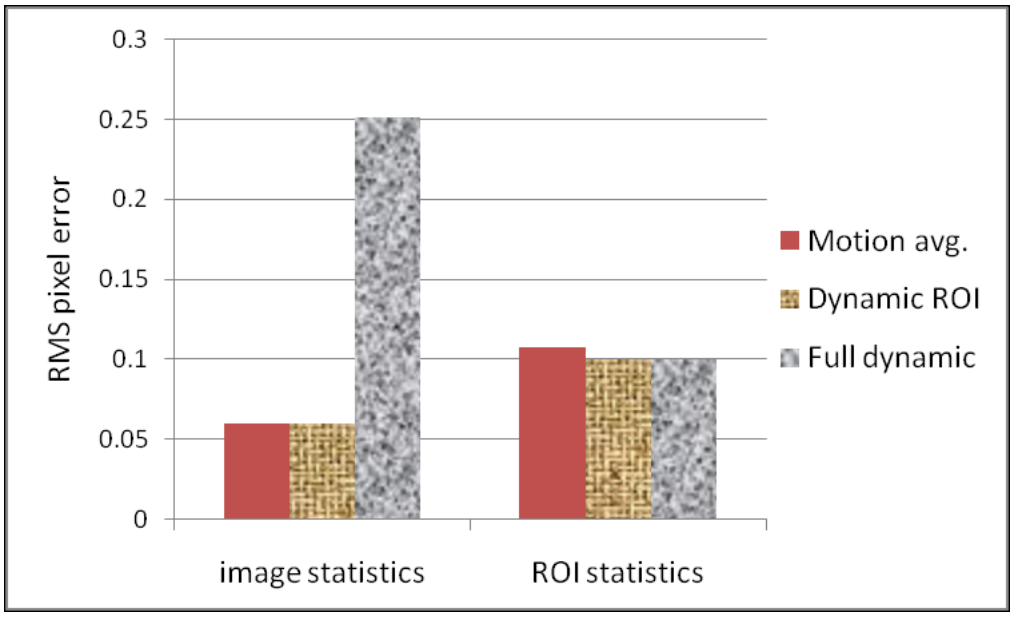

Figure 4.9: RMS pixel error values for the motion averaged, dynamic ROI, and full dynamic reconstructions. The dynamic ROI and full dynamic reconstructions were reconstructed at the 0% motion phase. Used with permission from *Medical Physics* journal (Ahmad *et al.*, 2011) [50].

typically have good contrast against the low density lung tissue background.

4.2.2 Dynamic chest phantom

The 4D-VOI, full 4D, and MB reconstructions in the dynamic chest phantom experiment are compared. The reconstructed images are shown in Figures 4.10 and 4.11. For the coronal views in Figure 4.10, the two extreme phases (end-exhale and end-inhale) are shown. In the 4D-VOI reconstruction, the VOI is a tight cylinder enclosing the moving sphere. The 4D-VOI reconstruction shows a clear motion of 2 cm, as measured by a simple distance-measuring tool on an image viewer. The full 4D reconstruction also shows the same motion since, by definition, it has the same values inside the VOI as the 4D-VOI.

The major difference between the 4D-VOI and the full 4D reconstructions is seen in the region outside the VOI where the full 4D images are distorted by streak artifacts.

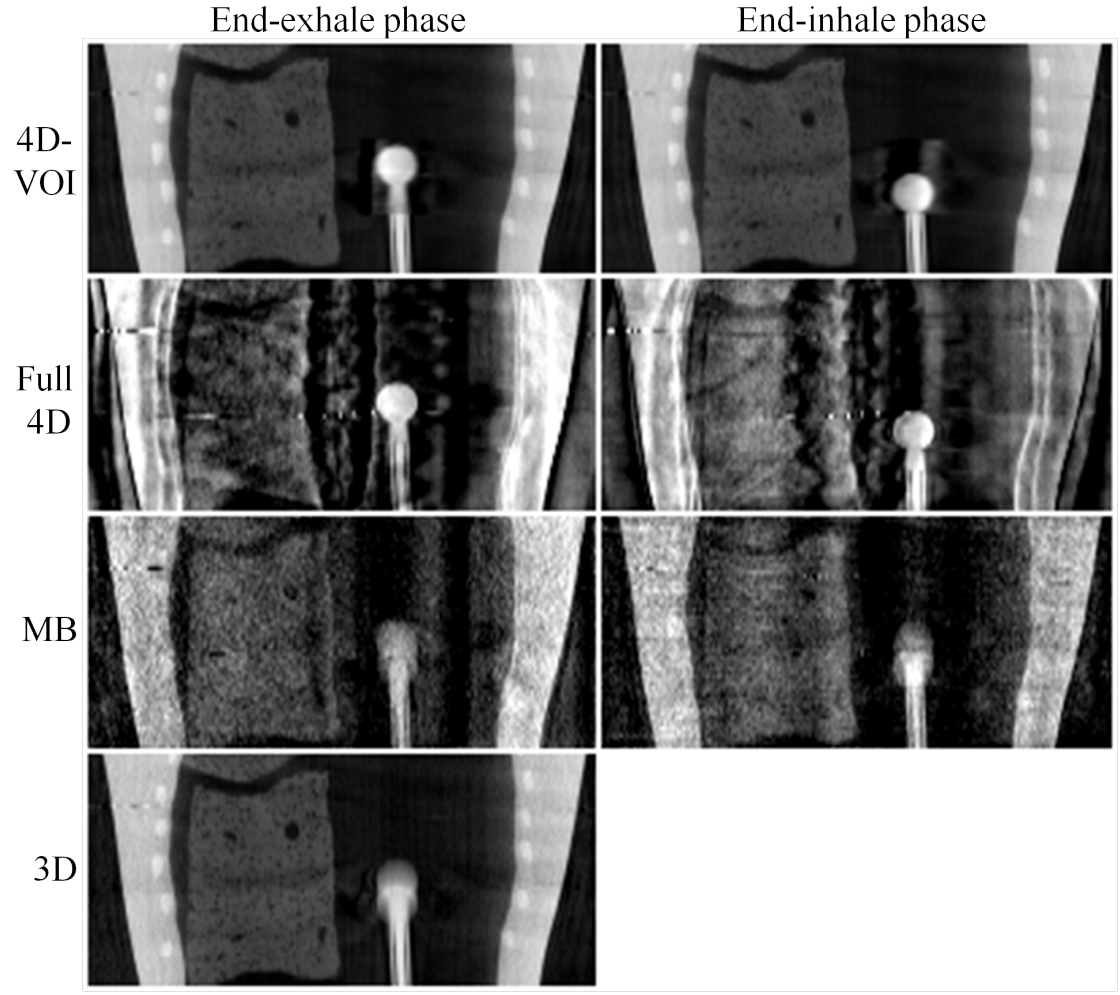

Figure 4.10: Chest phantom study: a 2-cm-diameter sphere moving inside an empty chest cavity phantom with 1.8-cm motion amplitude. Coronal views at end-inhale and end-exhale phases for the 4D-VOI, full 4D, MB, and static (3D) reconstructions. Window/level: 600/-20. Used with permission from *Medical Physics* journal (Ahmad *et al.*, 2011) [50].

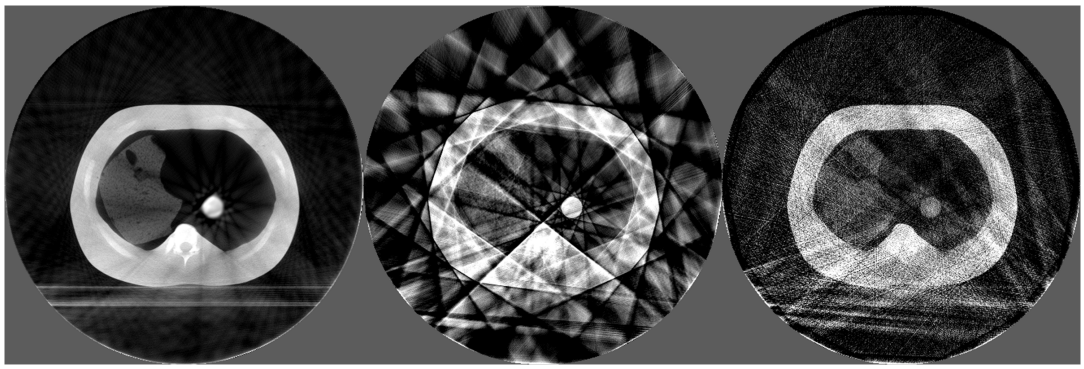

Figure 4.11: Chest phantom study: Axial views of the end-exhale phase. W/L: 600/-20. Used with permission from *Medical Physics* journal (Ahmad *et al.*, 2011) [50].

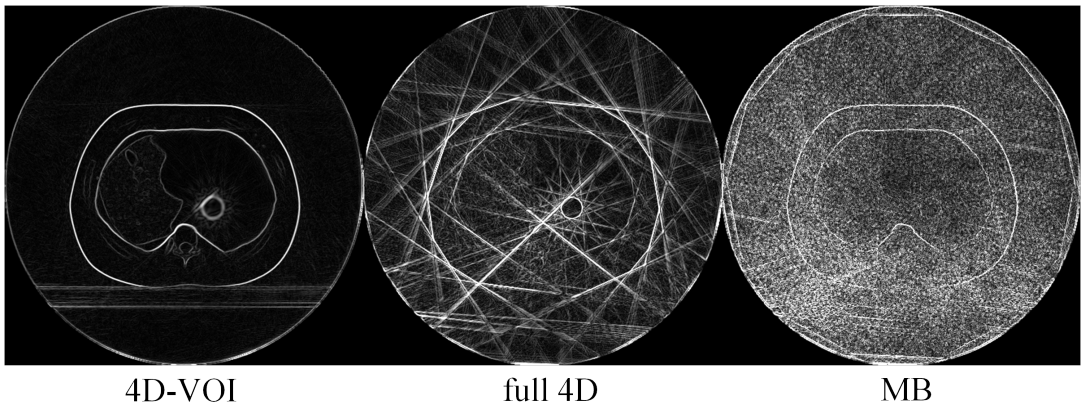

Figure 4.12: Phantom study: edge-detection filter processing on the 4D-VOI, full 4D, and MB reconstructions. Used with permission from *Medical Physics* journal (Ahmad *et al.*, 2011) [50].

In the left side of the coronal images, the right lung material is visible. In the 4D-VOI reconstruction, the fine details of the porous lung material are visible compared with the full 4D reconstruction, which shows heavy streak artifacts. In the coronal view, the streak artifacts appear as alternating bright and dark vertical bands, and the lung material is highly distorted. The location of the chest wall interface is also ambiguous in the full 4D reconstruction. The rib cage is also prominently distorted as streaks radiate from these bones. The axial view in Figure 4.11 shows the streak artifacts radiating from bony anatomy. The table on which the phantom rested is completely missing because of missing view angles of parallel rays through the table.

The MB reconstruction shows markedly fewer streak artifacts than the full 4D images. The location of the chest wall is clear, and some more details (such as air pockets in the lung material) are visible. The contrast was lost between the rib tissue and the soft tissue, so the position of the ribs is unclear. Unlike in the full 4D image, the table is visible, but it is distorted by streak artifacts. The MB reconstruction also shows poor temporal resolution, and motion blur is evident. Motion blur is discussed further in Subsection 4.2.3. To demonstrate the different amount of streak artifacts in the different reconstructions, the images were processed with the Sobel edge enhancement filter (Figure 4.12). The streak artifacts appear as straight bright lines. It is clear that the 4D-VOI has the least amount of streak artifact, followed by the MB reconstruction. The noise increase in the MB reconstruction is apparent in this image. The numerous streak artifacts in the full 4D reconstructions are greatly intensified in the edge-filtered image. The CNR for the 4D-VOI method (11.4) is better than that for the other methods because of the lack of streak and other artifacts that increase measured noise. The full 4D reconstruction has a slightly higher CNR (2.2) than the MB reconstruction (1.5). CNR in the MB reconstruction was degraded because of an increase in noise and texture artifacts.

4.2.3 Motion assessment in phantom study

The sphere motion in the 4D-VOI reconstruction in the chest phantom study was assessed. Since the VOI regions are, by definition, identical in the 4D-VOI and full 4D reconstruction, the following measurements apply to both reconstructions. A line profile was taken through the VOI in the direction of object motion (Figure 4.13). The true size of the sphere was 20 mm, but since the line profile was taken away from the center of the sphere, the ideal line profile width was 17 mm. The line profiles for the end-inhale and the end-exhale phase images in the 4D-VOI reconstruction are shown in Figure 4.14, and the line profiles for the MB reconstruction are shown in Figure 4.15. In the profiles for the 4D-VOI reconstruction, the sphere has a sharp edge and the movement of the sphere from the end-exhale to the end-inhale phases is apparent. The size of the sphere was 19.8 and 19.9 mm for the end-exhale and the end-inhale phase images, respectively, whereas the true size is 17 mm. This negligible amount of blurring may be expected from partial volume averaging (slice thickness is 2.5 mm), or even by the definition of the measurement (for instance, full-width half-maximum instead of full-width tenth maximum.) The measured motion displacement was 17 mm, which is very close to the actual value of 18-mm. To conclude, any motion blur or loss of spatial resolution introduced by the 4D-VOI and the full-4D reconstructions is negligible. Last, a mean intensity shift of about 100 HU was also observed between the end-exhale and the end-inhale phases. This is due to residual streak artifact inside the VOI that could not be eliminated by the 4D-VOI method. Nevertheless, for the purpose of localization, the sphere location and the trajectory were sufficiently clear.

On the other hand, the MB reconstruction algorithm showed a large motion blur for the sphere (Figure 4.15). The size of the sphere was 29.1 and 29.9 mm the end-exhale and the end-inhale phase images, respectively, whereas the true size is 17 mm. This indicates a motion blur of about 12.5 mm. The line profiles also showed only

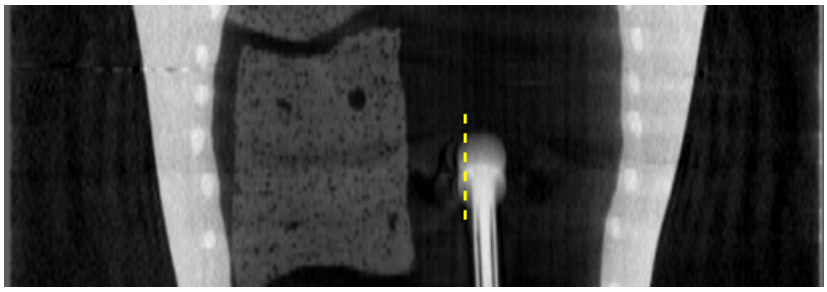

Figure 4.13: Line profile used to assess motion resolution. Used with permission from *Medical Physics* journal (Ahmad *et al.*, 2011) [50].

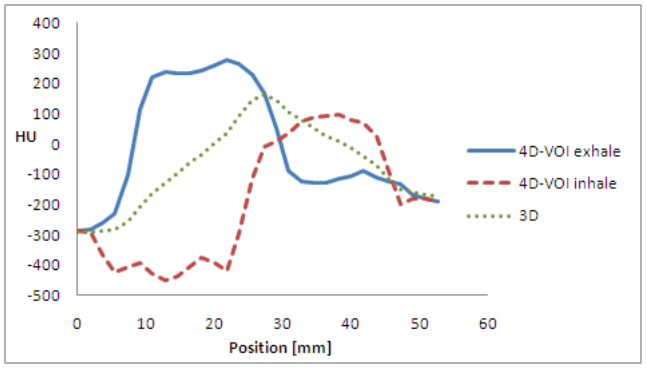

Figure 4.14: Line profiles for the 4D-VOI reconstruction at end-exhale and end-inhale phases. Line profile for 3D reconstruction is also shown. Used with permission from *Medical Physics* journal (Ahmad *et al.*, 2011) [50].

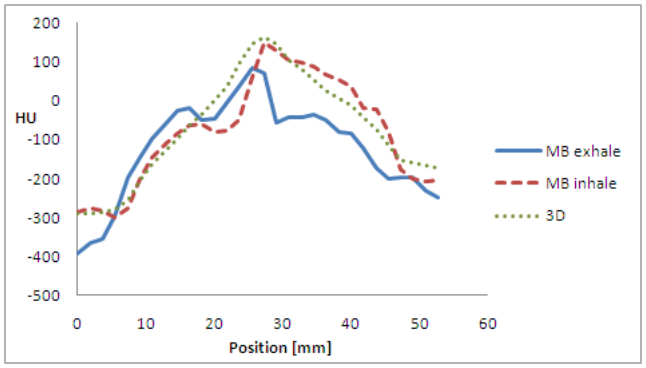

Figure 4.15: Line profiles for the MB reconstruction at end-exhale and end-inhale phases. Line profile for 3D reconstruction is also shown. Used with permission from *Medical Physics* journal (Ahmad *et al.*, 2011) [50].

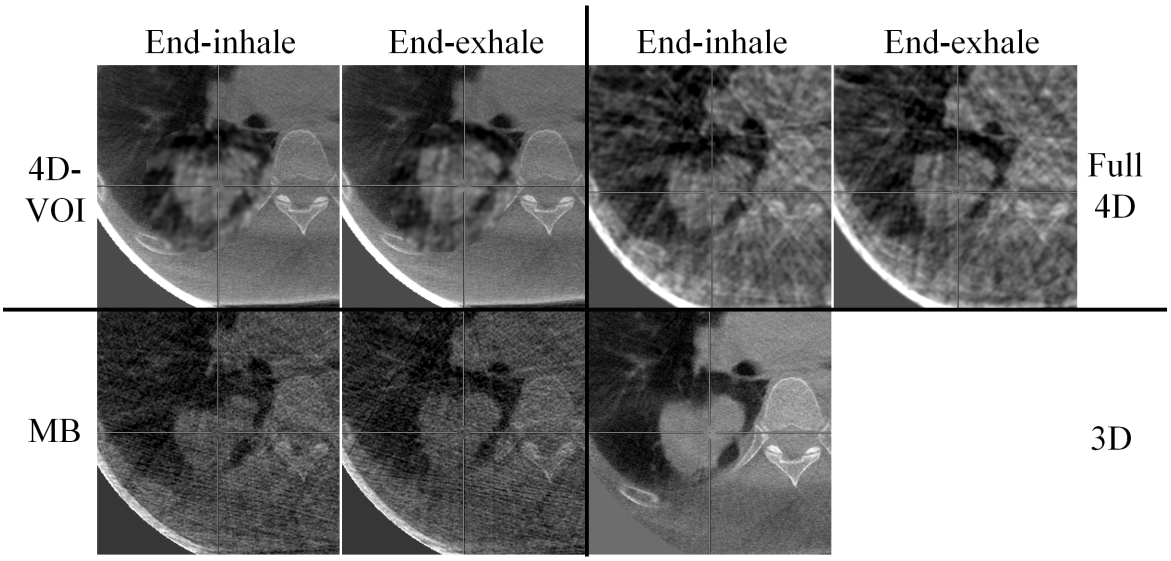

Figure 4.16: Patient 1, axial views for the 4D-VOI, full 4D, MB, and 3D reconstructions. Zoomed-in view of tumor. Top left: 4D-VOI, top right: Full 4D, bottom left: MB, bottom right: 3D. Image size: 13 cm. Window/level: 500/0. Used with permission from *Medical Physics* journal (Ahmad *et al.*, 2011) [50].

a 3-mm sphere displacement between the two phases (actual displacement was 18 mm). To conclude, the sphere size, edge, and motion were not accurate in the MB reconstruction for this chest phantom study.

4.2.4 Patient studies

The 4D image sets for the two patient studies are shown in Figures 4.16 to 4.21. Because of increased noise in the VOI region, there is an obvious visual discontinuity at the boundary of the VOI. To equalize the noise with that of the background, the VOI region was smoothed with a 2D Gaussian filter of 1.5 voxel width (0.73 mm). For a fair comparison between the 4D-VOI and full 4D reconstructions, the same Gaussian filtering was applied after reconstruction to smooth the full 4D reconstruction.

Light gray cross-hairs are included as a reference for respiratory motion. Patient 1 had a large 5-cm-diameter tumor in the right lung. It was known from 4D-CT

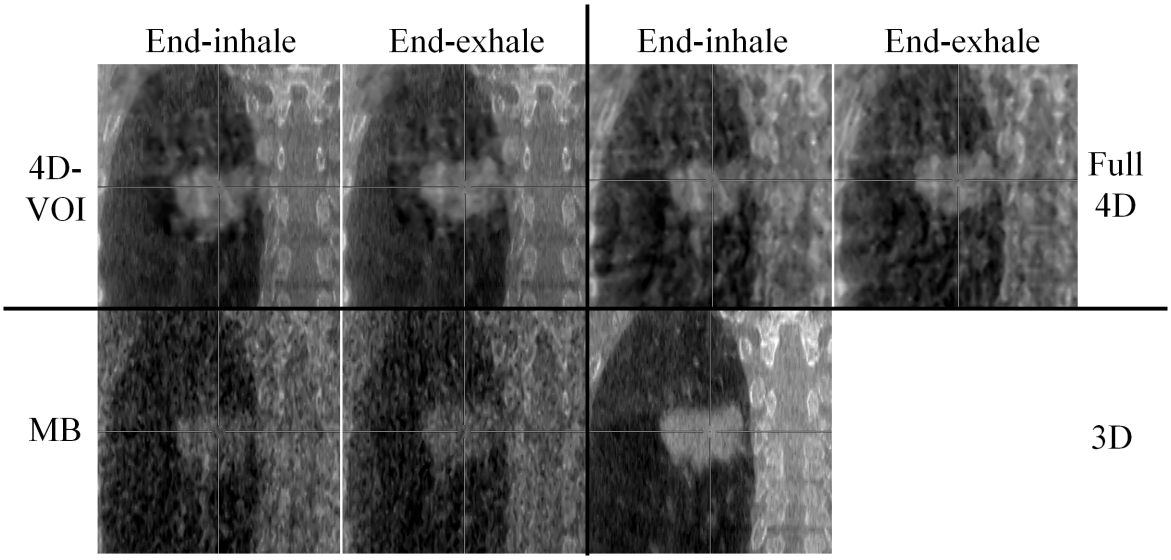

Figure 4.17: Patient 1, coronal views for the 4D-VOI, full 4D, MB, and 3D reconstructions. The tumor moves 1.5 cm in the superior-inferior direction. Top left: 4D-VOI, top right: Full 4D, bottom left: MB, bottom right: 3D. Zoomed-in view of tumor. Image size: 13 cm. Window/level: 500/0. Used with permission from *Medical Physics* journal (Ahmad *et al.*, 2011) [50].

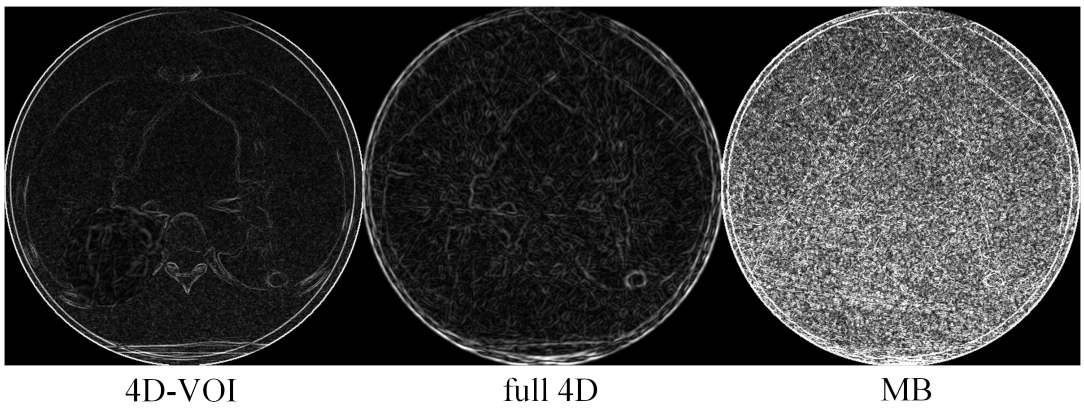

Figure 4.18: Patient 1, edge-detection filter processing on the 4D-VOI, full 4D, and MB reconstructions. Used with permission from *Medical Physics* journal (Ahmad *et al.*, 2011) [50].

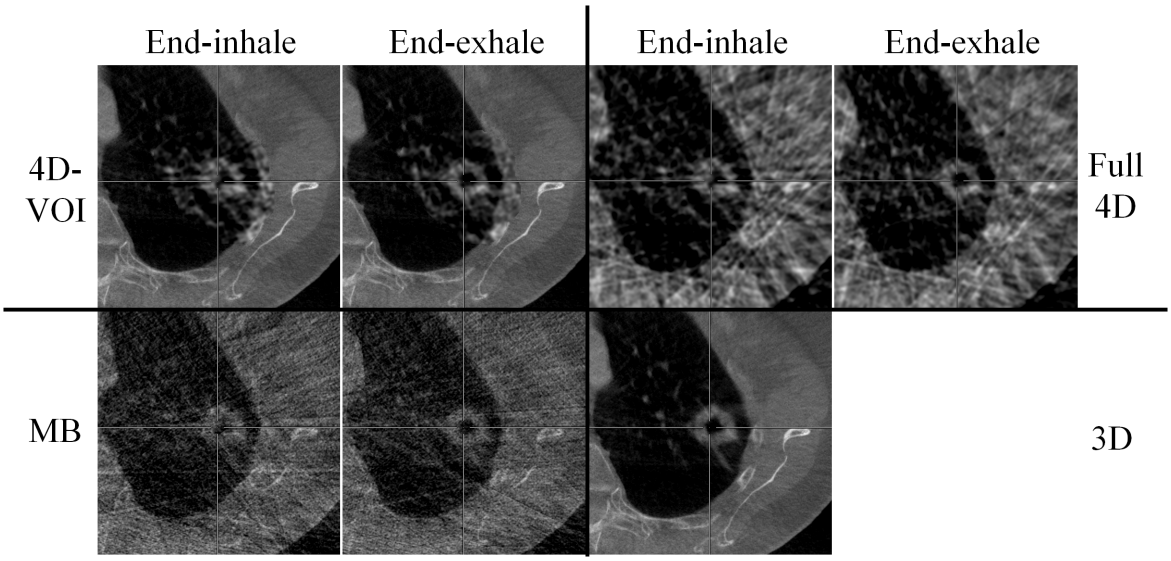

Figure 4.19: Patient 2, axial views for the 4D-VOI, full 4D, MB, and 3D reconstructions. Zoomed-in view of tumor. Top left: 4D-VOI, top right: Full 4D, bottom left: MB, bottom right: 3D. Image size: 13 cm. Window/level: 500/0. Used with permission from *Medical Physics* journal (Ahmad *et al.*, 2011) [50].

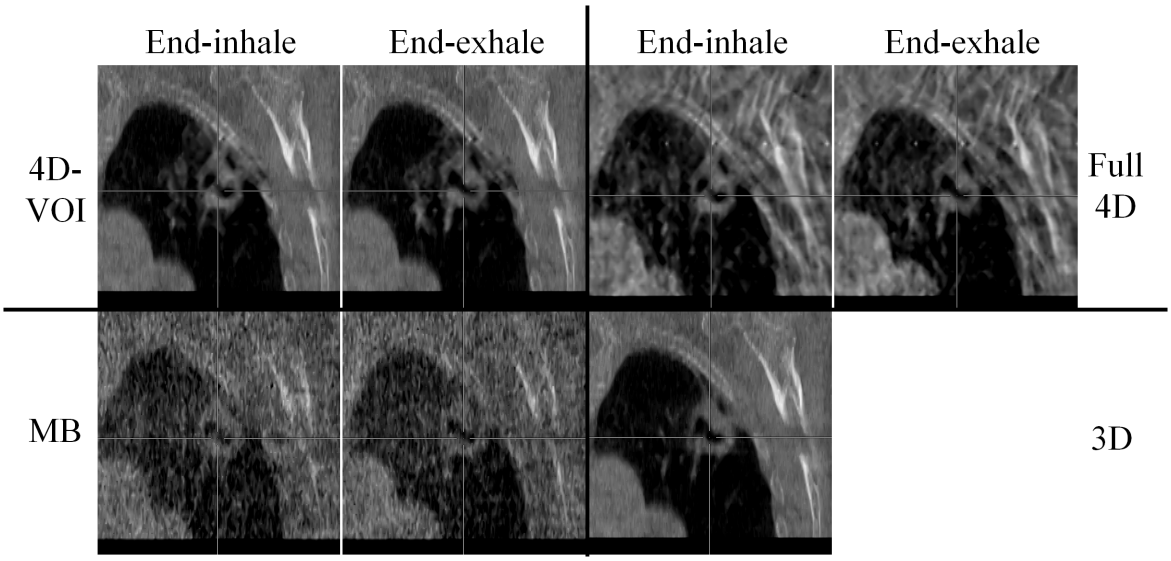

Figure 4.20: Patient 2, coronal views for the 4D-VOI, full 4D, MB, and 3D reconstructions. The tumor moves 1.5 cm in the superior-inferior direction. Top left: 4D-VOI, top right: Full 4D, bottom left: MB, bottom right: 3D. Zoomed-in view of tumor. Image size: 13 cm. Window/level: 500/0. Used with permission from *Medical Physics* journal (Ahmad *et al.*, 2011) [50].

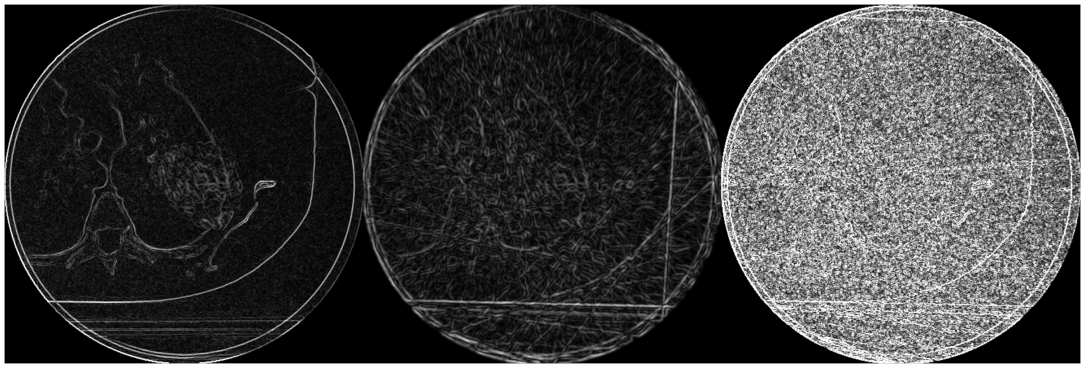

Figure 4.21: Patient 2, edge-detection filter processing on the 4D-VOI, full 4D, and MB reconstructions. Used with permission from *Medical Physics* journal (Ahmad *et al.*, 2011) [50].

imaging in treatment planning that this tumor had a known superior- inferior motion of 15 mm with a period of 2.8 s; the tumor motion was correctly measured by all three methods (4D-VOI, full 4D, and MB). Patient 2 had a 3-cm tumor near the apex of the left lung known to move only 3 mm in the anterior-posterior direction with a period of 3.2 s. Again, all three methods correctly measured the tumor motion.

The 4D-VOI images show no streak artifact except inside the VOI, whereas the full 4D images show artifact over the entire image. In the full 4D images for patient 1 (Figures 4.16 and 4.17), many structure boundaries are lost (the shape of the vertebral body and the ribs). The relatively uniform region in the heart shows large variations in the full 4D image. The edge-filtered images in Figure 4.18 show streak artifacts along the heart and the chest wall boundaries. For patient 2, the full 4D reconstruction produced streak artifacts which distorted the vertebrae, scapula, and other bony anatomy (Figures 4.19 and 4.20). The edge-filtered image for the full 4D reconstruction (Figure 4.21) shows strong streak artifacts tangent to the patient skin and the table.

The MB reconstructions reduced the streak artifacts but did not completely eliminate them. Regions outside the VOI show better quality than the full 4D recon-

struction because of the streak artifact reduction. The MB reconstruction also added a hazy texture artifact. The coronal views (Figures 4.17 and 4.20) suffer more from this artifact than the axial views The tumor boundary and the shape of the ribs in the MB images are not as clear as in the other reconstructions. Further investigation is warranted to explain the poor image quality in the coronal views of the MB reconstruction.

Although a motion blur was seen in the phantom study, this degradation was not observed in these patient studies, possibly because the data acquisitions were different. For the phantom study, an asymmetric (i.e., offset) detector was used with a 360-deg gantry rotation, while the patient studies used a symmetric detector with 200-deg gantry rotation. An offset detector does not necessarily illuminate the target lesion in all views. Furthermore, some parts of the field of view may receive redundant (conjugate) views in a 360-deg rotation, would not happen with a 200-deg rotation. Again, further investigation of the MB algorithm may be needed to understand the relationship between the motion blur and the configuration of data acquisition.

The CNR was measured for the heart against the lung background. It was not surprising that the 4D-VOI reconstruction had the largest CNR (7.6), because it was composed mostly of the static (3D) image, which was reconstructed from a large number of projections. The CNR of the full-4D (2.5) reconstruction was low due to streak artifacts. The CNR was slightly lower for the MB reconstruction (2.4) than for the full 4D reconstruction. CNR in the MB reconstruction was degraded from the amplification of quantum noise in the algorithm.

The 4D-VOI reconstruction is computationally practical from a clinical perspective since it uses Feldkamp reconstruction. The 4D-VOI reconstruction was implemented using a graphics processing unit (GPU) [54, 55, 56, 57] and a computation time of 40 s was measured. Appendix A provides a detailed account of the speed

up with GPU-based reconstruction. Many algorithms proposed for 4D-CBCT do not have clinically practical computation times.

4.3 Discussion

The 4D-VOI reconstruction improves image quality by relaxing the 4D requirement: *i.e.* only a VOI is reconstructed in 4D, while the rest of the image is static. This strategy makes use of the full (unsorted) projection set to improve the reconstruction of the region outside the VOI. This region may contain important anatomical landmarks and organs-at-risk. The reconstruction of these structures is important for accurate patient setup in radiation therapy. For instance, the lung tumor could be localized accurately but a bulk patient rotation could introduce large treatment errors. The 4D-VOI reconstruction reduces undersampling artifacts in the region outside the VOI; therefore, it is an improvement over the standard FBP reconstruction.

There are several other advantages in the 4D-VOI reconstruction method. The 4D portion of the image is inherently and automatically registered to the 3D background anatomy. The 4D-VOI method does not require a symmetric (centered) detector configuration, so it can be used to reconstruct a large field of view using an asymmetric (offset) detector. This coverage can thus include the body outline for most patients larger than 25 cm in diameter. Furthermore, the 4D-VOI reconstruction requires much less computation time than iterative reconstruction and can be implemented in a clinical setting.

One limitation is that the 4D-VOI reconstruction does require a human intervention in the VOI selection. However, this limitation is mitigated by the fact that such a VOI is typically previously determined during treatment planning. This information can be imported from the treatment plan and used to determine the VOI in the 4D-VOI reconstruction. Although the PTV from treatment planning was chosen

as the VOI, other choices are possible. The GTV is a smaller volume based on the extent of the tumor seen in treatment simulation imaging. The PTV encompasses a larger volume than the GTV. The PTV structure includes safety margins for respiratory motion, setup uncertainty, and extended microscopic disease not captured in the GTV [12]. Since this work is not directly concerned with microscopic disease or setup uncertainty in image reconstruction, it may be better to choose a smaller VOI. The GTV or GTV + small expansion may be good choices. With a smaller VOI based on the GTV, one may be better able to detect cases in which tumor moves outside the boundary of the VOI, and adjust accordingly.

4D-VOI reconstruction effectively reduces undersampling artifacts and resolves lung tumor motion in 4D-CBCT when using undersampled acquisition data. The 4D-VOI reconstruction is computationally inexpensive compared with more sophisticated iterative algorithms which may not be clinically practical. The improved image quality is achieved with a minor modification to the standard Feldkamp FBP algorithm. Compared with other 4D-CBCT image reconstructions that relate to streak artifact reduction and incomplete data sampling, the 4D-VOI reconstruction is an attractive alternative in 4D-CBCT for reconstructing target motion with 1-min acquisitions with reduced undersampling artifacts.

Chapter 5

Iterative 4D-VOI Reconstruction

This chapter presents an iterative image reconstruction algorithm for undersampled acquisition data in 4D-CBCT. This algorithm, termed iterative 4D volume-of-interest (I4D-VOI) reconstruction, is based on the previous (4D-VOI) reconstruction method [50]. It uses fully-sampled projection data for high-quality reconstruction outside the VOI. However, it also improves upon the previous method by incorporating fully-sampled 3D image data outside the VOI into the iterative reconstruction inside the VOI. The result is reduced undersampling artifacts and improved image quality in the VOI containing the tumor. The improvement is achieved without any sparsity constraints or any other regularization function. Lastly, this method is conceptually and computationally simple and can be easily implemented in the clinic.

5.1 Methods

5.1.1 Algorithm specification

Iterative image reconstruction deals generally with the problem of finding the solution $\vec{x}$ to the linear system of equations $\vec{A}_n \cdot \vec{x} = b_n$ for $n = 1, 2, \ldots, N$, where b_n is the n^{th}

point projection measurement, $\vec{A}_n$ is the projection operator for the n^{th} projection measurement, and N is the total number of projection measurements. The solution $\vec{x}$ is a vector $\{x_1, x_2, \ldots, x_m, \ldots, x_K\}$ of the values of K image voxels (or other image basis functions). In 4D image reconstruction, the solutions to several such problems are sought independently of one another, one for each time point or respiratory phase. In practice, these linear systems are very large and singular, and do not lend themselves to solutions via direct inversion. One iterative method of solving a large set of equations is the algebraic reconstruction technique (ART), which updates a given estimate of the solution, $\vec{x}^{(k)}$ by the formula:

$$\vec{x}^{(k+1)} = \vec{x}^{k} + \beta(b_n - \vec{A}_n \cdot \vec{x}^{(k)}) \frac{\vec{A}_n}{\sum_m {A_{n,m}}^2} \ , \tag{5.1}$$

where $A_{n,m}$ is the coefficient of $\vec{A}_n$ corresponding to pixel m.

In this update equation, $\vec{x}^{(k+1)}$ is the image update, and β is the relaxation parameter, valued between 0 and 1, which is used to reduce the influence of noise in b_n or inaccuracies in the system modeling $\vec{A}_n$. The update is applied sequentially for all N projection data. This constitutes one iteration of the algorithm. This process is repeated for either a fixed number of iterations or until the solution meets some convergence criteria. (The initial iterate $\vec{x}^{(0)}$ can be chosen as all zeros. In 4D reconstruction the motion-averaged reconstructed image, which is an approximate solution to the equations, can be used.)

Because of the computationally expensive forward projection operation and the serial processing of the projection data, the ART algorithm may require long computation times. Therefore the simultaneous algebraic reconstruction technique (SART) [58] was used instead. SART uses multiple (or all) projection data simultaneously in one image update. In the SART reconstruction, the projection data b_n are organized

into subsets S_i. The SART update equation for each voxel x_m is

$$x_m^{(k+1)} = x_m^{(k)} + \beta \left[\sum_{n \in S_i} \left(\frac{b_n - \vec{A}_n \cdot \vec{x}^{(k)}}{\sum_m A_{n,m}} \right) A_{n,m} \right] \Bigg/ \sum_{n \in S_i} A_{n,m} \ . \tag{5.2}$$

The summation in the denominator is the normalization factor for the simultaneous weighted average update, and the weights for a given projection n are $A_{n,m}$.

The I4D-VOI algorithm, which is a modification of SART, is defined by the following steps:

1. Reconstruct a prior image from the full unsorted projection data and set this image as the initial estimate in the 4D reconstruction.

2. Select a VOI that contains the object(s) influenced by respiratory motion.

3. Sort the projection data into respiratory phases.

4. Apply the SART algorithm on the phase-sorted data, updating *only the region inside the VOI*.

In the first step, the prior image lacks temporal resolution because the full dataset is not sorted by respiratory phase. However, it is fully sampled with respect to projection angles, and does not suffer from undersampling artifacts. The final step is a modification in the SART update and can be mathematically expressed as

$$x_m^{(k+1)} = x_m^{(k)} + \beta \left[\sum_{n \in S_i} \left(\frac{b_n - \vec{A}_n \cdot \vec{x}^{(k)}}{\sum_m A_{n,m}} \right) A_{n,m} M_m \right] \Bigg/ \sum_{n \in S_i} A_{n,m} \ , \tag{5.3}$$

where $\vec{M} = \{M_1, M_2, \ldots, M_m, \ldots, M_K\}$ is a binary mask variable equal to 1 for m inside the VOI and 0 for m outside the VOI. Overall, this equation represents the situation in which the SART update is masked to zero outside the VOI.

In this implementation, each subset S_i is the set of projections b_n for a single cone-beam view (henceforth called a "cone-beam projection"). Thus a single update is applied for one cone-beam projection, and the algorithm processes cone-beam projections sequentially. All projection data b_n within one cone-beam projection were processed in parallel using graphics processing unit (GPU) computing hardware, accelerating the computation by a factor of about 100 compared to a CPU implementation. (Appendix A provides a detailed account of the speed up with GPU-based reconstruction.) An additional computational speed-up was possible because projection rays that did not intersect the VOI were not used. That is, if $\vec{A}_n \cdot \vec{M} = 0$, then the corresponding term n in the summation in equation (5.3) can be omitted. The terms $\vec{A}_n \cdot \vec{M}$ were pre-computed and the corresponding terms in the summation were omitted as needed.

5.1.2 Reconstruction algorithm evaluation

The iterative 4D-VOI reconstruction was compared against the standard Feldkamp filtered back-projection algorithm [39] (FBP), and against ordinary SART, i.e. SART without the VOI restriction. The same raw projection dataset was used in the reconstructions comparison. The reconstruction results were compared using the root mean square image error (RMSE) metric against the ideal image.

Streak artifacts can be evaluated using total variation (TV), which is defined over region R in image $I(x, y, z)$ as:

$$TV = \frac{\sqrt{\int_R |\nabla I|^2 \cdot dV}}{\int_R dV} \tag{5.4}$$

The gradient operation ∇I computes the intensity differences among neighboring pixels in image I. The gradient operation therefore is sensitive to edges such as in

streak artifacts. Here TV is normalized by the volume of region R in order to compare TV in regions of different sizes. TV responds to streak artifacts but it is also sensitive to true edges in the image. If the true image I_{ref} is known (such as in a phantom study), the sensitivity to true edges can be removed using an adjusted total variation metric TV_{adj}:

$$TV_{adj} = \frac{\sqrt{\int_R |\nabla(I - I_{ref})|^2 \cdot dV}}{\int_R dV} \tag{5.5}$$

The TV_{adj} metric was used to compare streak artifacts among the different reconstructions.

Since one of the main attractive features of the I4D-VOI reconstruction is computational simplicity relative to other iterative algorithms, the computation time for each reconstruction was also tabulated. All image reconstructions were performed on a desktop workstation using a Tesla C1060 graphics processing unit (NVIDIA Corporation, Santa Clara, CA) for accelerated computation.

5.1.3 Mathematical phantom study

The mathematical phantom from Chapter 4 was reused in this experiment (see Figure 4.2). The relaxation parameter $\beta = 1$ and iteration number $I = 20$ were chosen in both the SART and iterative ROI reconstructions.

5.1.4 Patient studies

Retrospective 4D-CBCT patient studies were performed using data from lung cancer patients who had received 4D-CBCT for stereotactic body radiation therapy. The raw cone-beam projection data and the respiratory tracking data from two patient studies were used. The Varian RPM system was used to obtain the patient respiratory signal during CBCT acquisition. Patient 1 had a large 40-mm diameter lung tumor that

moved with a 2.8-sec breathing cycle. Patient 2 had a smaller 10-mm diameter lung tumor that moved with a 6-sec breathing cycle.

The two patients had long acquisitions (5-min for Patient 1 and 8-min for Patient 2) which produced adequately-sampled 4D-CBCT datasets. The image reconstructions and trajectories from these datasets serve as the gold standard for comparison. Since this work is concerned with short acquisition 4D-CBCT, the number of projections of the long acquisitions was reduce in order to simulate shorter scan times.

The projections were removed in a way that represented an accurate number of breath cycles for the shortened scan time. For instance, to reduce the scan time by 80%, the projection data for only one of five breath cycles were retained, while data for the other four breath cycles were discarded. This process produced an angular distribution of projection angles that was a realistic representation of a 1-min scan. After the scan times of the datasets were reduced, there were 397 and 762 projections for 1-min and 2-min acquisition for patients 1 and 2, respectively. The data were sorted into eight respiratory phases; after sorting there was an average of 49.6 and 91.1 cone-beam projections in patient studies 1 and 2, respectively.

The major difference between patient studies 1 and 2 is that the tumor was smaller, moved with a longer respiratory cycle, and was more mobile in Patient 2 than in Patient 1. As an additional difference, an offset detector (half-fan) configuration was used to obtain a larger field of view for Patient 2. Targets with longer respiratory cycles have poorer angular projection sampling after projection sorting, resulting in more undersampling artifacts. The offset detector configuration produces worse projection data sampling than the centered detector configuration. (See chapter 3 and Ref. [35]). For these reasons, Patient 1 represents an "easy" case and Patient 2 represents a "difficult" case in reconstructing the moving target. Therefore, the scan time chosen in this study was nearly double for Patient 2 than for Patient 1. The

parameters for both patient studies are listed in Table 5.1.

Table 5.1: I4D-VOI patient studies parameters

Parameter	Patient 1	Patient 2
Tumor size (cm)	4	2
Motion amplitude (mm)	5	13
Motion period (s)	2.9	3.1
Scan time (s)	54	121
Number of projections	397	762
Rotation	200°	360°
Detector configuration	centered	offset
Tube voltage (kVp)	120	120
Tube current (mA)	50	20
Pulse width (ms)	25	20

Generally, a radiation treatment plan with a planning target volume (PTV) is available before a CBCT scan. The PTV may be used as the VOI in the I4D-VOI reconstruction. If the I4D-VOI reconstruction shows the target crossing the boundary, this serves as a flag for either repositioning the patient or re-planning the treatment. For patient study 1, a radiation treatment plan was available and the PTV was imported as the VOI. For the I4D-VOI reconstruction of the moving calcified plaque in patient study 1, the VOI was created by deriving the maximum intensity projection (MIP) image taken from the gold-standard images from 5-min data. This MIP was then expanded uniformly by 5 mm, which is a typical margin added to targets to account for setup uncertainty. For patient study 2, the PTV was not available, so the same MIP procedure was used to define the VOI.

5.2 Results

5.2.1 Mathematical phantom study

The reconstructed images of the mathematical motion phantom are shown in Figure 5.1. The filtered back-projection images show severe streak (undersampling) artifacts. Those artifacts are less pronounced in the SART reconstruction, but the undersampling leads to a low contrast, blurry appearance. Finally, the iterative ROI reconstructions show excellent image quality outside the ROI because those regions are reconstructed from fully-sampled (temporally unsorted) projection data. The image quality has also improved *inside* the ROI, as the moving circle has a more uniform appearance and sharper boundary. This results shows that the prior information from the motion-averaged image improved the reconstruction.

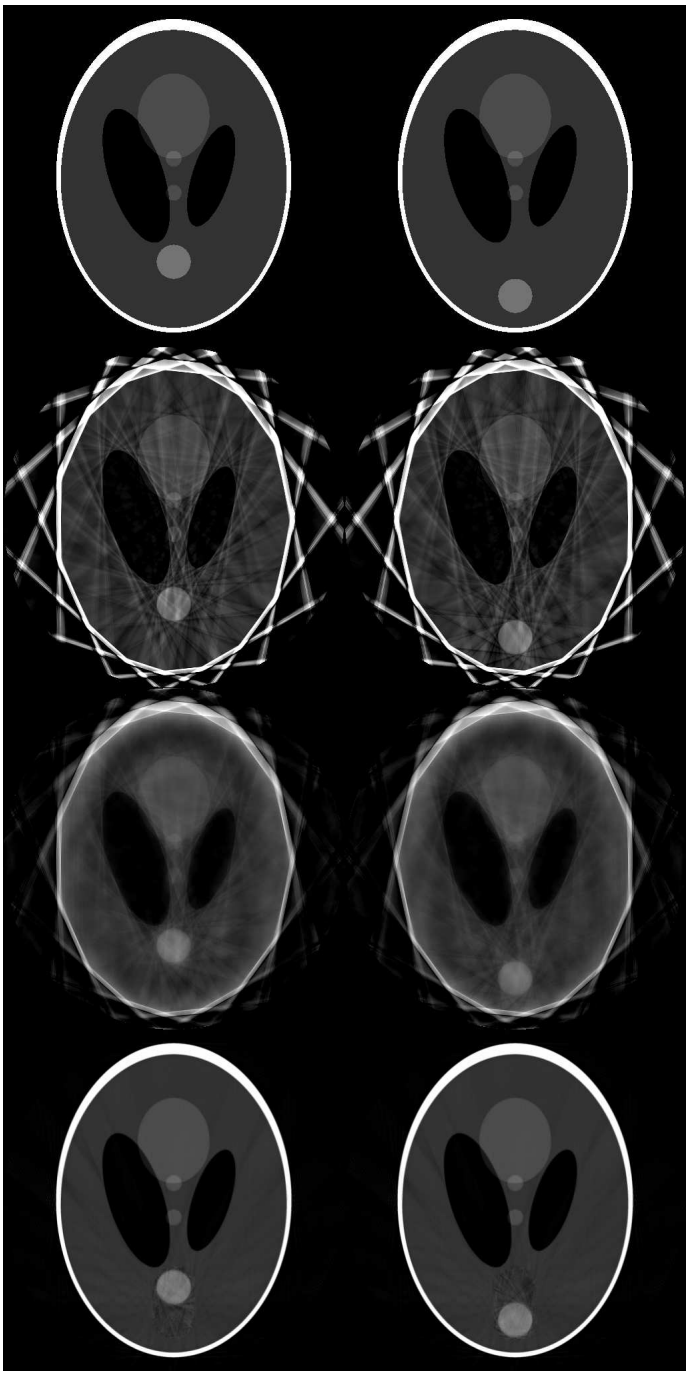

Figure 5.1: 0% phase (left column) and 50% phase (right column) images of the mathematical motion phantom. Top row: Ideal phantom. Second row: FBP reconstruction. Third row: SART reconstruction. Fourth row: iterative ROI reconstruction.

The quantitative image quality improvement was demonstrated in the RMS image

errors listed in Table 5.2 for the different reconstructions. Considering all motion phases, the iterative ROI reconstruction has only 16% and 33% of the RMSE of the FBP and full iterative reconstructions, respectively, when examining the entire image. This improvement is expected because the iterative ROI reconstruction uses the larger, fully sampled projection data set for reconstruction of the region outside the ROI. However, the image reconstruction accuracy also improved *inside* the ROI. The iterative ROI reconstruction had 57% and 74% of the RMSE of the FBP and SART reconstructions, respectively, inside the ROI. The iterative ROI reconstruction also shows greater uniformity inside the moving disk, and sharper disk boundary. These improvements are shown in the reconstruction line profiles in Figure 5.3. The location of the line profile measurement is depicted in Figure 5.2.

Table 5.3 shows that the iterative ROI reconstruction also reduced the undersampling streak artifacts, as measured with the TV_{adj} metric. Considering all motion phases, the iterative ROI reconstruction has only 30% and 60% of the streaking artifacts of the FBP and SART reconstructions, respectively, when examining the entire image. Inside the ROI, the iterative ROI reconstruction had only 79% of the streaking artifacts of the FBP reconstruction, but had the same amount of streaking artifact as the SART reconstruction. The iterative ROI and SART reconstructions were different with $p = 0.078$ and $p = 0.697$, for the 0% and 50% phases respectively, using the pixel-wise paired t-test; therefore these two reconstructions were considered to have the same amount of streaking artifact inside the ROI. For all other RMSE and TV_{adj} comparisons, the results were different with all p-values $< 10^{-4}$.

Table 5.2: Root mean squared image reconstruction errors for the moving mathematical phantom at 0% and 50% motion phases.

	RMSE: entire image		RMSE: inside ROI	
Reconstruction	0% phase	50% phase	0% phase	50% phase
FBP	0.301	0.302	0.063	0.064
SART	0.141	0.141	0.050	0.047
iterative ROI	0.047	0.047	0.037	0.035

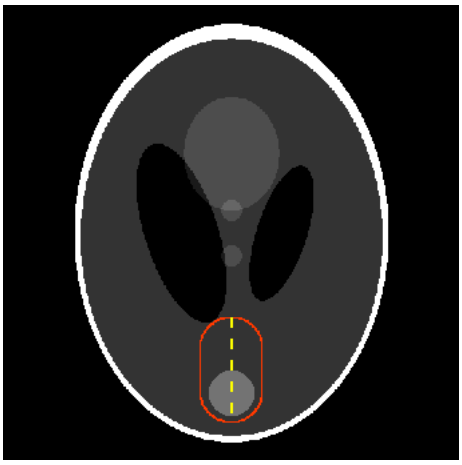

Figure 5.2: The dashed vertical line is used to measure the intensity line profile. The solid line indicates the ROI used in the iterative ROI reconstruction.

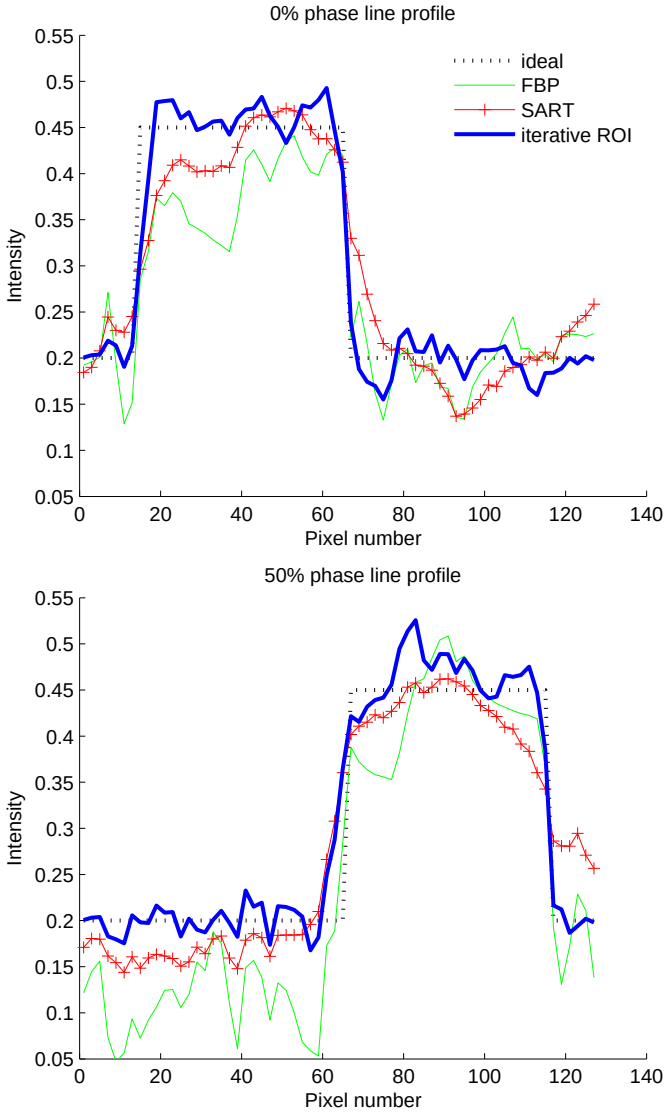

Figure 5.3: Line profiles of the mathematical phantom reconstructions in the ROI. Top-0% phase. Bottom-50% phase.

Table 5.3: Adjusted total variation metric for streak artifacts for the moving mathematical phantom at 0% and 50% motion phases (in 10^{-4} intensity units).

	TV_{adj}: entire image		TV_{adj}: inside ROI	
Reconstruction	0% phase	50% phase	0% phase	50% phase
FBP	3.29	3.29	3.98	3.94
SART	1.65	1.66	3.18	3.06
iterative ROI	0.99	0.99	3.24	3.07

5.2.2 Patient studies

Patient study 1 had a 1-min acquisition. The reconstructed images for Patient 1 are shown in Figures 5.4 and 5.5. The tumor boundary is apparent in the 5-min scan images, which were considered as a gold standard. The FBP reconstruction shows severe undersampling artifacts. These artifacts appear as streaks in the axial views and alternating dark and bright vertical lines in the coronal views. The SART reconstructions show a washed-out appearance. Last, the I4D-VOI reconstruction shows good image quality outside the VOI. The region inside the VOI shows much fewer undersampling artifacts compared to the FBP reconstruction.

The same results are true for the images of the mobile calcification in patient study 1 (Figure 5.6). The calcification motion is apparent in the I4D-VOI reconstruction and the region outside the VOI has much fewer artifacts than the other reconstructions. The VOI region also has less artifact, especially compared to the FBP reconstruction.

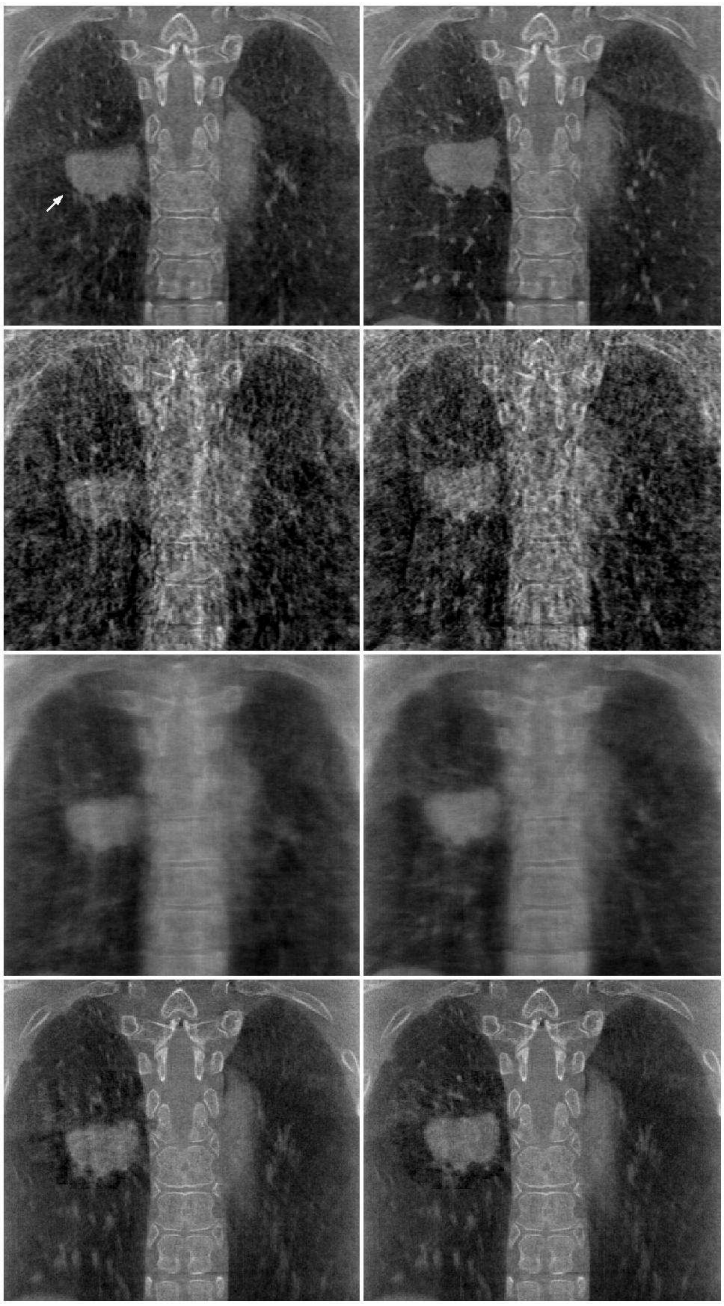

Figure 5.4: End-inhale (left column) and end-exhale (right column) phase images of Patient 1's lung tumor in the coronal format. Top row: gold standard from fully-sampled data. Second row: FBP reconstruction. Third row: SART reconstruction. Fourth row: I4D-VOI reconstruction.

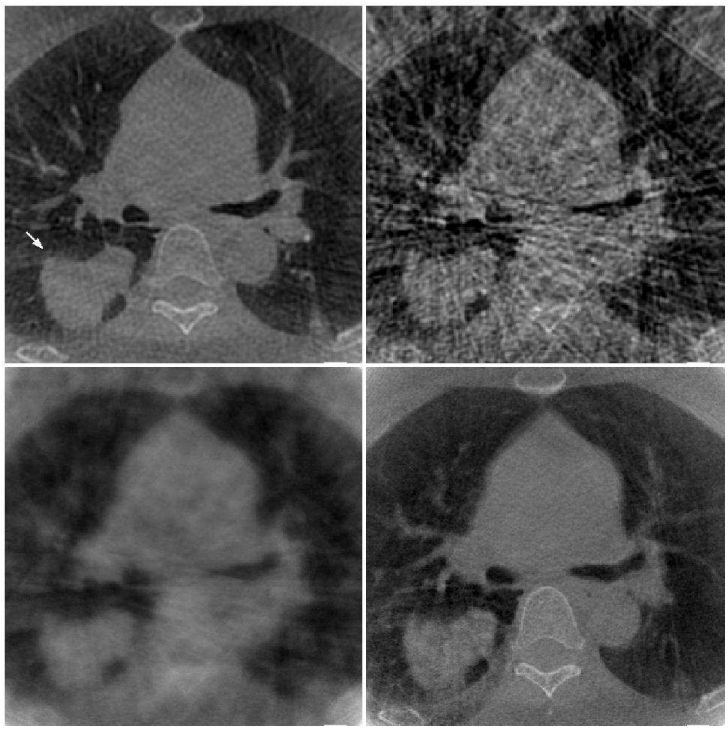

Figure 5.5: End-exhale phase images of Patient 1's lung tumor in the axial format. Top left: gold standard from fully-sampled data. Top right: FBP reconstruction. Bottom left: SART reconstruction. Bottom right: I4D-VOI reconstruction.

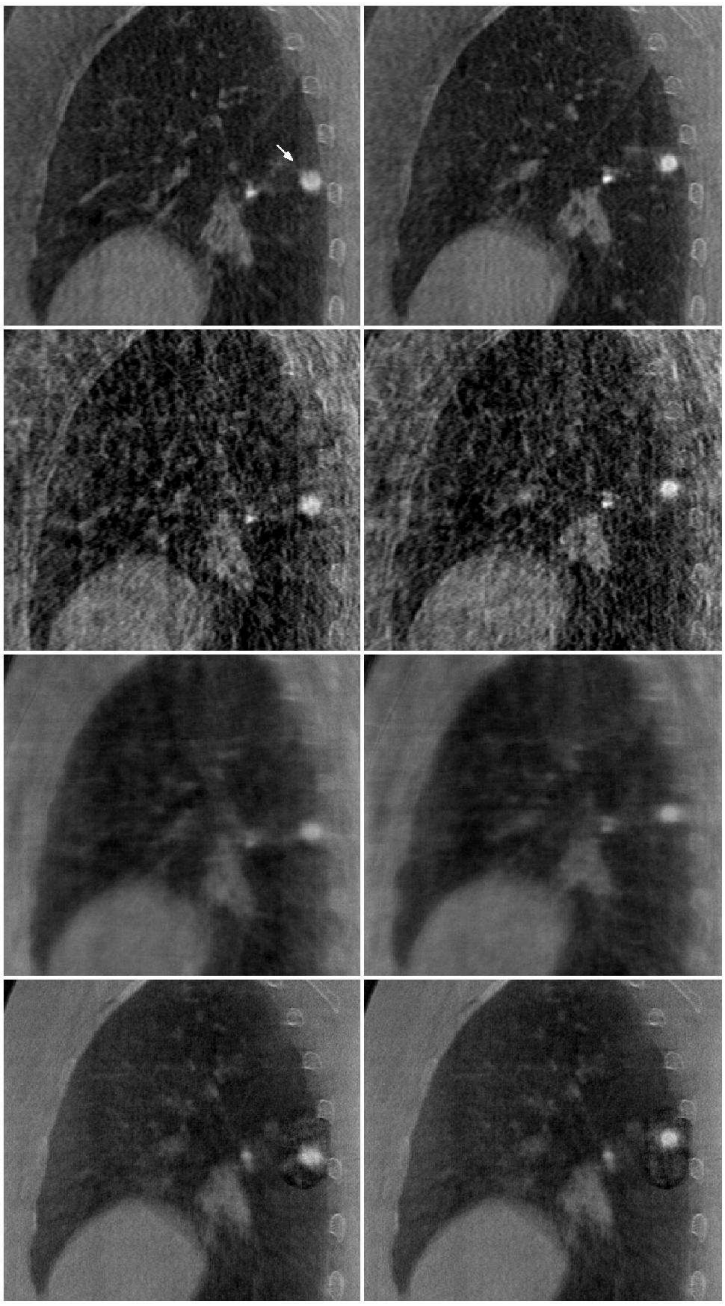

Figure 5.6: End-inhale (left column) and end-exhale (right column) phase images of Patient 1's lung calcification in the sagittal format. Top row: gold standard from fully-sampled data. Second row: FBP reconstruction. Third row: SART reconstruction. Fourth row: I4D-VOI reconstruction.

The acquisition time for Patient study 2 was 2 min. The reconstructions for Patient 2 are shown in Figures 5.7 and 5.8. This patient had a fiducial marker surgically

implanted into the tumor bed. The tumor and its motion are apparent in the 8-min scan images, which were considered as a gold standard. The FBP reconstructions are severely impacted by streak artifacts. The SART reconstruction shows fewer artifacts but the overall appearance is blurry and has low contrast for the chosen number of iterations I, and relaxation parameter β. The I4D-VOI reconstructions uses the same parameters I and β, but it shows better contrast than the full 4D reconstruction. In the axial format images, particularly in Fig. 5.8, the tumor has better contrast in the I4D-VOI image than in the SART image, and lower streak artifacts than the FBP image.

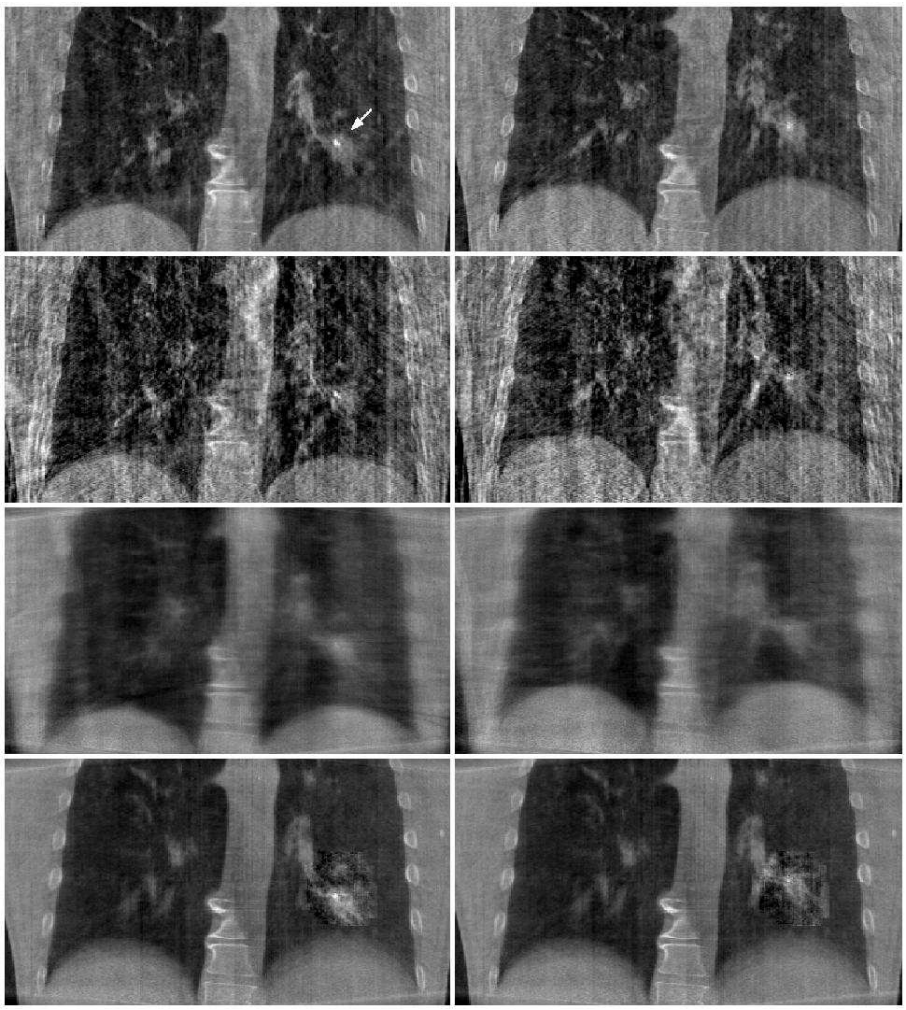

Figure 5.7: End-inhale (left column) and end-exhale (right column) phase images of Patient 2's lung tumor in the coronal format. Top row: gold standard from fully-sampled data. Second row: FBP reconstruction. Third row: SART reconstruction. Fourth row: I4D-VOI reconstruction.

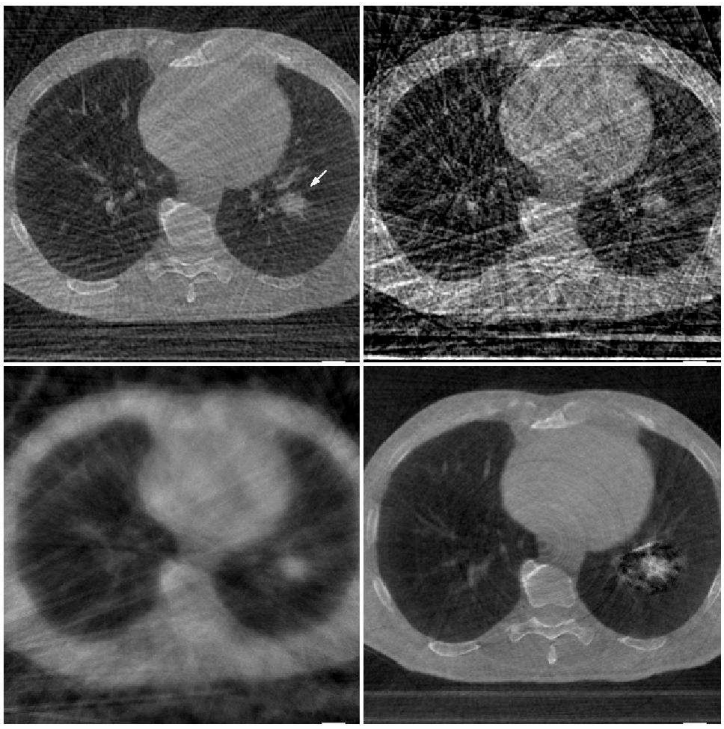

Figure 5.8: End-exhale phase images of Patient 2's lung tumor in the axial format. Top left: gold standard from fully-sampled data. Top right: FBP reconstruction. Bottom left: SART reconstruction. Bottom right: I4D-VOI reconstruction.

For patient study 1, a relaxation parameter $\beta = 0.1$ was used to reduce noise and an iteration number $I = 20$. For patient study 2, the same parameters were initially used with good results, except that the metallic fiducial marker showed reduced contrast. To restore the contrast in the fiducial marker, $\beta = 0.8$ was used. However, this also increased noise. To compensate for the increased noise, I was reduced to 10. $\beta = 0.1$ is recommended generally for clinical data such as in this study, with an exception for cases with metallic fiducials. As a final note on the reconstruction parameter selections, β and I are SART parameters and are not unique to I4D-VOI. In all cases, the same β and I parameters were used for both the SART and I4D-VOI reconstructions.

5.2.3 Reconstruction times

The computation times for the FBP, SART, and I4D-VOI reconstructions are shown in Table 5.4. The size of each reconstructed image set was 512^3 and the size of each cone-beam projection was $512 * 384$. The computation time is directly proportional to the number of projections; the number of projections for each data set is listed in Table 5.4. The computation time is smallest for the analytic FBP reconstruction. The greatest computation time was for the SART reconstruction. Depending on the size of the VOI, the I4D-VOI algorithm was 3-5 times faster than the SART reconstruction. The speed-up was possible because the I4D-VOI algorithm reconstructs only a fraction of the full scanned volume. Furthermore, it processes only the fraction of projection data that correspond to the VOI (i.e. only those b_n for which $\vec{A}_n \cdot \vec{M} \neq 0$). The fraction of the scanned volume belonging to the VOI and the fraction of projection data corresponding to the VOI are listed in Table 5.4 for each case. Note that the reconstruction time was correlated with the size of the VOI as shown by reconstruction of two different VOIs in Patient study 1.

Table 5.4: Reconstruction times for the patient studies.

	Patient 1 (tumor)	Patient 1 (calcification)	Patient 2
FBP	2 min 17 sec		4 min 22 sec
SART	111 min 38 sec		103 min 2 sec
I4D-VOI	31 min 30 sec	24 min 50 sec	23 min 13 sec
number of cone-beam projections	397	397	729
number of iterations	20	20	10
fraction of volume in VOI	2.2%	0.21%	0.24%
fraction of raw data corresponding to VOI	9.8%	2.3%	3.8%

The reconstruction time for the prior image was not included in the overall reconstruction time. The prior image was reconstructed from adequately sampled data (*i.e.*

the full unsorted projection set). Therefore, an iterative algorithm is not required for reducing undersampling artifacts, and the prior image can be reconstructed using the computationally inexpensive FBP algorithm.

5.3 Discussion

This chapter presented a novel iterative algorithm for the reconstruction of a 4D volume-of-interest containing a moving radiotherapy target. In the simulation study, the I4D-VOI reconstruction significantly reduced the RMS image error and streak artifacts in the overall image compared to FBP and SART reconstructions ($p < 10^4$). Inside the VOI, the I4D-VOI reconstruction significantly reduced the RMS image error compared to FBP and SART and reduced the streaking undersampling artifacts compared to FBP ($p < 10^4$). The I4D-VOI reconstruction showed sharper boundaries in the moving object than SART. In the patient studies, the I4D-VOI reconstruction showed lower streak artifacts than FBP and greater contrast and sharpness than SART. I4D-VOI was 3-5 times faster than SART depending on the size of the VOI.

The I4D-VOI reconstruction improves image quality over standard FBP and SART reconstructions by incorporating prior image information and a VOI constraint. With undersampled projection data, the SART reconstruction without the VOI constraint has a large solution space. The desired solution is just one possible solution in this space and there is no guarantee that the iterative reconstruction will ever converge to the desired solution. The I4D-VOI reconstruction achieves improved image quality because the VOI region is coupled to the outside region in iterative reconstruction. The motion-averaged image is used as prior information for a "good" initialization and the solution remains constrained to this value outside the VOI. The phase-sorted projection data resolves the motion inside the VOI while taking advantage of the "good" outside region.

No image regularization is used in I4D-VOI reconstruction algorithm. Many other image reconstruction algorithms achieve image quality improvements by incorporating a regularization term or function in iterative reconstruction. This is essentially an assumption about the form of desired reconstruction solution (i.e. it is smooth or has a sparse spatial gradient). The I4D-VOI reconstruction does not make a similar assumption. However, this algorithm can be combined with regularization further image quality improvement.

One of the most attractive features of the I4D-VOI reconstruction is that it is much faster than the ordinary iterative reconstruction. This is because only the projection data that contribute to the VOI need to be used; this is usually a small fraction of the projection data. In IGRT, the chief concern is adequate target coverage. For a solitary lung nodule target, the motion outside the VOI is usually negligible. If there are structures near the target whose motion is of interest (e.g. the diaphragm, heart, or mediastinum), these structures can be included in the reconstruction VOI. Overall, the VOI chosen for the I4D-VOI reconstruction can be quite small relative to the entire imaging volume, speeding up the total reconstruction time.

Ideally, images in IGRT should be available immediately after acquisition. Although the I4D-VOI reconstruction is not yet real-time, the demonstrated computation times suggest that a practical clinical reconstruction solution may be possible with only desktop computing technology.

Future work will include validation of the I4D-VOI algorithm in larger clinical datasets. This will include quantitative demonstration of image quality improvement in the clinical datasets. Other possible work can be the combination of other reconstruction algorithms such as PICCS or ASD-POCS with the I4D-VOI reconstruction for further image quality improvement.

In all cases, the I4D-VOI algorithm provided improved reconstruction results com-

pared to FBP and SART reconstructions, with shorter computation time than SART. The improved image quality, short scan time, and low computational cost make I4D-VOI an attractive reconstruction algorithm for 4D-CBCT.

Chapter 6

Summary

The main challenge in clinical 4D-CBCT is overcoming the undersampling that results from the time constraint of a treatment session. Two approaches were presented for reducing the impact of undersampling artifacts.

The first approach is to quantify the errors due to undersampling and establish tolerance limits. This approach was presented in Chapter 3, in which a table of errors due to undersampling artifacts was compiled for many scan times using reference 4D-CBCT scans. These results allow the selection of a patient-specific scan time, such that error due to undersampling artifacts is less than a desired tolerance. In particular, the most important factor in the scan time optimization is the respiratory cycle, with longer cycles requiring longer scan times. Smaller targets also require longer scan times. The results in this chapter fulfilled Aim I of this dissertation.

Chapters 4 and 5 fulfilled Aim II and presented new image reconstruction methods for undersampled 4D-CBCT projection data. Chapter 4 demonstrated a new "4D-VOI" reconstruction based on limiting dynamic reconstruction to a VOI. This reconstruction reduced undersampling in the region outside the VOI, which is usually most of the imaged volume.

Despite the advantages of the 4D-VOI reconstruction, it does not reduce the un-

dersampling artifacts *inside* the VOI. Chapter 5 presented the iterative 4D-VOI (I4D-VOI) reconstruction which also reduced undersampling artifact inside the VOI using the motion-averaged image as prior information and a local VOI constraint. The comparisons between the different reconstructions are summarized in Table 6.1. All reconstructions here were fast enough that clinical implementation may be possible using inexpensive GPU hardware.

Table 6.1: Qualitative description of reconstructions of undersampled data sets

	Static CBCT w/ FBP	4D-CBCT w/ FBP	4D-VOI	I4D-VOI
Temporal resolution	X	✓	✓	✓
Reduced artifact inside VOI	✓	X	X	✓
Reduced artifact outside VOI	✓	X	✓	✓

6.1 Concluding statement

Four-dimensional CBCT with acquisition time of less than 2 min may be achieved with image reconstruction improvements and evaluation of motion measurement errors at different acquisition times. The 4D-CBCT improvements in this work may potentially improve the targeting accuracy of radiation therapy of mobile lung tumors, and thereby reduce the radiation dose to healthy tissue.

Appendix A

Fast image reconstruction implementation using GPU hardware

There are several hardware approaches for fast image reconstruction computation in CT and cone-beam CT. Computing clusters, application-specific integrated circuits (ASIC) and field-programmable gate arrays (FPGA), cell broadband engines (CBE), and graphics processing units (GPU) are several computing platforms. A computing cluster is the most powerful and expensive option. Computing clusters are usually a shared resource and not always available. Another disadvantage is that acquisition data needs to be transferred over an institutional network which may be busy with other traffic. ASICs and FPGAs are highly optimized and application-specific computing solutions and can be very fast. This is the reconstruction hardware used in most diagnostic CT scanners. These implementations incur high development costs and cannot be modified easily. The cell broadband engine is a parallel computing approach using many microprocessors linked by high-speed interconnections. Kachelrieß *et al.* demonstrated real-time CT and CBCT reconstruction with a cell broadband engine [59]. Although it is a promising technology, at this time CBE remains a novel computing platform, may require a proprietary compiler for programming, and does

not have a universal interface to a computer. The GPU may be the most cost-effective advanced computing solution due to its widespread availability as commodity hardware for desktop computers.

The GPU is a specialized computing hardware dedicated to pixel shading, calculation of the shape and location of polygons in a graphical scene, and other such graphics-specific tasks. These graphical tasks typically comprise a large number of similar computations that can be performed in parallel. Traditional GPU design uses dedicated hardware specifically for graphics computations. The ever-increasing demand for realistic dynamic graphics, particularly in video games, has led to an increase in the computing power of GPUs. In particular, the maximum number of processor cores has increased for greater parallelization. These hardware improvements offer a cost-effective opportunity for high-speed computation in many problems. The application of GPU hardware to applications outside of computer graphics is called general-purpose GPU computing (GPGPU computing). In the past, GPU hardware was designed for a small set of graphics instructions. Fortunately for GPGPU computing, the hardware has been generalized and is much more programmable. In particular, the compute unified device architecture (CUDA) framework (NVIDIA Corporation, Santa Clara, CA, USA) offers the user a high level language based on C for programming NVIDIA GPUs [60].

GPU computing has previously been used in CT reconstruction [61, 57, 62, 63, 64, 65]. The GPU is useful because each voxel is reconstructed independently in FBP and can be performed in parallel by the many processing cores of a GPU. Xu *et al.* laid the groundwork for GPU-based CT reconstruction and demonstrated orders of magnitude speed-up compared to CPU computation [61] Others have harnessed the GPU for algebraic and iterative reconstruction algorithms [62, 65]. Noël *et al.* demonstrated GPU-based CBCT with FBP reconstruction [57].

This Appendix demonstrates the GPU implementation of 4D-CBCT image reconstruction, which is a computationally demanding application. Some reconstruction algorithms may not be feasible within clinical time restrictions without special hardware. It is shown that a GPU can drastically accelerate image reconstruction in 4D-CBCT as compared to a traditional CPU.

A.1 Methods

Imaging acquisition The reconstructions implemented in this work use one patient study. The patient was scanned in an experimental long 4.5 minute acquisition with 1983 projections acquired7. The projection size is $1024 * 768$ pixels. The Real-Time Position Management System (Varian Medical Systems, Palo Alto, CA) was used to acquire a respiratory signal used for sorting projection data into eight phase subsets. The 4D-CBCT images were reconstructed using the FBP algorithm.

In FBP, The processing of an individual cone-beam projection is divided into the following sequence of steps:

- Pre-filtering / smoothing (optional)
- Log-normalization
- Feldkamp weighting
- Half-scan weighting (optional)
- Offset detector weighting (optional)
- Ramp-filtering
- Back-projection

Pre-filtering is a smoothing operation on a projection for decreasing noise. Typically, noise reduction is incorporated into ramp-filtering by windowing of the ramp-filter kernel. In the Feldkamp algorithm, the ramp-filtering operation is performed

along rows in the cone-beam projection in the plane of reconstruction. There is no smoothing along the longitudinal (z) direction. However, filtering in the z-direction can be used to reduce noise. Since the reconstruction matrix is typically coarse in the z-direction (2.5 mm) compared to the detector size (0.388 mm), little or no spatial resolution is lost by pre-filtering the projection in the z-direction. This was implemented with a boxcar convolution filter, with each projection pixel computed in parallel.

Log-normalization is necessary to convert the detector pixel measurement into an attenuation path integral L:

$$L = \int u \cdot dl = \ln I_0 - \ln I \ , \tag{A.1}$$

where I is the pixel value in the projection and I_0 is the normalization value (e.g. value of the pixel in a flat-field image.) Feldkamp weighting applies a geometry-dependent weighting factor to each projection pixel before filtering [39] Additionally, if a half-scan (180° + fan angle) acquisition is used, another weighting factor is applied to account for data redundancy [66]. If offset-detector geometry was used for increased field of view, a weighting factor is applied to avoid truncation artifact [38]. For each of these normalization and weighting steps, each pixel is calculated independently and in parallel.

Next, the projection data is filtered along rows with a ramp-filter kernel. This filtering is achieved by convolving a sinc-squared function with each projection row. Computationally, this is usually performed by multiplication in the Fourier or frequency domain. This implementation used the Fourier transform library CUFFT for code unified device architecture (CUDA) GPU computing. Finally, the projection is back-projected into the reconstruction matrix. The back-projection operation is voxel-based with each voxel computed independently and in parallel. All of these steps involve a large set of independent parallel computations. The computation time

Table A.1: List of tested GPUs and their specifications

GPU model	GT 220	GT 240	Tesla C1060
Number of processor cores	48	96	240
Processor clock frequency (MHz)	1360	1340	1300
GPU memory bandwidth (GB/s)	25.3	54.4	102
Theoretical computational power (GFLOPS*)	192	385	933

*a GFLOP is defined as 10^9 (or *G*iga) *FL*oating point *OP*erations per second.

for each step was measured.

Each of these two reconstruction algorithms was implemented on GPUs and also in a CPU-only implementation. For the GPU reconstruction, only a single executable program was compiled and used for the various GPUs. This GPU program was independent of specific GPU hardware. A runtime program provided by NVIDIA recognized the GPU(s) present on the host computer, and automatically assigned work according to the resources present on the actual GPU(s). Thus this compiled reconstruction program could scale the computational work to a GPU with any number of physical processors. The GPU reconstruction program was written in NVIDIA's CUDA language, which is essentially the C language with a few GPU-specific extensions.

Each reconstruction program was tested separately on various GPUs. These GPUs were used in very similar host computer systems with similar CPUs (quad core, 2.5 to 2.8 GHz clock frequency) and the same DDR3 memory standard. Table A.1 lists these GPUs and the relevant specifications. The GT 220 and GT 240 are low-end and mid-range desktop GPUs, respectively, and are marketed for video games. The Tesla C1060 is a high-end GPU marketed for scientific and engineering computation.

For comparison, each reconstruction algorithm was also implemented in a CPU-only version. These CPU-only reconstruction programs were written in the C++ language and tested on a computer with an Intel Core i7 CPU with a 2.667 GHz clock frequency. The theoretical computational power of this CPU was 42 GFLOPS.

(One GFLOP is one billion floating point operations per second). This was considered a high-end CPU when this experiment was performed. Although this was a quad-core CPU, the CPU-only implementation in this work was not multi-threaded. The program was designed as single-threaded for convenience and portability. Therefore, only one quarter of the computational power of this particular CPU was used.

The overall reconstruction times were measured for both the GPU and CPU-only implementations. For the GPU reconstruction, each of the GPUs listed in Table A.1 was tested.

A.2 Results

Figure A.1 plots the CPU profiled computation times versus the GPU computation times. The GPU shown is the most powerful of the three GPUs tested, the Tesla C1060. For nearly every step in reconstruction, the GPU outperformed the CPU by two orders of magnitude. The projection loading operation cannot be parallelized; nevertheless, some of the latency of loading is hidden due to parallel execution of the GPU and the host CPU, i.e. the GPU works on the current projection while the CPU simultaneously loads the next projection. Overall, the GPU shows a speed-up factor of 264 for computation time per projection. Note that computation time was plotted on a logarithmic scale. In iterative reconstruction, a forward-projection operation is required. The forward-projection time was also measured for each tested hardware.

Table A.2: GPU reconstruction times for FBP (1983 projections from a 4 min. 30 s. scan

	CPU	GT 220	GT 240	Tesla C1060
Number of cores		48	96	240
Time	1 hr. 45 min.	2 min. 44 s.	1 min. 34 s.	54 s.
Speed-up factor	-	38x	67x	116x

Figure A.1: Computational profile of steps in reconstruction. The Tesla C1060 GPU was used.

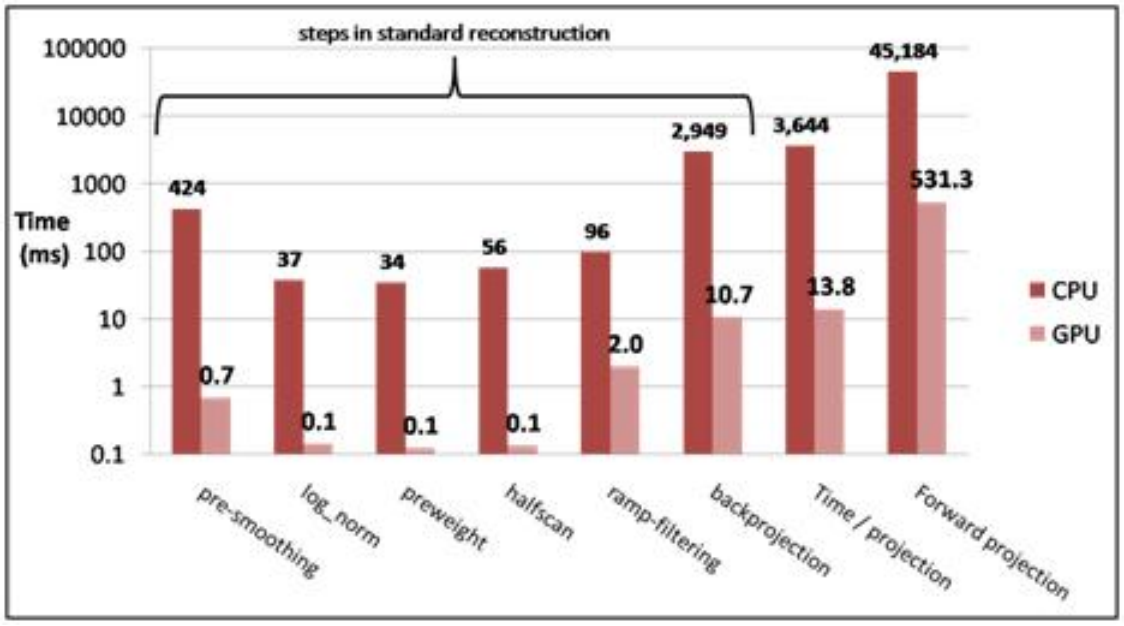

The overall reconstruction times are shown in Table A.2. The speed-up factor compared to the CPU-only implementation is also noted. For the most powerful GPU tested, the reconstruction time for 4D-CBCT was less than 1 minute, which makes this reconstruction clinically feasible. Reconstruction can also begin during the acquisition. Since the reconstruction time (54 s.) was much less than the acquisition time (4.5 min), reconstruction can be completed in real-time.

The speed up factor for the entire reconstruction was not as large as the 264x speed-up factor measured for processing a single projection. This can be explained by the fact that the reconstruction is a hybrid CPU/GPU program with the CPU

controlling the GPU computations. The CPU provides input data to the GPU, and extracts the output GPU computation results. If the GPU waits idly at any point for the next data input from the CPU, a less-than-optimum speed-up factor is achieved.

Lastly note that the performance scaled with the number of processing cores. A plot of speed up factors vs. number of processors is given in Figure A.2. The performance scaled mostly linearly with some diminishing return. The diminishing return was attributed to parts of the program that cannot be parallelized such as the loading of projection data from the hard disk. This problem can be mitigated by pre-fetching of projection data. Greater performance can be expected with program optimization, more powerful GPUs or additional GPUs.

Figure A.2: Scaling of performance with GPU size

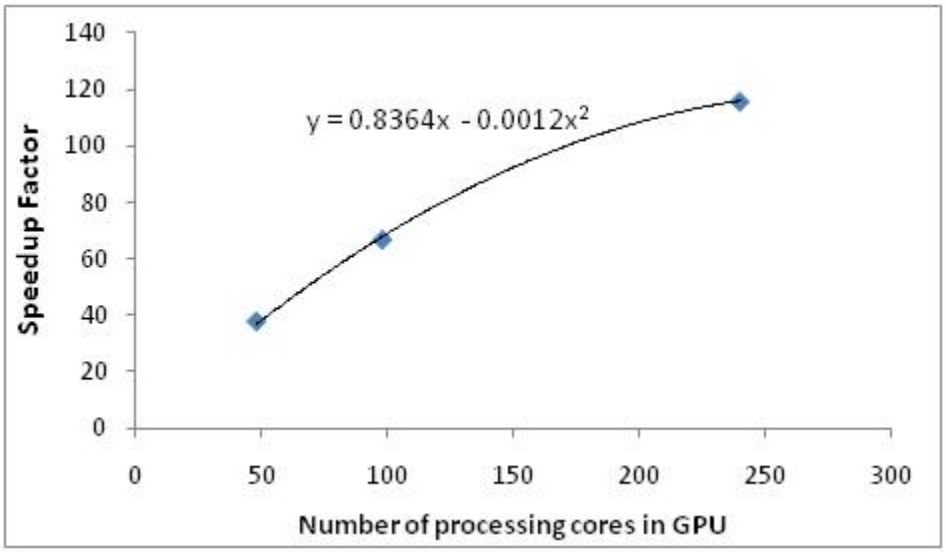

A.3 Discussion

GPU-based image reconstruction has been demonstrated for the computationally demanding 4D-CBCT application. Without special computing hardware, the computational time may be too prohibitive for clinical implementation. Four-dimensional CBCT may require a greater amount of projection data than conventional CBCT.

This work demonstrates that 4D-CBCT reconstruction can be kept below 1 minute with a GPU. Secondly, in addition to the overall reconstruction timing, the various steps in reconstruction have been profiled. These measurements reveal the most costly parts of the reconstruction, providing clues for program optimization. Lastly, the reconstructions were timed on three different GPUs, and showed a near-linear dependence of computational speed on the number of processing cores. This confirms that filtered back-projection is a parallel and scalable algorithm, with potential for proportional computational speed-up with a increasing number of processor cores.

The primary advantage of a GPU for fast reconstruction is its cost-effectiveness. At the time of writing, the NVIDIA GeForce GT 220 and 240 tested in this work cost US $70 and $80 respectively. Although not demonstrated here, it is very simple to scale performance by stacking multiple inexpensive GPUs. The GPU also offers great potential to imaging researchers. Experimental data acquisitions and reconstruction algorithms may not necessarily be accommodated by commercial reconstruction software. GPUs allow researchers to use home-made reconstruction programs to eliminate dependence on commercial reconstruction software. Lastly, 4D-CBCT could be used for target alignment in gated radiotherapy, in which the lung lesion is exposed to radiation only during a consistent portion of the breathing cycle. Since gated therapy depends on 4D image guidance, this technique may require GPU-based 4D-CBCT.

It is possible to further optimize the GPU reconstruction for faster reconstruction times. For instance, Noël *et al.* achieved faster GPU reconstruction using a more efficient data loading and use of cached (shared) memory to store intermediate results [57]. Zhao *et al.* used an efficient division of reconstruction volume for computation parallelization [63]. These two groups both used FBP, similar to this work, but the computational implementations were different and more optimized. This level of optimization was beyond the scope of this work. Nevertheless, it is clear from the

present and previous works that reconstruction with common GPUs can increase the reconstruction speed by two orders of magnitudes over CPU reconstruction.

References

[1] J. Ferlay, H. R. Shin, F. Bray, D. Forman, C. Mathers, and D. M. Parkin, "Estimates of worldwide burden of cancer in 2008: Globocan 2008," *Int. J. Cancer.*, vol. 127, no. 12, pp. 2893–917, 2010. 1

[2] H. H. Liu, P. Balter, T. Tutt, B. Choi, J. Zhang, C. Wang, M. Chi, D. Luo, T. Pan, S. Hunjan, G. Starkschall, I. Rosen, K. Prado, Z. Liao, J. Chang, R. Komaki, J. D. Cox, R. Mohan, and L. Dong, "Assessing respiration-induced tumor motion and internal target volume using four-dimensional computed tomography for radiotherapy of lung cancer," *Int. J. Radiat. Oncol. Biol. Phys.*, vol. 68, no. 2, pp. 531–40, 2007. 1, 2.1.2

[3] J. J. Sonke, M. Rossi, J. Wolthaus, M. van Herk, E. Damen, and J. Belderbos, "Frameless stereotactic body radiotherapy for lung cancer using four-dimensional cone beam CT guidance," *Int. J. Radiat. Oncol. Biol. Phys.*, vol. 74, no. 2, pp. 567–74, 2009. 1.3

[4] B. Rosen, G. Starkschall, K. Britton, R. Mohan, and J. D. Cox, "Utility of four-dimensional computed tomography for analysis of intrafractional and inter-

fractional variation in lung volumes." *Int. J. Radiat. Oncol. Biol. Phys.*, vol. 72, no. 1, pp. 288–94, 2008. 1.3

[5] A. M. Berson, R. Emery, L. Rodriguez, G. M. Richards, T. Ng, S. Sanghavi, and J. Barsa, "Clinical experience using respiratory gated radiation therapy: comparison of free-breathing and breath-hold techniques," *Int. J. Radiat. Oncol. Biol. Phys.*, vol. 60, no. 2, pp. 419–26, 2004. 1.3, 2

[6] C. R. Ramsey, D. Scaperoth, D. Arwood, and A. L. Oliver, "Clinical efficacy of respiratory gated conformal radiation therapy," *Med. Dosim.*, vol. 24, no. 2, pp. 115–9, 1999. 1.3

[7] A. Harsolia, G. D. Hugo, L. L. Kestin, I. S. Grills, and D. Yan, "Dosimetric advantages of four-dimensional adaptive image-guided radiotherapy for lung tumors using online cone-beam computed tomography," *Int. J. Radiat. Oncol. Biol. Phys.*, vol. 70, no. 2, pp. 582–9, 2008. 1.3

[8] G. G. Steel, *Basic Clinical Radiobiology*, 3rd ed. London: Hodder Arnold, 2002, ch. 8, pp. 71–83. 2.1

[9] F. M. Khan, *Clinical Radiation Generators: Linear Accelerator*. Philadelphia, PA: Lippincott Williams & Wilkins, 2003, ch. 4, pp. 42–47. 2.1

[10] ——, *Modern Radiation Therapy*. Philadelphia, PA: Lippincott Williams & Wilkins, 2003, ch. 19-21, pp. 467–520. 2.1

[11] ——, *Treatment Planning I: Isodose Distributions*. Philadelphia, PA: Lippincott Williams & Wilkins, 2003, ch. 11, pp. 199–227. 2.1

[12] "Prescribing, recording, and reporting photon beam therapy (report 50)." *International Commission on Radiation Units and Measurements*, 1993. 2.1.2, 3.1.5.1, 4.1.1, 4.3

[13] S. S. Vedam, P. J. Keall, V. R. Kini, H. Mostafavi, H. P. Shukla, and R. Mohan, "Acquiring a four-dimensional computed tomography dataset using an extrnal respiratory signal," *Phys. Med. Biol.*, vol. 48, no. 1, pp. 45–62, 2003. 2.1.2

[14] T. Pan, T. Y. Lee, E. Rietzel, and G. T. Chen, "4D-CT imaging of a volume influenced by respiratory motion on multi-slice CT," *Med. Phys.*, vol. 31, no. 2, pp. 333–40, 2004. 2.1.2, 3.1.3

[15] M. Ezhil, S. Vedam, P. Balter, B. Choi, D. Mirkovic, G. Starkscahll, and J. Y. Chang, "Determination of patient-specific internal gross tumor volumes for lung cancer using four-dimensional computed tomography," *Radiat Oncol*, vol. 4, p. 4, 2009. 1

[16] P. Keall, S. Vedam, R. George, C. Bartee, J. Siebers, F. Lerma, E. Weiss, and T. Chung, "The clinical implementation of respiratory-gated intensity-modulated radiotherapy," *Med. Dosim.*, vol. 31, no. 2, pp. 152–62, 2006. 2

[17] P. J. Keall, S. Joshi, S. S. Vedam, J. V. Siebers, V. R. Kini, and R. Mohan, "Four-dimensional radiotherapy planning for DMLC-based respiratory motion tracking." *Med. Phys.*, vol. 32, no. 4, pp. 942–51, 2005. 3

[18] I. S. Grills, G. Hugo, L. L. Kestin, A. P. Galerani, K. K. Chao, J. Wloch, and D. Yan, "Image-guided radiotherapy via daily online cone-beam CT substantially reduces margin requirements for stereotactic lung radiotherapy," *Int. J. Radiat. Oncol. Biol. Phys.*, vol. 70, no. 4, pp. 1045–56, 2008. 2.2

[19] P. S. Cho, R. H. Johnson, and T. W. Griffin, "Cone-beam CT for radiotherapy applications," *Phys. Med. Biol.*, vol. 40, no. 11, pp. 1863–83, 1995. 2.2.1

[20] D. A. Jaffray, J. H. Siewerdsen, J. W. Wong, and A. A. Martinez, "Flat-panel cone-beam computed tomography for image-guided radiation therapy," *Int. J. Radiat. Oncol. Biol. Phys.*, vol. 53, no. 5, pp. 1337–49, 2002. 2.2.1

[21] L. E. Antonuk, J. Yorkston, W. Huang, J. H. Siewardsen, J. M. Boudry, Y. el Mohri, and M. V. Marx, "A real-time, flat-panel, amorphous silicon, digital x-ray imager," *Radiographics*, vol. 15, no. 4, pp. 993–1000, 1995. 2.2.1

[22] D. A. Jaffray and J. H. Siewerdsen, "Cone-beam computed tomography with a flat-panel imager: initial performance characterization," *Med. Phys.*, vol. 27, no. 6, pp. 1311–23, 2000. 2.2.1

[23] H. Li, X. R. Zhu, L. Zhang, L. Dong, S. Tung, A. Ahamad, K. S. Chao, W. H. Morrison, D. I. Rosenthal, D. L. Schwartz, R. Mohan, and A. S. Garden, "Comparison of 2D radiographic images and 3D cone beam computed tomography for positioning head-and-neck radiotherapy patients," *Int. J. Radiat. Oncol. Biol. Phys.*, vol. 71, no. 3, pp. 916–25, 2008. 2.2.1

[24] P. J. Keall, G. Starkschall, H. Shukla, K. M. Forster, V. Ortiz, C. W. Stevens, S. S. Vedam, R. George, T. Guerrero, and R. Mohan, "Acquiring 4d thoracic ct scans using a multislic helical method." *Phys. Med. Biol.*, vol. 49, no. 10, pp. 2053–67, 2004. 2.2.2

[25] J. Lu, T. M. Guerrero, P. Munro, A. Jeung, P. C. Chi, P. Balter, X. R. Zhu, R. Mohan, and T. Pan, "Four-dimensional cone beam CT with adaptive gantry rotation and adaptive data sampling," *Med. Phys.*, vol. 34, no. 9, pp. 3520–9, 2007. 2.4.1, 3

[26] J. J. Sonke, L. Zijp, P. Remeijer, and M. van Herk, "Respiratory correlated cone beam CT," *Med. Phys.*, vol. 32, no. 4, pp. 1176–86, 2005. 2.4.1

[27] T. Li and L. Xing, "Optimizing 4D cone-beam CT acquisition protocol for external beam radiotherapy," *Int. J. Radiat. Oncol. Biol. Phys.*, vol. 67, no. 4, pp. 1211–9, 2007. 2.3, 2.4.1

[28] E. Y. Sidky, C. M. Kao, and X. Pan, "Accurate image reconstruction from few-views and limited-angle data in divergent-beam CT," *J. X-Ray. Sci. Tech.*, vol. 14, no. 2, pp. 119–39, 2006. 2.4.2, 3.1.2

[29] E. Y. Sidky and X. Pan, "Image reconstruction in circular cone-beam computed tomography by constrained, total-variation minimization," *Phys. Med. Biol.*, vol. 53, no. 17, pp. 4777–807, 2008. 2.4.2, 3.1.2

[30] G. H. Chen, J. Tang, and S. Leng, "Prior image constrained compressed sensing (PICCS)," *Proc. Soc. Photo. Opt. Instrum. Eng.*, vol. 6856, 2008. 2.4.2

[31] S. Leng, J. Tang, J. Zambelli, B. Nett, R. Tolakanahalli, and G. H. Chen, "High temporal resolution and streak-free four-dimensional cone-beam computed tomography," *Phys. Med. Biol.*, vol. 53, no. 20, p. 565373, 2008. 2.4.2, 4.1.5

[32] F. Bergner, T. Berkus, M. Oelhafen, P. Kunz, T. Pa, R. Grimmer, L. Ritscl, and M. Kachelriess, "An investigation of 4D cone-beam CT algorithms for slowly rotating scanners," *Med. Phys.*, vol. 37, no. 9, pp. 5044–53, 2010. 2.4.2

[33] J. Bian, J. H. Siewerdsen, X. Han, E. Y. Sidky, J. L. Prince, C. A. Pelizzari, and X. Pan, "Evaluation of sparse-view reconstruction from flat-panel-detector cone-beam CT," *Phys. Med. Biol.*, vol. 55, no. 22, pp. 6575–99, 2010. 2.4.2

[34] X. Pan, E. Y. Sidky, and M. Vannier, "Why do commercial CT scanners still employ traditional, filtered back-projection for image reconstruction?" *Inverse Probl.*, vol. 25, no. 12, p. 123009, 2009. 2.4.2

[35] M. Ahmad and T. Pan, "Target-specific optimization of four-dimensional cone beam computed tomography," *Med. Phys.*, vol. 39, no. 9, pp. 5683–96, 2012. 3, 3.1, 3.2, 3.3, 3.4, 3.5, 3.6, 3.7, 3.8, 3.9, 3.10, 3.11, 3.12, 3.13, 3.14, 3.15, 3.16, 3.17, 3.18, 3.19, 3.20, 5.1.4

[36] Z. Qi and G. H. Chen, "Extraction of tumor motion trajectories using PICCS-4DCBCT: a validation study," *Med. Phys.*, vol. 38, no. 10, pp. 5530–8, 2011. 3, 3.1.5

[37] T. Li, L. Xing, P. Munro, C. McGuinness, M. Chao, Y. Yang, B. Loo, and A. Koong, "Four-dimensional cone-beam computed tomography using an on-board imager," *Med. Phys.*, vol. 33, no. 10, p. 382533, 2006. 3

[38] G. Wang, "X-ray micro-CT with a displaced detector array," *Med. Phys.*, vol. 29, no. 7, pp. 1634–6, 2002. 3.1.1, A.1

[39] L. A. Feldkamp, L. C. Davis, and J. W. Kress, "Practical cone-beam algorithm," *J. Opt. Soc. Am.*, vol. 1A, pp. 612–9, 1984. 3.1.2, 4.1.1, 5.1.2, A.1

[40] G. H. Chen, J. Tang, and S. Leng, "Prior image constrained compressed sensing (PICCS): a method to accurately reconstruct dynamic CT images from highly undersampled projection data sets," *Med. Phys.*, vol. 35, no. 2, pp. 660–3, 2008. 3.1.2

[41] S. Leng, J. Zambelli, R. Tolakanahalli, B. Nett, P. Munro, J. Star-Lack, B. Paliwal, and G. H. Chen, "Streaking artifacts reduction in four-dimensional cone-beam computed tomography," *Med. Phys.*, vol. 35, no. 10, p. 464959, 2008. 3.1.2

[42] K. Choi, J. Wang, L. Zhu, T. S. Suh, S. Boyd, and L. Xing, "Compressed sensing based cone-beam computed tomography reconstruction with a first-order method," *Med. Phys.*, vol. 37, no. 9, p. 511325, 2010. 3.1.2

[43] R. C. Gonzalez and R. E. Woods, *Digital Image Processing*, 2nd ed. Upper Saddle River, N.J.: Prentice Hall, 2002. 3.1.2

[44] P. J. Keall, G. S. Mageras, J. M. Balter, R. S. Emery, K. M. Forster, S. B. Jiang, J. M. Kapatoes, D. A. Low, M. J. Murphy, B. R. Murray, C. R. Ramsey, M. B. van Herk, S. S. Vedam, J. W. Wong, and E. Yorke, "The management of respiratory motion in radiation oncology report of aapm task group 76," *Med. Phys.*, vol. 33, no. 10, pp. 3874–900, 2006. 3.1.3, 4.1.4

[45] K. Levenberg, "A method for the solution of certain problems in least squares," *Quart. Appl. Math.*, vol. 2, pp. 164–168, 1944. 3.1.5

[46] D. W. Marquardt, "An algorithm for least-squares estimation of nonlinear parameters," *SIAM. J. Appl. Math.*, vol. 11, no. 2, pp. 431–441, 1963. 3.1.5

[47] J. Mor, *The Levenberg-Marquardt algorithm: Implementation and theory.* Springer Berlin / Heidelberg, 1978, vol. 630, ch. Numerical Analysis, pp. 105–116. 3.1.5

[48] W. Lu, M. L. Chen, G. H. Olivera, K. J. Ruchala, and T. R. Mackie, "Fast free-form deformable registration via calculus of variations," *Phys. Med. Biol.*, vol. 49, no. 14, pp. 3067–87, 2004. 3.1.5

[49] Z. Qi and G. H. Chen, "Performance studies of four-dimensional cone beam computed tomography," *Phys. Med. Biol.*, vol. 56, no. 20, pp. 6709–21, 2011. 3.1.5

[50] M. Ahmad and T. Pan, "Four-dimensional volume-of-interest reconstruction for cone-beam computed tomography-guided radiation therapy," *Med. Phys.*, vol. 38, no. 10, pp. 5646–56, 2011. 4, 4.2, 4.3, 4.4, 4.5, 4.6, 4.7, 4.8, 4.9, 4.10, 4.11, 4.12, 4.13, 4.14, 4.15, 4.16, 4.17, 4.18, 4.19, 4.20, 4.21, 5

[51] H. Turbell, "Cone-beam reconstruction using filtered backprojection," Ph.D. dissertation, Linköping University Institute of Technology, 2001. 4.1

[52] A. C. Kak and M. Slaney, *Summary of Shepp-Logan phantom parameters for tomographic imaging.* New York: Society for Industrial and Applied Mathematics, 2001, ch. 3, pp. 53–55. 4.1.2

[53] G. C. McKinnon and R. H. T. Bates, "Towards imaging the beating heart usefully with a conventional CT scanner," *IEEE Trans. Biomed. Eng.*, vol. BME-28, no. 2, pp. 123–127, 1981. 4.1.5

[54] Z. Wang, Q. J. Wu, L. B. Marks, N. Larrier, and F. F. Yin, "Cone-beam CT localization of internal target volumes for stereotactic body radiotherapy of lung lesions," *Int. J. Radiat. Oncol. Biol. Phys.*, vol. 69, no. 5, p. 161824, 2007. 4.2.4

[55] F. Xu and K. Mueller, "Accelerating popular tomographic reconstruction algorithms on commodity pc graphics hardware," *IEEE Trans. Nucl. Sci.*, vol. 52, no. 3, pp. 654–663, 2005. 4.2.4

[56] ——, "Real-time 3D computed tomographic reconstruction using commodity graphics hardware," *Phys. Med. Biol.*, vol. 52, no. 12, pp. 3405–19, 2007. 4.2.4

[57] P. B. Noel, A. M. Walczak, J. Xu, J. J. Corso, K. R. Hoffmann, and S. Schafer, "GPU-based cone beam computed tomography," *Comput. Methods. Programs. Biomed.*, vol. 98, no. 3, pp. 271–77, 2009. 4.2.4, A, A.3

[58] A. C. Kak and M. Slaney, *SART (Simultaneous Algebraic Reconstruction Technique).* New York: Society for Industrial and Applied Mathematics, 2001, ch. 7, pp. 285–92. 5.1.1

[59] M. Kachelrieß, M. Knaup, and O. Bockenbach, "Hyperfast parallel-beam and cone-beam backprojection using the cell general purpose hardware," *Med. Phys.*, vol. 34, no. 4, pp. 1474–86, 2007. A

[60] M. Garland, S. L. Grand, J. Nickolls, J. Anderson, J. Hardwick, S. Morton, E. Phillips, Y. Zhang, and V. Volkov, "Parallel computing experiences with CUDA," *Micro, IEEE*, vol. 28, no. 4, pp. 13–27, 2008. A

[61] F. Xu and K. Mueller, "Real-time 3D computed tomographic reconstruction using commodity graphics hardware," *Phys. Med. Biol.*, vol. 52, no. 12, pp. 3405–19, 2007. A

[62] F. Xu, W. Xu, M. Jones, B. Keszthelyi, J. Sedat, D. Agard, and K. Mueller, "On the efficiency of iterative ordered subset reconstruction algorithms for acceleration on GPUs," *Comput. Methods Programs. Biomed.*, 2009. A

[63] X. Zhao, J. J. Hu, and P. Zhang, "GPU-based 3D cone-beam CT image reconstruction for large data volume," *Int. J. Radiat. Oncol. Biol. Phys.*, vol. 2009, p. 149079, 2009. A, A.3

[64] X. Jia, Y. Lou, R. Li, W. Song, and S. Jiang, "GPU-based fast cone beam CT reconstruction from undersampled and noisy projection data via total variation," *Med. Phys.*, vol. 37, no. 4, pp. 1757–60, 2010. A

[65] F. Vazquez, E. M. Garzon, and J. J. Fernandez, "A matrix approach to tomographic reconstruction and its implementation on GPUs," *J. Struct. Biol.*, vol. 170, no. 1, pp. 146–51, 2010. A

[66] D. L. Parker, "Optimal short scan convolution reconstruction for fanbeam CT," *Med. Phys.*, vol. 9, no. 2, pp. 254–7, 1982. A.1

Vita

Moiz Ahmad graduated from Bellaire Senior High School in Bellaire, TX in 2001. He attended The University of Texas at Austin from 2001–2005 where he completed Bachelor of Science degrees in Electrical Engineering and in Physics. After graduation, he worked as an electrical engineer in electronics manufacturing for Harris-Stratex Networks in San Antonio, TX from 2006–2007, where he implemented quality control of the manufacture of microwave frequency radios. In 2007, he entered The University of Texas Graduate School of Biomedical Sciences in Houston, TX to pursue a Ph.D. in Medical Physics. For his research work, Moiz was a research assistant at The University of Texas MD Anderson Cancer Center in the Department of Imaging Physics. Moiz has research interests in medical and applied physics, signal and image reconstruction, image analysis, and scientific computation. His goal is to pursue these research interests at an academic medical center while practicing clinical medical physics.